Laser-induced incandescence for soot diagnostics at high pressure

Maximilian Hofmann

Physikalisch-Chemisches Institut
Universität Heidelberg
November, 2006

INAUGURAL-DISSERTATION

zur

Erlangung der Doktorwürde

der

Naturwissenschaftlich-Mathematischen Gesamtfakultät

der

Ruprecht-Karls-Universität

Heidelberg

vorgelegt von

Diplom-Chemiker Arnulf Maximilian Hofmann

aus Bielefeld

Tag der mündlichen Prüfung: 24. November 2006

Laserinduzierte Inkandeszenz für die Rußdiagnostik bei erhöhtem Druck

Laser-induced incandescence for soot diagnostics at high pressure

Gutachter:

Prof. Dr. Jürgen Wolfrum

Prof. Dr. Christof Schulz

SUMMARY

This work focuses on laser-induced incandescence (LII) at elevated pressure. LII is a laser-based technique for measuring particle sizes and volume fractions of nano-sized particles in aerosols. These particles, as emitted by traffic in the form of soot, cause a significant health risk, as nano-sized particles can penetrate deeply into the lungs and are considered important for causing asthma, fibrosis and the development of tumors [1,2]. Over the past 20 years, LII has been developed and applied mainly for soot diagnostics in flames. However, only little work has been performed before on LII in sooting flames at elevated pressure. Nonetheless, this is important for applications in technical high-pressure environments, namely Diesel engines.

Construction of a sooting high-pressure burner. In order to investigate the ability of LII as a tool for soot diagnostics at elevated pressure, a sooting high-pressure burner was constructed in cooperation with the research group of Prof. Dr. Dr. h.c. H. Gg. Wagner and Dr. H. Jander of the Universität Göttingen. Several improvements compared to previous burners were made. The burner produced long-term stable, laminar ethylene/air flames up to 10 bar with pressure fluctuations less than ± 2%. In LII diagnostics, this burner is unique in its performance world wide.

Modeling laser-induced incandescence. The LII signal results from the heat-up of particles by a nanosecond laser pulse and subsequent cooling due to near-blackbody radiation and different competing heat-loss paths. This process was modeled by setting up an energy and mass balance for the different heat- and mass-loss mechanisms. Recent advancements on the different sub-models were combined in a numerical model. This model, called LIISim, enables the modeling of LII signals as well as the fitting of experimental LII decay curves with a Levenberg-Marquardt non-linear least-squares fitting algorithm. Additionally, a perl script was written which allows the access to the LII model using a web browser. For the first time, an LII model was made available to the scientific community by a web interface. This will simplify the comparison of different LII models and reveal deficiencies in the underlying sub-models. LIISim is available at http://www.liisim.com.

Particle sizing with LII at variable pressure. The log-normal size distribution of soot particles was measured in the new high-pressure burner at pressures of 1 – 10 bar using LII. The flame temperature as well as the peak particle temperature are required as input parameters for the data evaluation with LIISim. These parameters were determined by two-color pyrometry of non-laser-heated soot (flame temperature) and by two-color LII (peak particle temperature). Low laser fluences of 70 – 115 mJ/cm^2 at 1064 nm were used to avoid evaporation. C_2 fluorescence within the 550 nm detection channel might interfere with the LII signal. However, spectrally-resolved detection showed no narrowband interferences in the region of 656 – 400 nm for the low laser fluences used in this study at all investigated pressures. Additional to the LII measurements, soot samples were taken from the flame and the particle-size distribution was determined from transmission-electron microscopy (TEM) images of these samples. For the first time, soot particle-size distributions obtained with LII could be compared with a second, independent method at elevated pressures. Moreover, a first comparison of different heat-conduction models used for the evaluation of experimental LII signals could be performed. The results show excellent agreement between the mean diameter of the particle-size distribution obtained by TEM analysis and LII for all pressures, if the LII data are evaluated with the model of Fuchs taking into account the reduced heat conduction of aggregated particles.

This work significantly advanced the understanding of LII at high pressures which further improves the applicability of this diagnostics technique to *in-situ* particle-size measurements in practical high-pressure combustors like Diesel engines.

ZUSAMMENFASSUNG

In dieser Arbeit wurde die laserinduzierte Inkandeszenz (LII) in rußenden Hochdruckflammen untersucht. LII ist ein laser-basiertes Messverfahren zur Bestimmung von Größe und Konzentration von Nanopartikeln in Aerosolen. Solche Partikel, wie sie z.B. im Straßenverkehr als Ruß emittiert werden, stellen ein erhebliches Gesundheitsrisiko dar, da Nanopartikel tief in die Lunge eindringen können und im Verdacht stehen, Asthma, Fibrose und Krebs zu verursachen [1,2]. Während der letzten 20 Jahre lag der Schwerpunkt auf der Entwicklung und Anwendung von LII für die Rußdiagnostik in Flammen. Bisher lagen jedoch nur wenige Untersuchungen zu LII in rußenden Flammen unter erhöhtem Druck vor.

Konstruktion eines rußenden Hochdruckbrenners. Um das Potential von LII für die Rußdiagnostik bei höheren Drücken zu untersuchen, wurde ein rußender Hochdruckbrenner konstruiert. Dies erfolgte in Zusammenarbeit mit Prof. Dr. Dr. h.c. H. Gg. Wagner und Dr. H. Jander von der Universität Göttingen. Zahlreiche Verbesserungen im Vergleich zu früheren Brennern der Göttinger Arbeitsgruppe wurden realisiert. Mit diesem Brenner können laminare Ethylen/Luft-Flammen bis zu 10 bar über einen langen Zeitraum hin stabilisiert werden. Dieser Brenner ist in seinen Eigenschaften bezüglich Druck und Flammentyp einzigartig auf dem Gebiet der LII-Diagnostik.

Modellierung der laserinduzierten Inkandeszenz. Das LII-Signal wird durch das Aufheizen von Partikeln mit einem Laserpuls von einigen Nanosekunden Dauer erzeugt, wonach die Partikel aufgrund verschiedener Wärmeflüsse wieder abkühlen und dabei thermische Strahlung aussenden. Dieser Prozess wurde modelliert, indem eine Energie- und Massenbilanz aufgestellt wurde. Das Model, LIISim genannt, erlaubt das Modellieren von LII-Signalen sowie das Anpassen experimenteller LII-Abklingkurven mit Hilfe eines nicht-linearen Levenberg-Marquardt Anpassungs-Algorithmus. Zudem wurde ein Perl-Skript geschrieben, das eine Schnittstelle zu dem Modell über einen Internet-Browser darstellt. Auf diese Weise wird Forschern zum ersten mal der Zugang zu einem LII-Model über das Internet ermöglicht. LIISim ist unter http://www.liisim.com verfügbar.

Bestimmung der Partikelgröße mit LII unter verschiedenen Drücken. In dem neu entwickelten Hochdruckbrenner wurde die logarithmische Normalverteilung von Rußpartikelgrößen mit LII in Flammen unter 1 – 10 bar ermittelt. Für die Auswertung der Messsignale mit LIISim wird die Gasphasentemperatur sowie die maximale Aufheiztemperatur der Partikel benötigt. Diese wurden mit Zweifarben-Pyrometrie des Rußeigenleuchtens bzw. mit Zweifarben-LII gemessen. Bei der Detektion besteht die Gefahr, dass Fluoreszenz des C_2-Radikals bei 550 nm mit dem LII-Signal überlagert. Eine spektral aufgelöste Detektion des LII-Signallichts zeigte jedoch keine schmalbandigen Interferenzen im Bereich von 656 – 400 nm für alle untersuchten Drücke. Zusätzlich zu den LII-Messungen wurden der Flamme Rußproben entnommen und die Partikelgrößenverteilung anhand von Aufnahmen dieser Proben mit einem Transmissions-Elektronenmikroskop (TEM) bestimmt. Zum ersten Mal konnten mit LII gemessene Partikelgrößenverteilungen von Ruß in einer Flamme bei erhöhtem Druck mit einer zweiten, unabhängigen Methode verglichen werden. Die Ergebnisse zeigen eine sehr gute Übereinstimmung zwischen den mit LII ermittelten Werten des mittleren Durchmessers und jenen aus den Analysen der TEM-Bilder. Es konnte gezeigt werden, dass die Übereinstimmung am besten gegeben ist, wenn die LII-Daten mit dem Wärmeleitungsmodel von Fuchs und unter der Berücksichtigung der verringerten Wärmeleitung aggregierter Rußpartikel ausgewertet werden.

Durch diese Arbeit wurden wesentlich Fortschritte im Verständnis von LII bei erhöhtem Druck erzielt, was eine bessere Anwendung dieser diagnostischen Methode für die *in-situ*-Bestimmung von Partikelgrößen in technischen Verbrennungsprozessen ermöglicht.

LIST OF SYMBOLS

Latin symbols

a_{cs}, b_{cs}, c_{cs}	Empirical factors for the temperature dependence of the heat capacity of soot, J mol^{-1} K^{-1}, J mol^{-1} K^{-2}, J K mol^{-1}
a_{cg}, b_{cg}, c_{cg}	Empirical factors for the temperature dependence of the heat capacity of nitrogen, J mol^{-1} K^{-1}, J mol^{-1} K^{-2}, J K mol^{-1}
C_{abs}	Absorption cross-section of soot, m^2
CMD	Count median diameter of log-normal distribution, m
c_p	Heat capacity at constant pressure, J K^{-1} kg^{-1}
c_v	Heat capacity at constant volume, J K^{-1} kg^{-1}
D_{eff}	Effective heat-transfer diameter of an aggregate
D_f	Fractal dimension of an aggregate
D_h	Scaling parameter for D_{eff}
d_p	Particle diameter, m
$E(m)$	Soot absorption function
$F(t)$	Laser temporal intensity profile, W m^{-2}
f	Euckenfactor
f_v	Soot volume fraction
G	Geometry-dependent heat-transfer factor
h_i	Polynomial coefficient for the temperature dependence of the enthalpy of vaporization of soot
J	Mass flux, kg s^{-1}
K	Calibration constant
Kn	Knudsen number
k	Imaginary part of the complex index of refraction
k_g	Thermal conductivity of air, W m^{-1} K^{-1}
k_h	Scaling parameter for D_{eff}
L	Characteristic length, m
M	Molar mass, kg mol^{-1}
m	Complex index of refraction
m_i	Polynomial coefficient for the temperature dependence of the molar mass of soot vapor
m_p	Particle mass, kg
N	Molecular flux, molecules m^{-2} s^{-1}
N_E	Number of experimental data points
N_d	Number density, m^{-3}
N_p	Number of primary particles per aggregate

n	Real part of the complex index of refraction
P	Number of fitting parameters
p	Pressure, Pa
p_i	Polynomial coefficient for the temperature dependence of the vapor pressure of soot
q	Energy transfer rate, J s^{-1}
R_g	Radius of gyration of an aggregate, m
r_i	Position vector of the i^th primary particle in an aggregate
S_LII	LII signal
s_i	Polynomial coefficient for the dependence of the molecular cross-section of soot vapor on the molar mass of the vapor
T_p	Particle temperature, K
T_g	Gas temperature, K
t	Time, s
v	Vibrational quantum number

Greek symbols

α	Thermal accommodation coefficient
β	Mass accommodation coefficient
Γ	Diffusion coefficient, $\mathrm{m}^2\ \mathrm{s}^{-1}$
γ	Heat capacity ratio $c_\mathrm{p}/c_\mathrm{v}$
Δ	Difference
ΔH_v	Enthalpy of vaporization, J mol^{-1}
δ	Thickness of boundary layer in Fuchs' model, m
ε	Emissivity of soot
θ	Total emission coefficient
Λ	Coefficient used in Fuchs' model
λ	Wavelength, m
λ_MFP	Mean free path length of gas molecules, m
ρ	Density, kg m^{-3}
Σ	Molecular cross-section, m^2
σ_g	Geometric width of a log-normal distribution
ϕ	Equivalence ratio
χ^2	Maximum likelihood estimator
Ω	Spectral response function of the detection system

Subscripts

det	Detection
ex	Excitation
s	Soot
g	Gas
FM	Free-molecular regime
C	Continuum regime
Trans	Transition regime
abs	Absorption
evap	Evaporation
cond	Conduction
rad	Radiation
int	Internal energy
i	Counter index for sum
p	Particle
v	Vapor
δ	Boundary layer used in Fuchs' model for heat conduction

Superscripts

*	Average value

LIST OF ABBREVIATIONS

CCD	Charge-coupled device
CGI	Common gateway interface
FWHM	Full width at half maximum
GS	Giga sample
HAB	Height above burner
HTML	Hyper text markup language
IC	Internal combustion
LII	Laser-induced incandescence
LIF	Laser-induced fluorescence
MS	Mega sample
ppm	Parts per million
TEM	Transmission-electron microscopy

LIST OF CONSTANTS

$c = 299792458\ \mathrm{m\ s^{-1}}$	Speed of light in vacuum
$h = 6.62608\cdot10^{-34}\ \mathrm{J\ s}$	Planck constant
$k_\mathrm{B} = 1.380662\cdot10^{-23}\ \mathrm{J\ K^{-1}}$	Boltzmann constant
$\sigma_\mathrm{B} = 5.670\cdot10^{-8}\ \mathrm{W\ m^{-2}\ K^{-4}}$	Stefan-Boltzmann constant
$N_\mathrm{A} = 6.0221415\cdot10^{-23}\ \mathrm{mol^{-1}}$	Avogadro constant
$R = 8.314\ \mathrm{J\ K^{-1}\ mol^{-1}}$	Universal gas constant

CONTENTS

1 INTRODUCTION

Without question, today's society depends on a constant supply of energy. Energy is needed for heating, manufacturing, production of electricity, and transportation. The demand for energy is steadily growing and has increased by ~90% world wide in the time between 1971 and 2003. In emerging markets, the demand is increasing even more rapidly. For instance, the energy supply of China has increased by more than 250% over the past 30 years [3].

The primary energy sources are oil, coal and gas as well as nuclear, hydro, wind and solar power. The share of total primary energy supply in the world is shown in Figure 1.1.

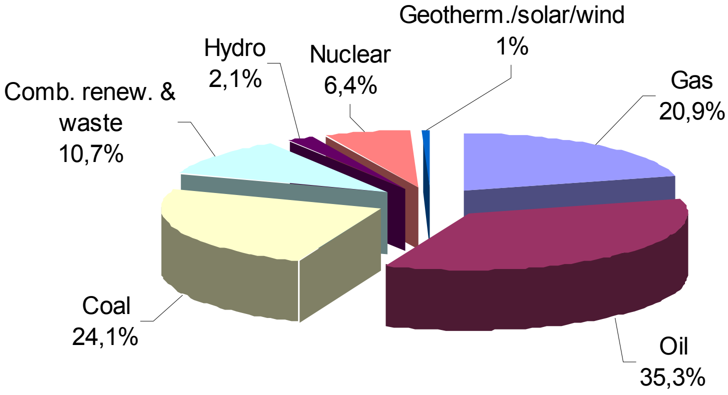

Figure 1.1. Share of total primary energy supply in the world 2003 [3].

It can be seen in Figure 1.1 that fossil fuels, i.e. oil, coal and gas cover more than 80% of the primary energy supply. They are mainly used in power plants, gas turbines and internal combustion engines. Combustion is the technological process that gains energy from these compounds. Including the energy from renewables and waste, combustion processes are responsible for over 90% of the world energy supply. Hence, the combustion technology is of utmost importance for efficient use of these resources. Although fossil fuels are limited and the combustion of these fuels releases the green-house gas CO_2, the use of oil, coal and gas still remains the main source of energy for the next decades.

With the upcoming biomass-to-liquid-technique, BTL, a renewable substitute for oil might be available in future [4-6].

Any combustion process, however, is accompanied with the formation of pollutants. In the case of the combustion of hydrocarbons, the major pollutants emitted are carbon-monoxide (CO), unburned hydrocarbons (HC), nitric oxides (NO_x), and particulate matter (PM). The emission of soot and particulate matter have gained increased interest with the growing popularity of the Diesel engine over the last years. Though the efficiency of Diesel engines is higher, the emission of pollutants, mainly of NO_x and particulate matter (soot), is higher as well compared to gasoline engines with exhaust gas aftertreatment. In Europe, the so-called "Euro-standards" were introduced to limit the emission of these pollutants in traffic. The standards are listed in Table 1.1. The values for the new Euro V standard are guidelines only – there are no final values yet.

Standard	**Year**	**Diesel (g/km)**				**Gasoline (g/km)**		
		CO	**HC**	**NO_x**	**PM**	**CO**	**HC**	**NO_x**
Euro III	2000	0.64	–	0.50	0.05	2.30	0.20	0.15
Euro IV	2005	0.50	–	0.25	0.025	1.00	0.10	0.08
Euro V	2008–10	1.00	0.05	0.08	0.0025	1.00	0.05	0.08

Table 1.1. European emission standards for passenger cars. PM = particulate matter.

It can be seen that the emission of particulate matter is restricted in terms of emitted mass per kilometer. However, in contrast to pollutants like NO_x and HC, the toxicity of particulate matter is not given by mass only, but by particle size as well. Smaller particles can penetrate deeper into the lungs and these ultrafine particles are considered important for causing asthma, fibrosis, and the development of tumors [1,2]. Hence, knowledge about the emitted particle size of particulate matter is important as well.

Suitable diagnostics tools are required in order to maximize the efficiency of combustion processes and minimize the emission of pollutants as listed above. Laser-optical techniques have been established in the field of combustion diagnostics because they are non-intrusive and, therefore, do not influence the process under investigation. Moreover, they can provide high spatial and temporal resolution. Laser-induced fluorescence (LIF), laser-induced incandescence (LII), Raman, Rayleigh and Mie scattering as well as absorption spectroscopy are commonly applied techniques to measure temperatures, species concentrations, flow velocities and particle/droplet sizes in flames, sprays and reacting flows [7-9]. With these techniques, a detailed insight into the entire combustion process is possible, starting from the mixing of fuel with air, followed by ignition, flame development, pollutant formation and exhaust gas analysis. In such a way, techniques can be developed that reduce the amount of pollutants at their origin without the need of exhaust gas after-treatment.

Laser-induced incandescence (LII) can be used to determine the size of ultrafine particles in the order of 5 – 100 nm. LII has been used over the past 20 years to determine both soot concentrations and soot particle sizes in flames and exhaust gases. In LII, nano-sized particles are heated by a pulsed laser of several nanoseconds duration. Depending on the laser fluence, soot particles are heated up to 2000 – 4000 K and cool down over a period of some hundreds of nanoseconds. The particles that are heated by the laser emit a near-blackbody radiation which is strongly increased compared to particles at flame temperature. The absolute light intensity of the incandescence is related to the soot volume, whereas the signal decay correlates to the particle size, as small particles cool down faster than large particles.

Historically, LII emerged from the field of laser diagnostics in combustion and the main focus has been, and still is, on the diagnostics of nano-sized soot particles in flames and exhaust gases. With upcoming nanotechnology, however, researchers started to investigate non-carbon materials as well. For instance, particle sizes or particle-size distributions were obtained with LII from iron nano-particles [10], manganese-oxide nanoparticles [11] as well as from titanium, molybdenum and tungsten particles [12]. These are promising experiments that help to understand the LII process in the case of soot as well.

In order to obtain particle sizes from experimental LII signal decays, numerical models are required that describe the cooling process after laser heating. These models are fitted to experimental signals with the particle size or both the mean diameter and the geometric width of a particle-size distribution as free parameters. Modeling the LII process is of major importance when applying LII for sizing of nano-particles and much progress has been made on modeling the relevant heat- and mass-loss mechanisms. However, significant differences exist between the models developed by different research groups [13]. These differences can be attributed to the use of different values for the physical input parameters, like the soot absorption function and heat capacities as well as to the use of different expressions for the heat- and mass-loss mechanisms. Therefore, detailed experiments are necessary in order to determine the correct values of uncertain parameters, and the comparison of particle sizes obtained by LII with an independent method can be used to verify the applied model used for data evaluation.

Although many applications were performed under atmospheric pressure conditions, e.g. in laboratory flames, only limited investigations have been performed on LII at elevated pressures. In Diesel engines, large pressure variations between 1 and 70 bar occur. In order to apply LII quantitatively at elevated pressure, systematic investigations in stable, laminar flames at elevated pressure are necessary to understand the behavior of LII under these conditions. It has been shown that the LII signal decreases faster with increasing pressure due to an increased heat conduction at elevated pressure [14]. Hence, it must be clarified whether these fast decaying signals obtain sufficient information to determine particle sizes. Different heat conduction models are used in literature to evaluate the particle size. So far, it has not been investigated which data evaluation model yields the correct particle size at elevated pressure and which effects, like the aggregation of the nano-sized particles, have an increased impact on the LII signal at elevated pressure. Comparison of particle sizes obtained by LII at elevated pressure with a second, independent method has not been performed before, which, however, is important to clarify the ability of LII for particle sizing under these conditions. Therefore, the goal of this thesis was to construct, build and operate a burner that provides laminar sooting ethylene/air flames at pressures up to 10 bar.

LII was performed in this burner in order to determine the ability of LII as an optical tool for soot diagnostics at elevated pressure. Particle-size distributions were deduced from the LII signals at variable pressure using different heat-conduction models. Therefore, a detailed state-of-the art LII model has been developed that combined several commonly used heat conduction models and that focused on the correct modeling of the pressure influence on the LII signal. The particle sizes determined by LII were compared to independent measurements of the particle-size distribution from transmission-electron microscopy images, taken from soot samples from the flame. These investigations are important for quantitative applications of LII in practical high-pressure combustors like Diesel engines and gas turbines.

2 THEORETICAL BACKGROUND

A detailed understanding of the microphysical processes in laser-induced incandescence is required in order to interpret LII signals quantitatively. In this chapter, an overview on LII will be given and the underlying physics of the energy and mass balance in LII will be described.

2.1 Laser-induced incandescence

The LII signal is the thermal radiation from particles that are heated by an intense laser pulse. Subsequent cooling occurs due to several heat loss channels until, after a few hundreds of nanoseconds, the particle temperature reaches ambient gas temperature again. In general, any solid refractory or metallic particle, such as soot, that absorbs the laser radiation will incandesce – resulting in LII.

LII is basically used for two applications: The determination of the volume fraction of particles in an aerosol and in-situ particle sizing of gas-borne particles in the submicron region. LII was observed for the first time by Weeks and Duley in 1973 when they heated aerosols of carbon black and alumina with a CO_2 laser [15]. They set up the first energy balance describing the heat-up and cooling of particles by pulsed lasers and suggested that the method could be used for particle sizing. A few years later, Eckbreth observed the incandescence as an interference in Raman scattering experiments in sooting propane diffusion flames in 1977 [16]. In 1984, Melton set up the first detailed energy- and mass balance for LII and suggested to use LII as a tool for quantitative measurements of soot volume fractions [17]. In the same year, Dasch reported on the experimental investigation of the vaporization of soot with a Nd:YAG laser [18,19]. His study focussed on gas velocity measurements, flow visualization and point measurement of soot absorption. Little work has been performed on LII from then until the early 1990's. From then on, many investigations started and LII has been used successfully in a variety of systems for measuring volume fractions of soot in laminar diffusion flames [20-24], laminar premixed flames [25-28], and turbulent flames [20,29-31]. Particle sizes have been deduced from the temporal behavior of the LII signal taking the ratio of the LII signal at two different delay times after the signal peak [32,33] as well as using the entire decay curve in point measurements [27,34-37]. In exhaust gases, particle sizes have been measured with LII as well [38,39]. Particle sizes were obtained assuming monodisperse particles [27,35,36] as well as considering a polydisperse log-normal particle-size distribution [34,37]. Though LII has been used to investigate non-carbonaceous particles [10-12] with increasing interest in recent years with the upcoming nano sciences, the main focus has been in the field of soot diagnostics. In the following overview, LII will be discussed with respect to soot.

2.1.1 Soot volume fraction measurements

The first experimental applications of LII focussed on the determination of soot volume fractions. The soot volume fraction f_v is the fraction of the volume of soot in a given volume, given as

$$f_\mathrm{v} = \frac{1}{6}\pi N_\mathrm{d} d_\mathrm{p}^3 \tag{2.1}$$

where N_d is the number density of soot particles and d_p is the soot particle diameter. As LII emerged as a new tool in the field of laser diagnostics in combustion in the early 1990's, researchers applied the new technique in a similar way as the established laser-induced fluorescence (LIF) imaging [7,8]: Fields of soot volume fractions were measured by heating the soot particles with a laser light sheet of a pulsed Nd:YAG laser, the incandescence was spectrally filtered and detected temporally integrated ("gated") with an intensified CCD camera (ICCD) [20,22,24,25,40-42]. As suggested for the first time by Melton [17], the gated LII signal is, in the case of high laser fluences, roughly proportional to the soot volume fraction:

$$S_\mathrm{LII} = N_\mathrm{d} d_\mathrm{p}^{3+154\mathrm{nm}/\lambda_\mathrm{det}} \tag{2.2}$$

Here, λ_det is the detection wavelength – usually the center wavelength of a detection band pass in experimental applications. Although there have been many publications that show good agreement between LII and soot volume fractions obtained by other methods, e.g. light extinction [20,21,25-27], care must be taken to choose the right excitation and detection strategies, e.g. the choice of laser fluence, detection wavelength and detection gate, to ensure a correct quantification of the data [43,44]. Moreover, the calibration of LII with light extinction might be inaccurate if the calibration constant, which is obtained in a calibration flame with a given gas temperature, particle size and pressure, is transferred to other conditions [45]. Changes in the optical properties of soot influences the calibration as well: The absorption cross-section of soot, which influences both the absorption and emission characteristics due to Kirchhoff's law, is related to the soot absorption function $E(m)$. The value of $E(m)$ depends on the refractive index of soot which is related to some uncertainty as it differs significantly between soot from different sources (e.g. different flames) [46]. A value of $E(m)$ which is higher than that under calibration conditions will result in a larger absorption cross section of soot and will result in higher particle temperatures and, hence, in increased incandescence signal. This would result in an over-prediction of the soot volume fraction.

Therefore, researchers tried to find a different way of calibrating LII signals. A novel technique for quantifying soot volume fractions by LII has been given by Snelling [47]. The soot volume fraction is obtained from the temperature of the laser-heated particles. This can be done if the detection system is calibrated with a light source of known absolute light intensity. In such a way, the measurement is not affected by a change in particle temperature or by signal-light trapping.

Besides studies in laboratory flames, practical applications of LII have been performed in IC engines. Soot volume fractions were measured inside the combustion chamber of Diesel engines [38,48-53] as well as in engine exhaust gases [38,39,54].

2.1.2 Particle sizing

LII can be used to obtain particle sizes. The physical principal behind this idea is the fact that a small particle cools down faster than a large particle since a small particle has a larger surface to volume ratio than a large one. This results in a faster LII signal decay for small particles as shown in Figure 2.1.

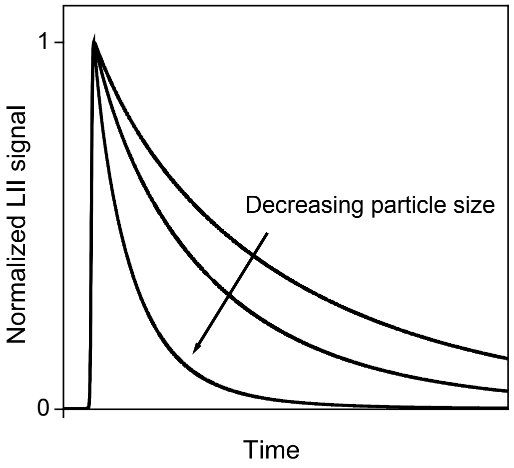

Figure 2.1. LII signal decay for different particle sizes.

Numerical models were set up and compared with experimental decay curves to obtain the particle size. Similar to the measurement of soot volume fractions, first applications focused on imaging measurements with ICCD cameras [32,33,55]. These experiments are based on the spatially two-dimensional detection of the LII signal at two different delay times after the signal peak. The ratio of these images is related to the particle size and a comparison with models yields absolute particle sizes.

However, it is more accurate to use the entire decay curve instead of only two single delay times. Models can be fitted to the full decay curve with the particle size as free fit parameter. Point measurements with fast photomultipliers yielded particle sizes in flames [27,34,36,56-58], shock tubes of both carbon and non-carbon materials [35,59,60], and in the combustion chamber of Diesel engines [37,61].

The information that is available from a single LII signal is not sufficient to obtain the particle size. Additional information is required to evaluate the particle size quantitatively:

The gas-phase temperature. The decay rate is influenced by the gas-phase temperature – a cold surrounding gas will force the particle to cool down faster. In flames, the gas-phase temperature can be obtained by soot pyrometry (in the case of constant temperature in the direction of detection) [62,63], coherent anti-Stokes Raman spectroscopy (CARS) [64,65], two-line atomic LIF [66] or multi-line NO-LIF thermometry [67,68].

The peak particle temperature. Similar to the gas-phase temperature, the peak particle temperature determines the decay rate. The peak particle temperature can be calculated from the absorption of laser light if the laser fluence and the absorption cross-section of the particle are known. However, both are subject to large uncertainty – the laser fluence due to unknown attenuation of laser light in the particle-laden gas, the absorption cross-section due to large differences in published values of *E(m)* [46]. Instead, the peak particle temperature can be measured by two-color pyrometry [34,57,61,69-71]. If the LII signal is detected at the two wavelengths λ_1 and λ_2, the peak particle temperature T_p^0 can be calculated from the peak signals $S_\mathrm{p}(\lambda_1, T_\mathrm{p}^0)$ and $S_\mathrm{p}(\lambda_2, T_\mathrm{p}^0)$ at the two wavelengths according to

$$T_p^0 = \frac{hc}{k_B}\left(\frac{1}{\lambda_2}-\frac{1}{\lambda_1}\right)\cdot\left[\ln\left[\frac{S_p(\lambda_1,T_p^0)}{S_p(\lambda_2,T_p^0)}\frac{K_2(\lambda_2)}{K_1(\lambda_1)}\frac{\varepsilon(\lambda_2)\lambda_1^{\,5}}{\varepsilon(\lambda_1)\lambda_2^{\,5}}\right]\right]^{-1} \tag{2.3}$$

where h is the Planck constant, c is the speed of light, k_B is the Boltzmann constant, S_p is the detected emission signal from the particles at the two detection wavelengths, and K_1 and K_2 are calibration constants that take into account the spectral sensitivity of the detectors at the two wavelengths. Finally, ε is the emissivity of the particles. The emissivity is a function of the refractive index of soot. In this case, however, the absolute value of $E(m)$ is not required; only the ratio of $E(m)$ at the two detection wavelengths is needed. The ratio $\varepsilon(\lambda_2)/\varepsilon_p(\lambda_1)$ can be approximated by λ_1/λ_2 assuming that $E(m)$ is constant between the two wavelengths. A careful choice of the detection wavelengths is necessary. In [13] a summary is given of the wavelengths used by different research groups. The reason for the wavelengths chosen is mainly to avoid interferences from C_2 fluorescence (which can be induced by the laser pulse that generates LII) and to choose a spectral range where the detection system is most sensitive.

Dispersion of the particle size. Particle sizes in a particle ensemble can be either mono- or polydisperse. In most practical systems, the particle sizes are polydisperse with a varying distribution width. This will influence the LII signal decay – it will be the sum of different particle sizes, weighted by the particle-size distribution. This behavior should be taken into account in the model and is described in section 2.2.9.

Aggregation. In real systems, nanosized particles tend to stick together and form aggregates. This will affect the particle cooling as well, and it must be known in which way aggregation influences the LII signal. Information about the structure and the number of primary particles per aggregate must be known. This will be described in detail in section 2.2.10.

2.2 Modeling laser-induced incandescence

Numerous models have been developed [17,33,54,61,72-74] to predict the temporal behavior of the LII signal. The basis for most models is an energy and mass balance that considers the absorption of laser energy and heat loss due to vaporization of material from the surface, heat conduction to the surrounding gas and radiation. Various submodels for the different heat-loss mechanisms have been suggested in the past. The energy balance for a single, spherical particle is shown in Figure 2.2. A more detailed model for soot particles including thermal annealing and oxidation has been developed by Michelsen [75].

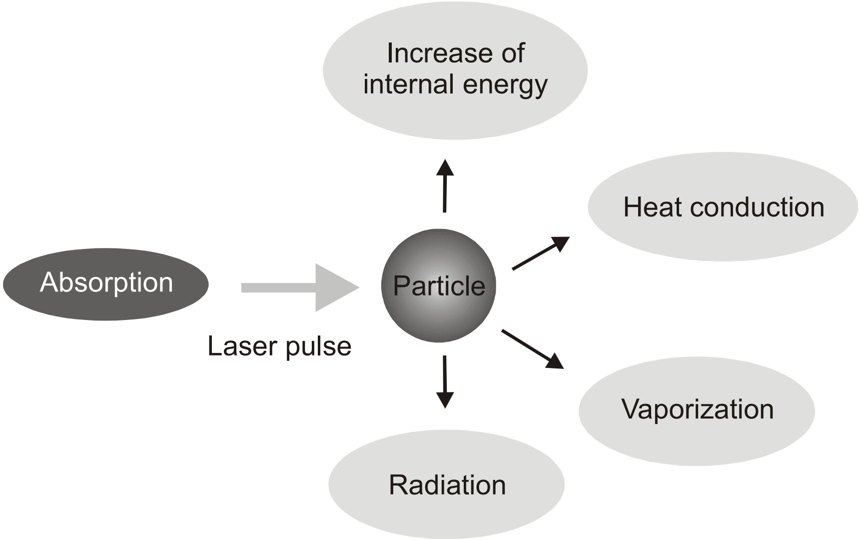

Figure 2.2. The energy balance of the LII process.

This energy balance can be written as

$$q_{\mathrm{abs}} = q_{\mathrm{int}} + q_{\mathrm{evap}} + q_{\mathrm{cond}} + q_{\mathrm{rad}} \tag{2.4}$$

where q_{abs} is the energy flux of laser absorption, q_{int} is the change in internal energy, q_{evap} is the energy flux due to evaporation, q_{cond} the energy flux related to heat conduction and q_{rad} the heat loss due to radiation. If the laser energy is sufficient to heat the particle above the vaporization threshold, carbon fragments will evaporate from the particle surface which will result in a mass loss of the particle and an increase of mass in the gas phase. This mass balance is described as

$$\mathrm{d}m_\mathrm{p} / \mathrm{d}t = J_\mathrm{evap} \tag{2.5}$$

with the particle mass m_p, the time t and the mass flux J_evap. The mass flux J_evap will be derived in section 2.2.6. Because one is mainly interested in the particle diameter instead of the particle mass equation 2.5 is written in dependence on the particle diameter d_p:

$$\frac{\mathrm{d}d_\mathrm{p}}{\mathrm{d}t} = \frac{2}{\rho_\mathrm{p} \pi d_\mathrm{p}^2} J_\mathrm{evap} \tag{2.6}$$

where ρ_p is the density of the particle. The resulting coupled differential equation given by the equations 2.4 and 2.6 can be solved numerically and yields the particle temperature and particle diameter as a function of time. The particle temperature is then turned into LII signal intensities using Planck's law.

In the following sections detailed expressions will be given for the sub-models of the energy and mass balance as well as the herein used physical and optical properties of the particle and the gas phase.

2.2.3 Laser absorption

The absorption of laser light by the particle is given by

$$q_\mathrm{abs} = C_\mathrm{abs} F(t) \tag{2.7}$$

The temporal intensity profile of the laser is given by the function $F(t)$ and is assumed to be Gaussian with 7 ns FWHM, a typical value for Q-switched Nd:YAG lasers. On the other hand, experimentally-measured laser profiles can be applied for $F(t)$. The spatial intensity profile of the laser is assumed to be rectangular, i.e. the fluence within the probe volume is homogeneously distributed and all particles are heated by the same laser fluence. Other spatial fluence distributions have been assumed in literature, e.g. a Gaussian distribution described by Bladh et al. [73].

If the particle is small compared to the laser wavelength, i.e. $\pi d_\mathrm{p}/\lambda < 0.3$, the absorption cross-section is given by [76,77]

$$C_\mathrm{abs} = \frac{\pi^2 d_p^3}{\lambda_\mathrm{ex}} E(m) \tag{2.8}$$

where λ_ex is the excitation wavelength and $E(m)$ is the soot-absorption function of the complex index of refraction m, given by

$$E(m) = -\mathrm{Im}\left(\frac{m^2 - 1}{m^2 + 2}\right) = \frac{6nk}{\left(n^2 - k^2 + 2\right)^2 + 4n^2k^2} \tag{2.9}$$

with the imaginary part k and the real part n of the complex index of refraction. The soot-absorption function is related to large uncertainties and affects the calculated peak particle temperature significantly. Various data about *E(m)* for flame and Diesel soot are available and are shown in Figure 2.3.

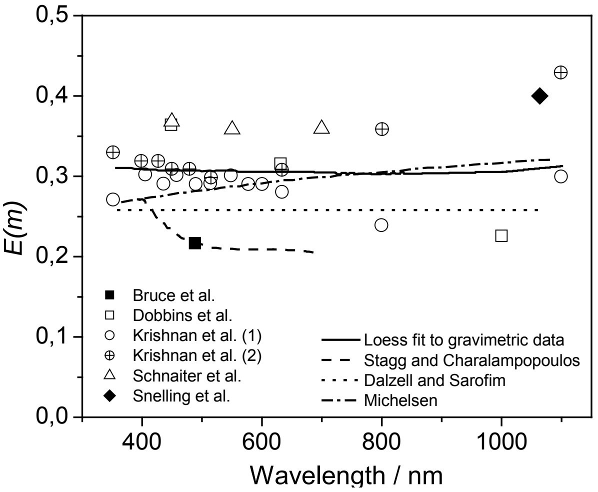

Figure 2.3. The soot absorption function for UV, visible and near-infrared wavelengths. Reproduced from [13].

A strong scatter between 0.2 and 0.4 can be observed for *E(m)* though there is no specific dependence on the wavelength within this scatter. This scatter may be related to different types of soot produced from different fuels and, therefore, to soot with different optical properties. The assumptions made to evaluate the soot-absorption function might affect the accuracy as well. For instance, data evaluated by Chang and Charalampopoulos [78] ignore the effect of aggregation and use data of graphite [13]. Additionally, those data were derived from soot at flame temperature (~1700 K), whereas *E(m)* of laser-heated soot (~3500 K) might be different. The value used for *E(m)* in this study is, unless otherwise noted, 0.4 as determined by Snelling from low-fluence LII measurements [71].

The default values used in the absorption term are summarized in Table 2.1.

Property	**Value**	**Source**
λ_{ex}	1064 nm	
E(m)	0.4	[71]
FWHM (laser)	7 ns	

Table 2.1. Values used for the absorption term.

2.2.4 Change in internal energy

The change in internal energy is given by

$$q_{\mathrm{int}} = \frac{\mathrm{d}\left(m_{\mathrm{p}} c_{\mathrm{p,s}} T_{\mathrm{p}}\right)}{\mathrm{d}t} \tag{2.10}$$

The heat capacity of soot $c_{\mathrm{p,s}}$ is expressed empirically in dependence on the particle temperature [61]:

$$c_{\mathrm{p,s}} = \frac{a_{\mathrm{c,s}} + b_{\mathrm{c,s}} T_{\mathrm{p}} + c_{\mathrm{c,s}} / T_{\mathrm{p}}^2}{M_{\mathrm{s}}} \tag{2.11}$$

where $a_{\mathrm{c,s}}$, $b_{\mathrm{c,s}}$ and $c_{\mathrm{c,s}}$ are empirical constants and M_{s} is the molar mass of graphite. Equation 2.10 can be written as

$$\begin{aligned} q_{\mathrm{int}} &= m_{\mathrm{p}} c_{\mathrm{p,s}} \frac{\mathrm{d}T_{\mathrm{p}}}{\mathrm{d}t} + m_{\mathrm{p}} T_{\mathrm{p}} \frac{\mathrm{d}c_{\mathrm{p,s}}}{\mathrm{d}t} + c_{\mathrm{p,s}} T_{\mathrm{p}} \frac{\mathrm{d}m_{\mathrm{p}}}{\mathrm{d}t} \\ &= m_{\mathrm{p}} c_{\mathrm{p,s}} \frac{\mathrm{d}T_{\mathrm{p}}}{\mathrm{d}t} + m_{\mathrm{p}} T_{\mathrm{p}} \frac{\mathrm{d}c_{\mathrm{p,s}}}{\mathrm{d}T_{\mathrm{p}}} \frac{\mathrm{d}T_{\mathrm{p}}}{\mathrm{d}t} + c_{\mathrm{p,s}} T_{\mathrm{p}} \frac{\mathrm{d}m_{\mathrm{p}}}{\mathrm{d}t} \end{aligned} \tag{2.12}$$

Here, m_{p} can be substituted by $\pi\rho_{\mathrm{p}} d_{\mathrm{p}}^3/6$, $\mathrm{d}m_{\mathrm{p}}/\mathrm{d}t$ by equation 2.5, and $\mathrm{d}c_{\mathrm{p,s}}/\mathrm{d}T_{\mathrm{p}}$ is obtained from equation 2.11:

$$\frac{\mathrm{d}c_{\mathrm{p,s}}}{\mathrm{d}T_{\mathrm{p}}} = \frac{b_{\mathrm{c,s}} - \dfrac{2c_{\mathrm{c,s}}}{T_{\mathrm{p}}^3}}{M_{\mathrm{s}}} \tag{2.13}$$

Combining equations 2.4, 2.12 and 2.13 and solving for $\mathrm{d}T_p/\mathrm{d}t$ results in

$$\frac{\mathrm{d}T_{\mathrm{p}}}{\mathrm{d}t} = \frac{q_{\mathrm{abs}} - q_{\mathrm{evap}} - q_{\mathrm{cond}} - q_{\mathrm{rad}} - J_{\mathrm{evap}} c_{\mathrm{p,s}} T_{\mathrm{p}}}{\frac{1}{6}\pi\rho_{\mathrm{p}} d_{\mathrm{p}}^3 \left(c_{\mathrm{p,s}} + T_{\mathrm{p}} \left(b_{\mathrm{c,s}} - \dfrac{2c_{\mathrm{c,s}}}{T_{\mathrm{p}}^3} \right) \Big/ M_{\mathrm{s}} \right)} \tag{2.14}$$

It should be noted that most models in literature use the expression $m_{\mathrm{p}} c_{\mathrm{p,s}} \mathrm{d}T_{\mathrm{p}}/\mathrm{d}t$ for the change in internal energy instead of equation 2.10. That expression ignores the change in internal energy due to the temperature dependence of the particle's heat capacity as well as the change in particle mass in case of high laser fluences. This can have a significant influence on the calculated temperature decay.

The default values used for the properties in the term for the change of the internal energy are summarized in Table 2.2.

Property	**Value**	**Source**
ρ_{p}	1860 kg m^{-3}	[61]
M_{s}	0.012011 kg mol^{-1}	
$a_{\mathrm{c,s}}$	22.5566 J mol^{-1} K^{-1}	[61]
$b_{\mathrm{c,s}}$	0.0013 J mol^{-1} K^{-2}	[61]
$c_{\mathrm{c,s}}$	-1819500 J K mol^{-1}	[61]

Table 2.2 Values used for the internal energy term.

2.2.5 Heat conduction

The heat conduction depends on the local gas-kinetic conditions that can be divided into three regimes: The free-molecular regime, the continuum regime and the transition regime. The regime of heat conduction is defined in terms of the ratio of two relevant length scales: the mean free path of gas molecules and the particle size. The resulting non-dimensional parameter is called the Knudsen number expressed as

$$Kn = \frac{\lambda_{MFP}}{L} \tag{2.15}$$

with the mean free path length of the gas molecules λ_{MFP} and the characteristic length L. In the case of heat conduction from a particle, the particle diameter or particle radius is taken for L. In this work, the particle radius is taken for L.

There is a gradual transition from the free-molecular regime to the continuum regime if the Knudsen number decreases. In the case of Knudsen numbers >> 1, typically $Kn > \sim 10$, heat conduction takes place in the free-molecular regime, which is the case for sooting flames at atmospheric pressure. For Knudsen numbers << 1, typically $Kn < \sim 0.01$, heat conduction takes place in the continuum regime. For Knudsen numbers around 1, heat conduction takes place in the transition regime, the regime that links the free-molecular and continuum regime. The relation between particle size and mean free path length for the three regimes is shown in Figure 2.4.

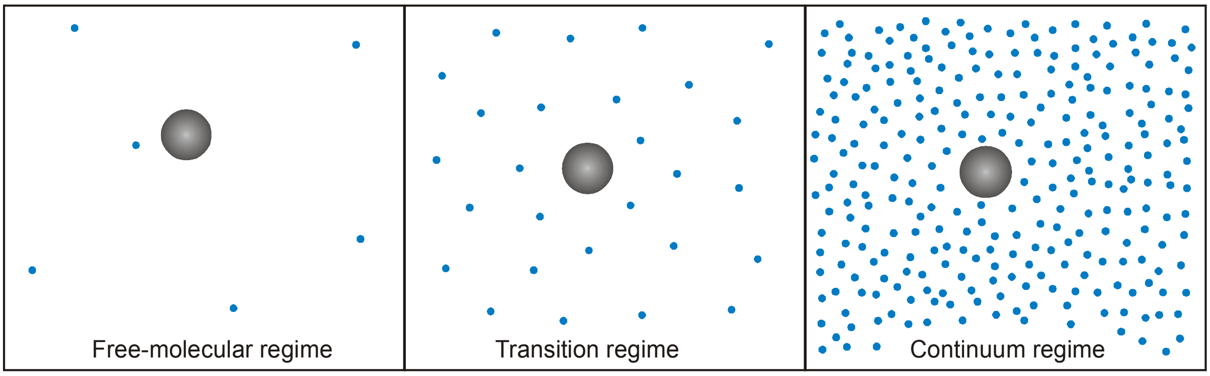

Figure 2.4. Relation between particle size (large gray circle) and mean free path length of the gas molecules (represented by small dots) for the three different Knudsen conditions.

The Boltzmann equation describes heat transfer in the most general way. While it is possible to solve this equation analytically in the free-molecular and the continuum regime, no detailed solution is available for the transition regime [79]. Hence, several approximating solutions were derived in the past. An overview on the different expressions for heat conduction for the three Knudsen conditions is given in the following subsections. A comprehensive overview on heat-conduction models in LII is given in [79].

The free-molecular regime

In the free-molecular regime, heat conduction is dominated by molecule-particle collisions. In the case of two concentric spheres and, hence, for a particle, heat conduction can be described by

$$q_{\mathrm{cond,FM}} = \alpha \pi d_p^2 \frac{p}{8} \sqrt{\frac{8RT_{\mathrm{g}}}{\pi M_{\mathrm{g}}}} \frac{\left(\gamma^* + 1\right)}{\left(\gamma^* - 1\right)} \left(\frac{T_{\mathrm{p}}}{T_{\mathrm{g}}} - 1\right) \tag{2.16}$$

where R is the universal gas constant, p is the gas pressure, α is the thermal accommodation coefficient, M_{g} is the molar mass of the gas and T_{g} is the gas temperature. The average heat capacity ratio γ^* is defined by Filippov and Rosner [80] as

$$\frac{1}{\gamma^* - 1} = \frac{1}{T_p - T_g} \int_{T_g}^{T_p} \frac{dT}{\gamma - 1} \tag{2.17}$$

Remember that γ is a function of temperature since it is the heat capacity ratio $c_{\mathrm{p}}/c_{\mathrm{v}}$ and heat capacities are temperature dependent. In literature, the heat capacity ratio γ is often applied at constant gas phase temperature. It has been pointed out by Liu et al. [79], that the average heat capacity ratio should be used if the temperature difference between the particle and the surrounding gas is large. Otherwise, the heat conduction will be underestimated, except for mono-atomic (noble) gases which have a temperature-independent heat capacity.

The thermal accommodation coefficient α was introduced by Knudsen in 1911 [81]. The thermal accommodation coefficient is the fraction of heat transferred by a gas molecule that collides with a surface. Before the collision, the colliding gas molecule's temperature equals the bath gas temperature. In the case of complete accommodation, i.e. $\alpha = 1$, the gas molecules leave the particle's surface with the temperature of the particle. In the case of zero accommodation, i.e. $\alpha = 0$, the reflected gas molecule is still at the same temperature as before the collision and has effectively not carried away energy from the surface. The value of the accommodation coefficient has a large impact on the heat conduction as heat conduction at given collision frequencies scales linearly with α. It depends on the nature of the gas molecules. For instance, LII experiments of pure carbon upon the flash photolysis of carbon suboxid, C_2O_3, in different bath gases yielded values of $\alpha = 0.44$ in Argon and CO, whereas a value of $\alpha = 0.1$ was found in the case of Helium [82]. Smallwood an coworkers [71] determined a value of 0.37 in an atmospheric ethylene/air diffusion flame. Hence, it is difficult the choose a value for α. A frequently used value for α in flames in literature is 0.3 [13], which has been used in this work as well.

The continuum regime

In the continuum regime, heat transfer between the particle and the surrounding gas is diffusion-controlled and, in contrast to the free-molecular regime, molecule-molecule collisions dominate over molecule-particle collisions. Compared to the free-molecular regime, however, molecule-particle collisions and, hence, heat conduction are strongly increased. As described by Filippov and Rosner [80] the heat flux can be expressed as

$$q_{\mathrm{cond,C}} = 2\pi d_{\mathrm{p}} \int_{T_{\mathrm{g}}}^{T_{\mathrm{p}}} k_{\mathrm{g}} \mathrm{d}T \tag{2.18}$$

This expression should be used in the case of large temperature differences between the particle and the surrounding gas. The thermal conductivity of the surrounding gas k_{g} is temperature dependent. In this work, the expression given by Michelsen [75] for air has been used:

$$k_{\mathrm{g}} = h_1 + h_2 T_{\mathrm{g}} \tag{2.19}$$

For small temperature differences, equation 2.18 simplifies to the commonly used Fourier law of heat conduction:

$$q_{\mathrm{cond,C}} = 2\pi d_{\mathrm{p}} k_{\mathrm{g}} \left(T_{\mathrm{p}} - T_{\mathrm{g}}\right) \tag{2.20}$$

Equation 2.18 can be written in the form of Fourier's law as

$$q_{\mathrm{cond,C}} = 2\pi d_{\mathrm{p}} k_{\mathrm{g}}^{*} \left(T_{\mathrm{p}} - T_{\mathrm{g}}\right) \tag{2.21}$$

with the *average* thermal heat conductivity of the bath gas that is given as

$$k_{\mathrm{g}}^{*} = \int_{T_{\mathrm{g}}}^{T_{\mathrm{p}}} \frac{k_{\mathrm{g}}}{T_{\mathrm{p}} - T_{\mathrm{g}}} \mathrm{d}T \tag{2.22}$$

The importance of the use of an average value for the thermal conductivity has been emphasized by Liu et al. [79] and is shown in this work in Figure 2.5. Here, the heat conduction has been calculated for a single, spherical particle in air with d_{p} = 32 nm at a temperature of T_{p} = 3400 K for different gas temperatures. For small temperature ratios, equations 2.18 and 2.20 give similar results, whereas they differ significantly at low gas temperatures, i.e. large temperature differences between particle and bath gas. In the case of Fourier's law with a fixed thermal conductivity at the gas temperature T_{g}, a maximum appears at ~1700 K since the increase in heat conduction due to an increase in the temperature difference T_{p}–T_{g} is compensated by a decrease of the heat conduction due to a decrease of the thermal conductivity of air with decreasing temperature. Hence, Fourier's law with the average value of k_{g} should be used, as this is the more accurate expression, and large differences are observed compared to the simplified expression 2.20.

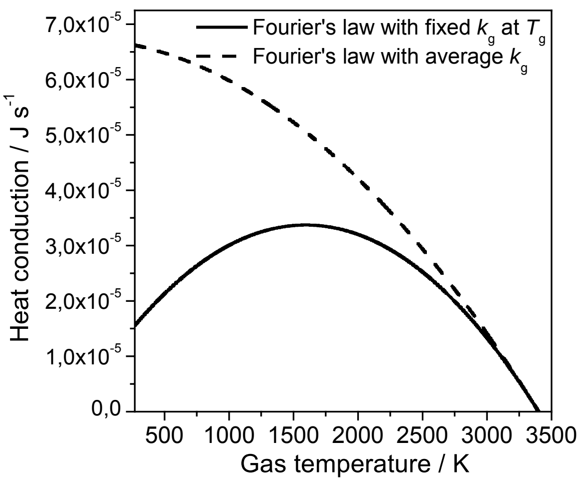

Figure 2.5. Heat conduction in the continuum regime for a spherical particle of 32 nm diameter at a temperature of 3400 K using Fourier's law with a fixed (solid line) and averaged (dashed line) thermal conductivity respectively.

The continuum regime will hardly be reached in typical LII applications. For instance, assuming a spherical particle of 120 nm diameter (which is about double the size of typical soot particles) and a gas temperature of 300 K, a Knudsen number of 0.01 requires a pressure of 110 bar. In the transition regime, however, some models use an interpolation between the free-molecular and the continuum regime and the use of a wrong sub-model for the continuum regime will affect the transition regime as well.

The transition regime: McCoy and Cha

A commonly-used heat conduction model for LII in the transition regime was given by Melton [17]. It is based on the work of McCoy and Cha [83] who derived the following expression for two concentric spheres in the transition regime:

$$q_{\mathrm{cond,Trans}} = \frac{2k_{\mathrm{g}}(T_{\mathrm{g}})\pi d_{\mathrm{p}}^{2}\left(T_{\mathrm{p}} - T_{\mathrm{g}}\right)}{\left(d_{\mathrm{p}} + G\lambda_{\mathrm{MFP}}\right)} \tag{2.23}$$

Here, the mean free path length is

$$\lambda_{\mathrm{MFP}} = \frac{k_{\mathrm{g}}(T_{\mathrm{g}})}{f(T_{\mathrm{g}})p}\left(\gamma(T_{\mathrm{g}}) - 1\right)\sqrt{\frac{\pi M_{\mathrm{g}} T_{\mathrm{g}}}{2R}} \tag{2.24}$$

It has been pointed out by Liu et al. [79] that it is of high importance to use expression 2.24 in the case of the heat-conduction model of McCoy and Cha. If the often used expression for hard spheres is used, i.e. $\lambda_{\mathrm{MFP}} = k_{\mathrm{B}}T_{\mathrm{g}}/(\sqrt{2}\Sigma_{\mathrm{g}}p)$, large deviations occur for the heat-conduction rate using equation 2.23.

In 2.23 the factor G is

$$\frac{8f}{\alpha(\gamma + 1)} \tag{2.25}$$

in which the Euckenfactor f [84] is

$$f = \frac{9\gamma - 5}{4} \tag{2.26}$$

To calculate the heat capacity ratio γ of the gas, the temperature-dependent heat capacity of the gas $c_{\mathrm{p,g}}$ is required. It is given by [61]

$$c_{\mathrm{p,g}} = a_{\mathrm{c,g}} + b_{\mathrm{c,g}} T_{\mathrm{g}} + \frac{c_{\mathrm{c,g}}}{T_{\mathrm{g}}^2} \tag{2.27}$$

The heat-conduction model of McCoy and Cha can be used for all Knudsen regimes as it provides a smooth transition between the free-molecular and the continuum regime.

The transition regime: Fuchs' approach

Fuchs' approach [85,86] is based on the assumption that heat conduction from a particle to the surrounding gas in the transition regime can be divided into two zones. The boundary between the two zones is given by a sphere of thickness δ around the particle. This boundary layer δ is in the order of the mean free path length of the gas molecules. Inside this limiting sphere heat conduction is assumed to follow the mechanisms of the free-molecular flow, whereas outside the sphere heat conduction takes place according to the continuum regime as shown in Figure 2.6. The particle has the temperature T_{p}, the temperature inside the limiting sphere is T_δ and outside the sphere the gas has the temperature T_{g}.

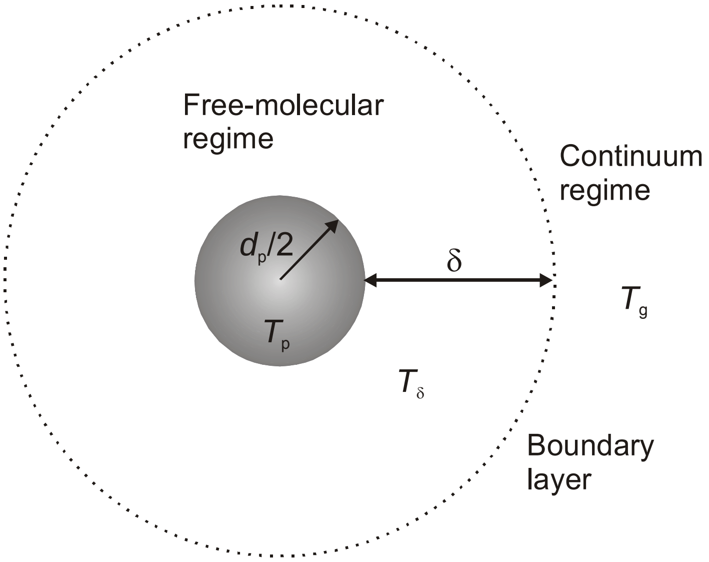

Figure 2.6. Heat-conduction for a spherical particle in the transition regime according to the two-layer model of Fuchs.

The key point in using the Fuchs model is to find the values for the thickness of the boundary layer and the temperature inside this limiting sphere. Filippov and Rosner [80] describe the required equations to calculate δ and T_δ. The thickness of the limiting sphere can be calculated as

$$\delta = \frac{(d_\mathrm{p}/2)^3}{\lambda^2_{\mathrm{MFP},\delta}}\left(\frac{1}{5}\Lambda_1^5 - \frac{1}{3}\Lambda_2\Lambda_1^3 + \frac{2}{15}\Lambda_2^{5/2}\right) - \frac{d_\mathrm{p}}{2} \tag{2.28}$$

with the mean free path inside the sphere $\lambda_{\mathrm{MFP},\delta}$ and the coefficients:

$$\Lambda_1 = 1 + \frac{\lambda_{\mathrm{MFP},\delta}}{d_\mathrm{p}/2}; \quad \Lambda_2 = 1 + \left(\frac{\lambda_{\mathrm{MFP},\delta}}{d_\mathrm{p}/2}\right)^2 \tag{2.29}$$

The mean free path inside the sphere can be calculated with equation 2.24 with T_δ instead of T_g:

$$\lambda_{\mathrm{MFP},\delta} = \frac{k_\mathrm{g}(T_\delta)}{f(T_\delta)p}\left(\gamma(T_\delta) - 1\right)\sqrt{\frac{\pi M_\mathrm{g} T_\delta}{2R}} \tag{2.30}$$

Hence, with known pressure and molecular mass of the gas, δ is only a function of temperature in the boundary layer.

The heat conduction inside the boundary layer is expressed by equation 2.16 and 2.17 with T_δ instead of T_g:

$$q_{\mathrm{cond,FM}} = \alpha\pi d_\mathrm{p}^2 \frac{p}{8}\sqrt{\frac{8RT_\delta}{\pi M_\mathrm{g}}}\frac{\left(\gamma^* + 1\right)}{\left(\gamma^* - 1\right)}\left(\frac{T_\mathrm{p}}{T_\delta} - 1\right) \tag{2.31}$$

Notice the use of two different values of γ for the free-molecular part: An average value γ^* is used between T_δ and T_p in 2.31, whereas in 2.30 γ at the fixed temperature T_δ is used to calculate the mean free path in the boundary layer. According to Liu (private communication) the mean free path of the gas molecules is a concept of gas at equilibrium. Therefore, the value of γ should be calculated at the equilibrium state of the gas, i.e. either T_g or T_δ in the case of the boundary layer.

Heat conduction outside the limiting sphere follows the model for the continuum regime. The "particle diameter" is the diameter of the boundary layer, i.e. the radius is $\delta + d_\mathrm{p}/2$. If this value is inserted in equation 2.18 and T_p is substituted by T_δ one obtains for the heat conduction outside the sphere

$$q_{\mathrm{cond,C}} = 4\pi(\delta + d_\mathrm{p}/2)\int_{T_\mathrm{g}}^{T_\delta} k_\mathrm{g}\,\mathrm{d}T \tag{2.32}$$

The next step is to obtain T_δ. As there are no sources or sinks of heat, equations 2.31 and 2.32 must be equal. With that relation and with equations 2.28 – 2.30 T_δ and successively δ can be determined by solving this combination of expressions numerically. Then, the heat conduction in the transition regime can be calculated by using either 2.31 or 2.32.

The values used for the properties in the heat conduction term are listed in Table 2.3.

Property	Value	Source
M_g	$28 \cdot 10^{-3}$ kg mol^{-1}	Molecular mass of nitrogen
$a_\mathrm{c,g}$	28.58 J mol^{-1} K^{-1}	[61]
$b_\mathrm{c,g}$	0.00377 J mol^{-1} K^{-2}	[61]
$c_\mathrm{c,g}$	-50 kJ K mol^{-1}	[61]
h_1	$1.08 \cdot 10^{-2}$ W m^{-1} K^{-1}	[75]
h_2	$5.15 \cdot 10^{-5}$ W m^{-1} K^{-2}	[75]

Table 2.3. Values used for the conduction term.

2.2.6 Vaporization

If the laser fluence is high and, therefore, the particles reach high temperatures, soot fragments can evaporate from the particle's surface. The amount of heat loss due to evaporation is given by the enthalpy of vaporization of soot, $\Delta H_\mathrm{v,s}$, the molar mass of the soot vapor $M_\mathrm{v,s}$ and the rate of mass loss $\mathrm{d}m_\mathrm{p}/\mathrm{d}t$:

$$q_\mathrm{evap} = \frac{\Delta H_\mathrm{v,s}}{M_\mathrm{v,s}} \frac{\mathrm{d}m_\mathrm{p}}{\mathrm{d}t} \tag{2.33}$$

The mass balance takes into account that the mass which evaporates from the particle will be in the gas phase:

$$\frac{\mathrm{d}m_\mathrm{p}}{\mathrm{d}t} = -\pi d_\mathrm{p}^2 N_\mathrm{v,s} \frac{M_\mathrm{v,s}}{N_\mathrm{A}} = J_\mathrm{evap} \tag{2.34}$$

Here, $N_\mathrm{v,s}$ is the flux of molecules that leave the surface in the transition regime. The molecular flux in the transition regime can be expressed by the fluxes in the free-molecular regime, $N_\mathrm{FM,s}$, and the continuum regime, $N_\mathrm{C,s}$ [54]:

$$N_\mathrm{v,s} = \left(\frac{1}{N_\mathrm{FM,s}} + \frac{1}{N_\mathrm{C,s}} \right)^{-1} \tag{2.35}$$

The flux in the free-molecular regime can be expressed by

$$N_\mathrm{FM,s} = \beta \frac{p_\mathrm{v,s}}{k_\mathrm{B} T_\mathrm{p}} \sqrt{\frac{R T_\mathrm{p}}{2\pi M_\mathrm{v,s}}} \tag{2.36}$$

with the vapor pressure $p_\mathrm{v,s}$ of the evaporating carbon species and the evaporation coefficient β which is a number between 0 and 1 and can be used to adjust the efficiency of the evaporation. Usually, β is set to 1. The flux in the continuum regime can be expressed by

$$N_\mathrm{C,s} = 2 \frac{p_\mathrm{v,s}}{k_\mathrm{B} T_\mathrm{P}} \frac{\Gamma_\mathrm{v,s}}{d_\mathrm{p}} \tag{2.37}$$

The diffusion coefficient of the soot vapor, $\Gamma_{\mathrm{v,s}}$, is given by Michelsen [75]:

$$\Gamma_{\mathrm{v,s}} = \frac{f k_{\mathrm{B}} T_{\mathrm{p}}}{4\Sigma_{\mathrm{v,s}} p} \sqrt{\frac{R T_{\mathrm{p}}}{\pi M_{\mathrm{v,s}}}} \tag{2.38}$$

Here, $\Sigma_{\mathrm{v,s}}$ is the molecular cross section of the vapor. The question is which soot fragments evaporate from the surface. An overview on the evaporating carbon species in dependence on temperature is given by Leider et al. [87]. The dominant species above ~2000 K is C_3, though all species from $C_1 - C_7$ are present in the vapor in different concentrations. In this work, the species $C_1 - C_7$ are considered. The vapor pressure, molecular weight of the soot vapor and the enthalpy of vaporization are required as a function of the particle temperature. Smallwood and coworkers [88] derived these expressions from polynomial fits to data from Leider et al. The expressions are

$$p_{\mathrm{v,s}} = \exp\left(\sum_{i=0}^{5} p_i T_{\mathrm{p}}^i \right), \tag{2.39}$$

$$M_{\mathrm{v,s}} = \sum_{i=0}^{5} m_i T_{\mathrm{p}}^i , \tag{2.40}$$

$$\Delta H_{\mathrm{v,s}} = \sum_{i=0}^{5} h_i T_{\mathrm{p}}^i , \tag{2.41}$$

Finally, the molecular cross-sections of the vapor molecules are required. Michelsen [75] has given the molecular cross-sections for the species $C_1 - C_{10}$. For this work, the data of Michelsen were fitted as function of the molecular weight of the vapor. In that way, a polynomial expression for the molecular cross-section of the soot vapor could be derived:

$$\Sigma_{\mathrm{v,s}} = \sum_{i=0}^{5} \sigma_i M_{\mathrm{v,s}}^i \tag{2.42}$$

The dependencies of $p_{\mathrm{v,s}}$, $M_{\mathrm{v,s}}$, $\Delta H_{\mathrm{v,s}}$ on temperature and of $\Sigma_{\mathrm{v,s}}$ on the molar mass of the vapor are shown in Figure 2.7.

The coefficients for the polynoms 2.39 – 2.42 are listed in Table 2.4. The coefficients will result in SI units for $p_{\mathrm{v,s}}$, $M_{\mathrm{v,s}}$, $\Delta H_{\mathrm{v,s}}$ and $\Sigma_{\mathrm{v,s}}$.

i	p_i	m_i	h_i	s_i
0	-111.44	0.017179	205398	$1.8\cdot10^{-19}$
1	0.090558	$6.8654\cdot10^{-7}$	736.6	$-1.8574\cdot10^{-17}$
2	$-2.7637\cdot10^{-5}$	$2.9962\cdot10^{-9}$	-0.40713	$1.40368\cdot10^{-15}$
3	$4.1754\cdot10^{-9}$	$-8.5954\cdot10^{-13}$	$1.1992\cdot10^{-4}$	$-2.5926\cdot10^{-14}$
4	$-2.4875\cdot10^{-13}$	$1.0486\cdot10^{-16}$	$-1.7946\cdot10^{-8}$	$2.07484\cdot10^{-13}$
5	0	0	$1.0717\cdot10^{-12}$	$-6.6673\cdot10^{-13}$

Table 2.4. Coefficients for the polynomial expressions of the vapor pressure, molecular mass of the vapor, enthalpy of vaporization and molecular cross-section of the vapor.

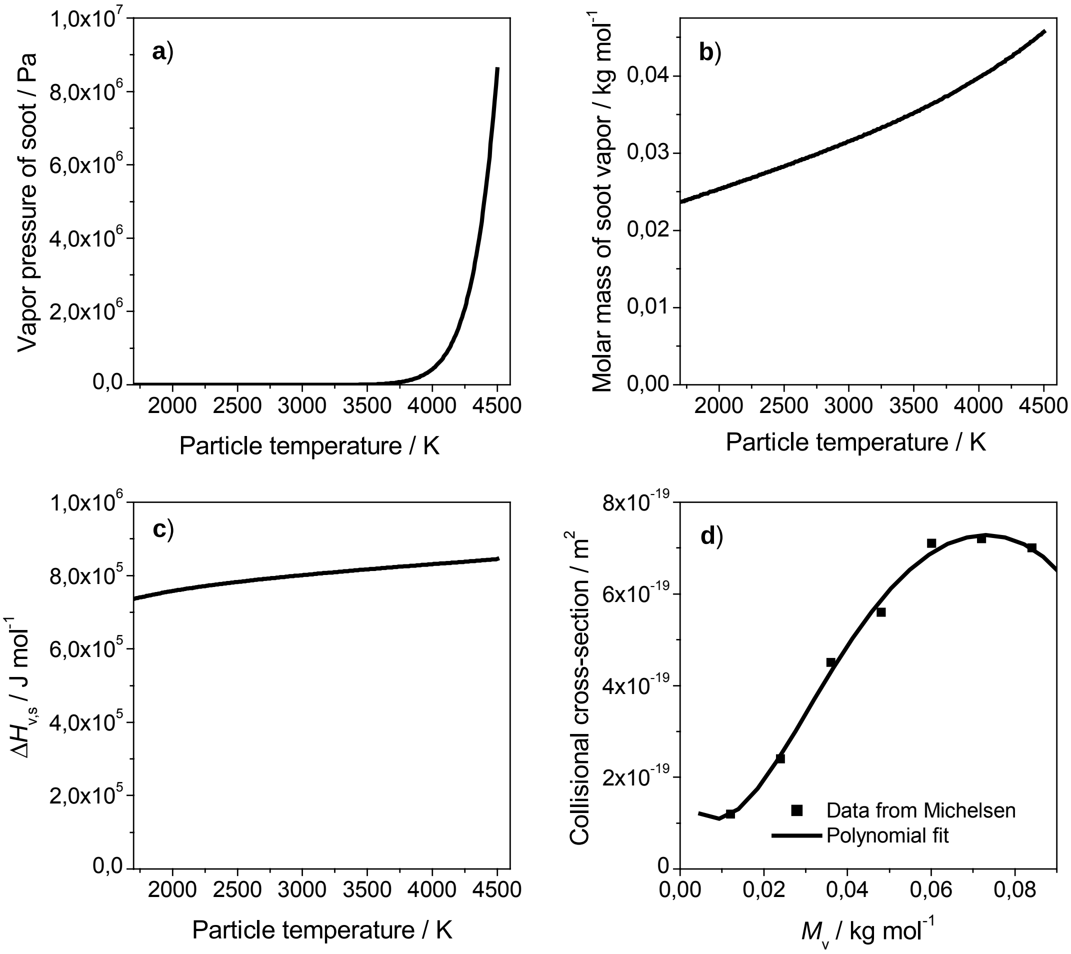

Figure 2.7. Dependencies of $p_{v,s}$ (a), $M_{v,s}$ (b), $\Delta H_{v,s}$ (c), on temperature and of $\Sigma_{v,s}$ (d) on the molar mass of the vapor.

2.2.7 Radiation

The heat loss due to radiation follows the Stefan-Boltzmann law. The emitted power over all wavelengths is

$$q_{\mathrm{rad}} = \pi d_{\mathrm{p}}^{2} \theta \sigma_{\mathrm{B}} \left(T_{\mathrm{p}}^{4} - T_{\mathrm{g}}^{4} \right) \tag{2.43}$$

Here, σ_B is the Stefan-Boltzmann constant and θ the total emission coefficient. Assuming black body radiation, θ is set to 1. This is a simplified expression, as soot is not a perfect black body. The difference is, however, negligible, as radiation has only a minor contribution to the heat loss under the conditions in this work, i.e. at atmospheric or high pressure. This will be shown in chapter 3.

2.2.8 Final energy and mass balance and LII signal

In order to calculate the LII signal, the energy and mass balance equations 2.4 and 2.6 have to be solved for T_p and d_p. The final energy balance is obtained from equations 2.4 and 2.14, the final mass balance from equations 2.6 and 2.34:

$$\frac{\mathrm{d}T_\mathrm{p}}{\mathrm{d}t}=\frac{q_\mathrm{abs}-q_\mathrm{evap}-q_\mathrm{cond}-q_\mathrm{rad}+\pi d_\mathrm{p}^2 N_\mathrm{v,s}\dfrac{M_\mathrm{v,s}}{N_\mathrm{A}}c_\mathrm{p,s}T_\mathrm{p}}{\dfrac{1}{6}\pi\rho_\mathrm{p}d_\mathrm{p}^3\left(c_\mathrm{p,s}+T_\mathrm{p}\left(b_\mathrm{c,s}-\dfrac{2c_\mathrm{c,s}}{T_\mathrm{p}^3}\right)\Big/M_\mathrm{s}\right)} \tag{2.44}$$

$$\frac{\mathrm{d}d_\mathrm{p}}{\mathrm{d}t}=2\frac{N_\mathrm{v,s}M_\mathrm{v,s}}{\rho_\mathrm{p}N_\mathrm{A}} \tag{2.45}$$

This is a coupled, first-order differential equation. It is numerically solved with a fourth-order Runge-Kutta algorithm. This yields the temperature, the particle diameter as well as the contributions of the different heat-loss mechanisms as a function of time.

Finally, the particle temperature has to be turned into LII signal intensity. This is done using Planck's law since the particle radiation is near black-body radiation. In order to obtain the effective LII signal, the signal of the radiating background, i.e. the soot at gas temperature, is subtracted. Hence, the contribution to the signal from each particle in the detection volume is given by

$$S_\mathrm{LII}=\pi d_\mathrm{p}^2\int_{\lambda_1}^{\lambda_2}\Omega(\lambda)\varepsilon(\lambda)2\pi hc^2\left[\frac{1}{\lambda^5\left[\exp\left(hc/\lambda k_\mathrm{B}T_\mathrm{p}\right)-1\right]}-\frac{1}{\lambda^5\left[\exp\left(hc/\lambda k_\mathrm{B}T_\mathrm{g}\right)-1\right]}\right]\mathrm{d}\lambda \tag{2.46}$$

with the spectral response function of the detection system Ω and the spectral emissivity of soot ε. The emissivity is related to the absorption cross-section and is given by [75]

$$\varepsilon=\frac{4C_\mathrm{abs}}{\pi d_\mathrm{p}^2}=\frac{4\pi d_\mathrm{p}E(m)}{\lambda_\mathrm{det}} \tag{2.47}$$

The signal is integrated over the detection bandpass from λ_1 to λ_2.

2.2.9 Polydisperse particle-size distributions

In most cases, the particles within the probe volume are not monodisperse but polydisperse. This will have a significant impact on the LII signal as the cooling of the laser-heated particles strongly depends on the particle size. It has been shown that for hydrocarbon flames at atmospheric and elevated pressure [89] the particles' size distribution follows a log-normal distribution given by

$$df = \frac{1}{\sqrt{2\pi}\, d_{\mathrm{p}} \ln\sigma_{\mathrm{g}}} \exp\left[-\frac{\left(\ln d_{\mathrm{p}} - \ln CMD\right)^2}{2\left(\ln\sigma_{\mathrm{g}}\right)^2}\right] \mathrm{d}d_{\mathrm{p}} \tag{2.48}$$

The distribution is characterized by the count median diameter *CMD* and the geometric width σ_{g}. *df* is the probability to find a particle size between d_{p} and $d_{\mathrm{p}} + \mathrm{d}d_{\mathrm{p}}$. The distribution is not symmetric but has a long tail towards larger particles. Some examples for different values of the count median diameter and the geometric width are shown in Figure 2.8.

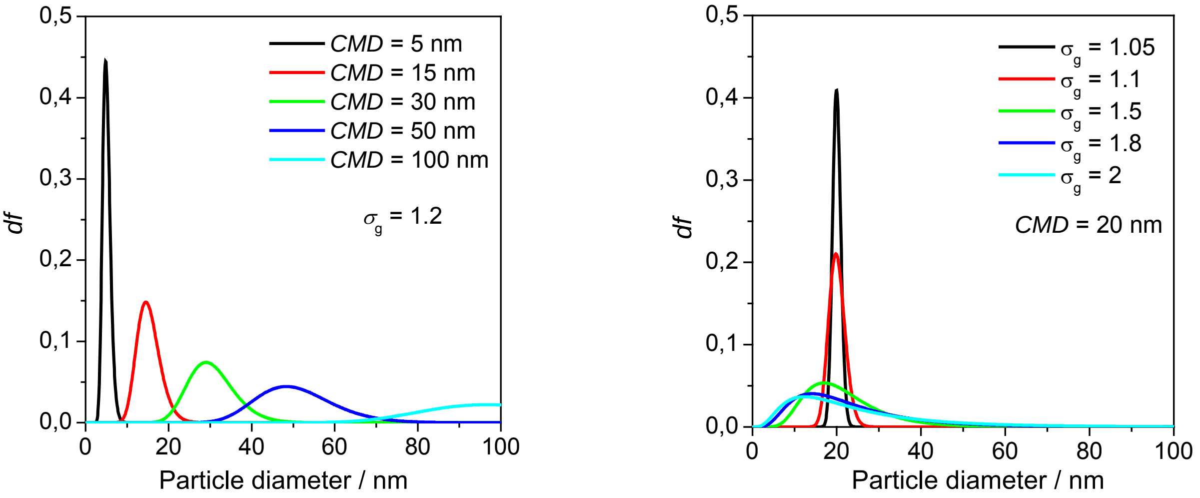

Figure 2.8. Log-normal distribution for a fixed geometric width of 1.2 with different CMD (left) and a fixed CMD with different geometric widths (right).

For the simulation of LII signals, a log-normal particle-size distribution can be considered if the LII signal is calculated for different individual particle sizes. The resulting signal contributions are then weighted by the probability *df* for a given particle diameter. The final signal for the distribution is obtained by integrating over all signals.

2.2.10 Influence of aggregates

So far, the process of modeling LII has been based on the calculation of the energy and mass balance for single, spherical particles. In real samples, however, the primary particles tend to form larger aggregates [90-93]. A schematic picture of an aggregate and a TEM image of soot from a premixed ethylene/air flame at 2 bar is shown in Figure 2.9. It can be seen that aggregates consist of several, spherical primary particles that “stick” together and form chains which split up in different branches. This results in a fractal structure of the aggregate. The contact between the individual primary particles can be point-wise although a “bridging” contact is possible as well.

The fractal structure can be described by the statistical scaling law [94]

$$N_{\mathrm{p}} = k_{\mathrm{f}} \left(\frac{R_{\mathrm{g}}}{d_{\mathrm{p}}/2}\right)^{D_{\mathrm{f}}} \tag{2.49}$$

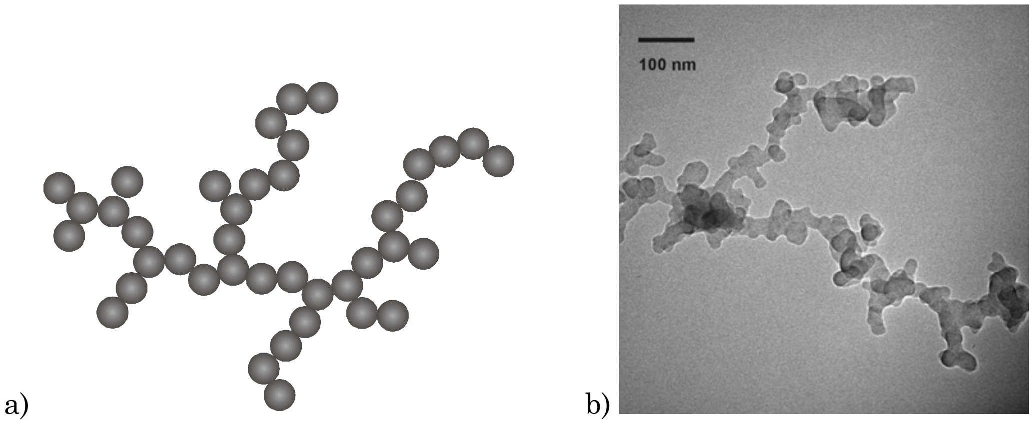

Figure 2.9. Schematic picture of an aggregate (a) and a TEM image of aggregated flame soot (b).

where N_p is the number of primary particles per aggregate, k_f and D_f are the fractal prefactor and fractal dimension respectively, and R_g is the radius of gyration. The fractal dimension is a statistical quantity that gives an indication of how completely a fractal structure fills the space, i.e. how open or close the structure of the aggregate is. The radius of gyration is defined via the mean square of the distance between the centers of primary particles and the geometrical center of mass of the aggregate:

$$R_\mathrm{g}^2 = \frac{1}{N_\mathrm{p}} \sum_{i=1}^{N_\mathrm{p}} (r_i - r_0)^2, \qquad r_0 = \frac{1}{N_\mathrm{p}} \sum_{i=1}^{N_\mathrm{p}} r_i \tag{2.50}$$

where r_i is the position vector of the i^th primary particle in the aggregate under consideration.

To include the effect of aggregation in the energy and mass balance, the LII process must be solved for an aggregate instead of a single particle. Following Liu et al. [95] some assumptions are made:

- The primary particles are in point contact
- The primary soot particle diameters are uniform within an aggregate of size N_p (containing N_p primary soot particles), but are allowed to vary from aggregate to aggregate, i.e. according to the polydisperse particle-size distribution described in section 2.2.9
- The potentially non-uniform temperature distribution among primary soot particles within an aggregate are neglected.

The LII model modifications for aggregates were presented for the first time by Snelling et al. [71] and were improved by Liu and coworkers [95,96]. Following Rayleigh-Debye-Gans polydisperse-fractal-aggregate (RDG-PFA) theory, the laser absorption rate is not affected by aggregation, but scales linearly with the number of primary particles within an aggregate [97,98]. Hence, equation 2.7 can be written as

$$q_\mathrm{abs} = N_\mathrm{p} C_\mathrm{abs} F(t) \tag{2.51}$$

The change in internal energy scales linearly with the number of primary particles as well and equation 2.10 can be written as

$$q_{\mathrm{int}} = \frac{\mathrm{d}\left(N_{\mathrm{p}} m_{\mathrm{p}} c_{\mathrm{p,s}} T_{\mathrm{p}}\right)}{\mathrm{d}t} \tag{2.52}$$

Concerning the heat loss due to radiation, it results from RDG-PFA theory again that radiation is not affected by aggregation and equation 2.43 is written as

$$q_{\mathrm{rad}} = N_{\mathrm{p}} \pi d_{\mathrm{p}}^2 \theta \sigma_{\mathrm{B}} \left(T_{\mathrm{p}}^4 - T_{\mathrm{g}}^4\right) \tag{2.53}$$

Heat conduction, however, is affected by aggregation. In the case of aggregates a “shielding” effect occurs: Particles inside the aggregate are shielded against collisions with gas molecules by surrounding particles in the aggregate. The heat conduction for aggregates is described by introducing an “effective” diameter D_{eff} that is the diameter of an equivalent single, solid sphere that has the same energy-transfer surface area as the aggregate. This is illustrated in Figure 2.10.

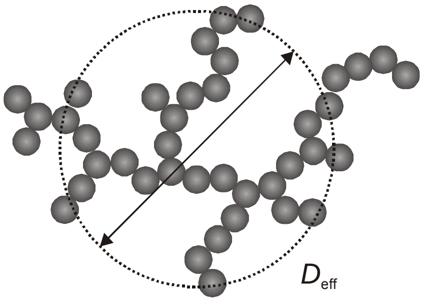

Figure 2.10. Effective heat-transfer diameter of an aggregate.

The effective particle diameter is related to d_{p} and N_{p} through [99]

$$D_{\mathrm{eff}} = \left(\frac{N_{\mathrm{p}}}{k_{\mathrm{h}}}\right)^{1/D_{\mathrm{h}}} d_{\mathrm{p}} \tag{2.54}$$

with the scaling parameters D_{h} and k_{h}. This relation was derived for the free-molecular regime and for a thermal accommodation coefficient of $\alpha = 1$. It was based on direct simulation Monte Carlo (DSMC) calculations in conjunction with numerically-generated aggregates for values of the fractal dimension $D_{\mathrm{f}} = 1.78$ and the fractal prefactor $k_{\mathrm{f}} = 2.3$ which are typical values for soot aggregates. However, the thermal accommodation coefficient in real systems is much smaller than unity. Therefore, Liu et al. [95] used DSMC calculations and numerically-generated aggregates to determine the scaling parameters D_{h} and k_{h} as function of α. With the same input values as Filippov et al. ($D_{\mathrm{f}} = 1.78$ and $k_{\mathrm{f}} = 2.3$) they obtained for k_{h} and D_{h}

$$k_{\mathrm{h,FM}} = 1.04476 + 0.22329\alpha + 7.14286\times10^{-3}\alpha^2 \tag{2.55}$$

$$D_{\mathrm{h,FM}} = 1.99345 + 0.30224\,\alpha - 0.11276\alpha^2 \tag{2.56}$$

Note that these results are valid for the free-molecular regime only. The scaling parameters are shown in Figure 2.11.

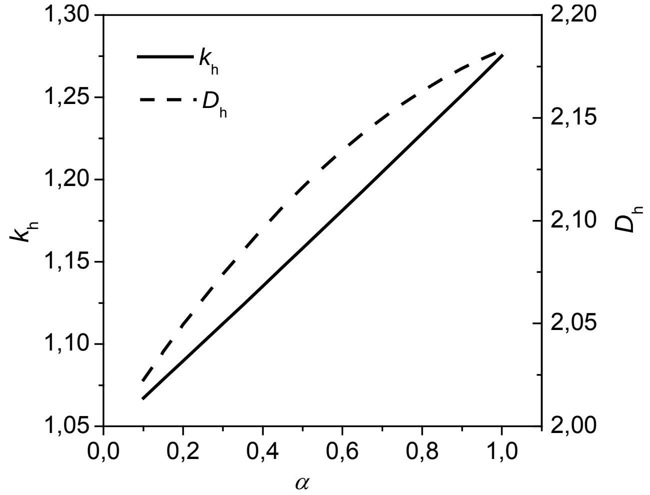

Figure 2.11. Scaling parameters D_h *and* k_h *in dependence on* α.

In the continuum regime, the scaling parameters for $D_f = 1.78$ and $k_f = 2.3$ are given by [99]

$$k_{h,C} = 1.32 \tag{2.57}$$

$$D_{h,C} = 2.07 \tag{2.58}$$

It should be noted that equation 2.54 is not valid for $N_p = 1$. In that case, D_{eff} is simply set to d_p.

In order to obtain the heat conduction for an aggregate, d_p is replaced by D_{eff} in the expression for the heat conduction. As the effective diameter is only given for either the free-molecular or the continuum regime, the expression of McCoy and Cha for heat conduction 2.23 can not be used in the transition regime in combination with the aggregate theory. However, Fuchs' model can be used in the transition regime including aggregates as it is a combination of the heat conduction of the free-molecular and the continuum regime. Heat conduction inside the boundary layer can then be expressed as

$$q_{\text{cond,Trans}} = \alpha\pi D_{\text{eff}}^2 \frac{p}{8}\sqrt{\frac{8RT_\delta}{\pi M_\text{g}}}\frac{\left(\gamma^*+1\right)}{\left(\gamma^*-1\right)}\left(\frac{T_\text{p}}{T_\delta}-1\right) \tag{2.59}$$

In Figure 2.12, the ratio of the heat conduction of an aggregate consisting of N_p primary particles to that of N_p isolated particles has been calculated as a function of the number of primary particles. The ratio is shown for a particle temperature of 3400 K with $T_g = 1700$ K, $d_p = 32$ nm and $\alpha = 0.3$. The Fuchs model has been used for the transition regime at a gas pressure of 20 bar, whereas 1 bar was chosen for the free-molecular regime.

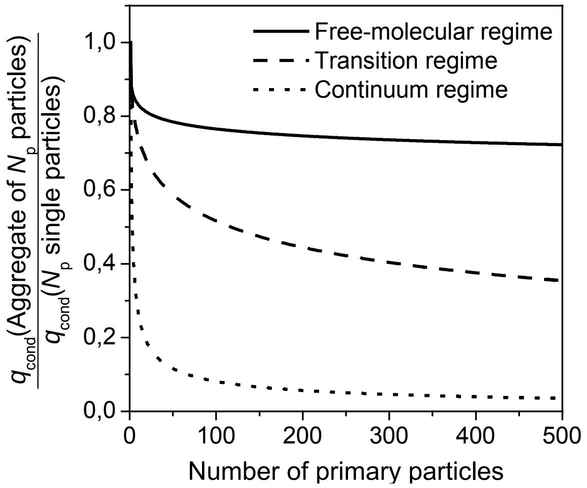

Figure 2.12. Ratio of the heat conduction of an aggregate consisting of N_p *primary particles to that of* N_p *isolated particles vs.* N_p *for different Knudsen conditions.*

The heat conduction for an aggregate rapidly decreases with increasing number of primary particles due to the shielding effect for all regimes. At a number of N_p = ~50 – 100 the ratio changes only slightly with increasing aggregate size. Aggregation effects the heat conduction more if the Knudsen condition shifts from the free-molecular regime towards the continuum regime: For N_p = 100, heat conduction is reduced by ~25% for an aggregate in the free-molecular regime, whereas it is reduced by ~50% in the transition regime for d_p = 32 nm and p_g = 20 bar, and by over 90% in the continuum regime. The pressure dependence of the ratio is shown in Figure 2.13 for two different aggregate sizes, calculated with the Fuchs model. An aggregate reduces the heat transfer with increasing pressure significantly. Hence, if LII is performed at elevated pressure, aggregation should be taken into account.

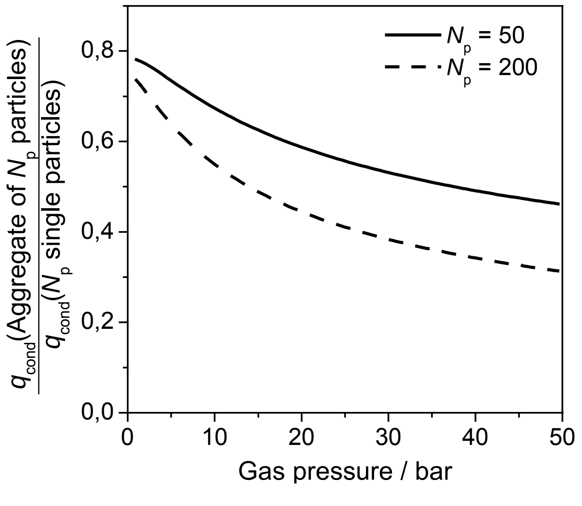

Figure 2.13. Ratio of the heat conduction of an aggregate consisting of N_p *primary particles to that of* N_p *isolated particles as a function of pressure.*

3 MODELING LII

Modeling LII is an import part in LII as the raw, experimental LII signal provides no quantitative information about particle sizes, particles size distributions or aggregation of the nano-sized particle ensembles. Not until the experimental data are compared to the modeled LII signal one does not retrieve the particle-size information. In this chapter, the software program LIISim, which has been developed in this thesis to model and fit LII signals, will be described. Model results will be shown to emphasize the influence of different sub-models in LII and to show the influence of different physical parameters. Furthermore, the ability of LII to determine particle-size distributions will be discussed.

3.1 LIISim – Program structure

In chapter 2.2, the underlying physics of modeling LII have been described and it has been shown that the resulting energy and mass balance is a first-order coupled differential equation. A first-order ordinary differential equation (ODE), written as

$$\frac{\mathrm{d}y}{\mathrm{d}x} = f(x)\,, \tag{3.1}$$

can be numerically solved with the Euler method

$$y_{n+1} = y_n + hf(x_n) \tag{3.2}$$

where h is the numerical integration stepsize. The derivative is used to obtain the solution at the point $x+h$. This is graphically illustrated in Figure 3.1a. However, the Euler method is neither very accurate nor very stable as compared to other integration methods. A wide-spread algorithm to numerically solve ODE's in practical applications is the Runge-Kutta algorithm. In its classical version, namely the *fourth*-order Runge-Kutta formula, the derivative is calculated four times per step h, and two intermediate points between y_n and y_{n+1} are used to determine the final value of the next step (see Figure 3.1b). In the classical version of Runge-Kutta, the stepsize h is kept constant. In this work, the stepsize has been determined by solving the ODE for different values of h. The integration variable is time, as the temporal behavior of the LII signal is modeled. The largest value of h, that gave the same result as smaller values, was found to be 0.2 ns.

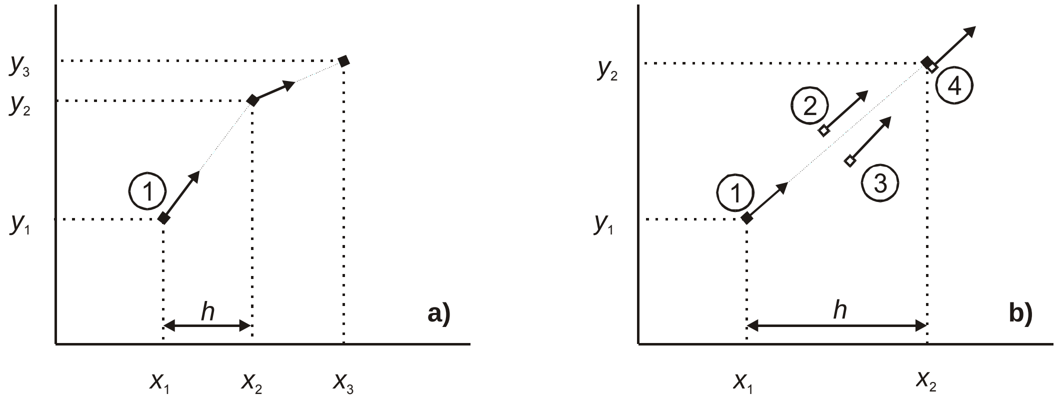

Figure 3.1. Euler's method (a) to solve an ODE (first order), and the fourth-order Runge-Kutta algorithm (b), that uses four evaluations of the derivative per step h, i.e. at the initial point (1), two intermediate points (2,3) and at a trial endpoint (4).

Modern versions of the Runge-Kutta method include adaptive stepsize algorithms that use small stepsizes when the function changes significantly, and larger stepsizes when the slope is rather flat. This can save computing time and some LII researchers apply such an adaptive stepsize algorithm [95,100]. More details on the Runge-Kutta algorithm are given in the book "*Numerical Recipes in C: The art of scientific computing*", chapter 16 [101].

In this work, a computer program, written in C, was developed to solve the ODE with the Runge-Kutta algorithm. The aim of this program, called LIISim, was to

- Model LII signals for different initial conditions, e.g. different particle sizes, gas temperatures, accommodation coefficients, etc.
- Model gated LII signals in dependence on certain parameters, e.g. fluence curves
- Enable the user to choose between different heat conduction sub-models
- Enable the user to choose between single particles, particles size distributions and/or aggregates
- Implement a fitting module to fit experimental signals with the model
- Set up a web interface to enable the use of the program by the scientific community world wide.

The advantage of using C as a programming language is, besides the flexibility and widespread use of C, the portability to different platforms, e.g. Microsoft Windows, Linux/Unix or Apple Macintosh. This is important for the use of LIISim on both a PC (mainly Microsoft Windows) and a web server with web interface (mainly Linux). The program is written in standard C and is compiled with the free available compiler lcc-win32 [102] (Windows) or gcc version 3.2 (Linux). The program is executed from the command line, e.g. in a DOS shell. All input parameters are given to the program in the form of ASCII files. This concept has been successfully used in LIFSim, which was developed by Bessler et al. at the Universität Heidelberg [103], and allows flexible input by either the user or another program, e.g. a web interface, without the need of recompiling the program. The output is given as an ASCII file as well, which is readily imported by other programs.

Different numerical functions are needed, e.g. the Runge-Kutta algorithm, a Levenberg-Marquardt non-linear least-squares fitting algorithm as well as several functions to solve algebraic equations numerically as it is required for the Fuchs model of heat conduction. They were taken from the book "*Numerical Recipes in C*" [101]. A detailed description of the different sub-modules and the structure of the source code of LIISim is given in the appendix.

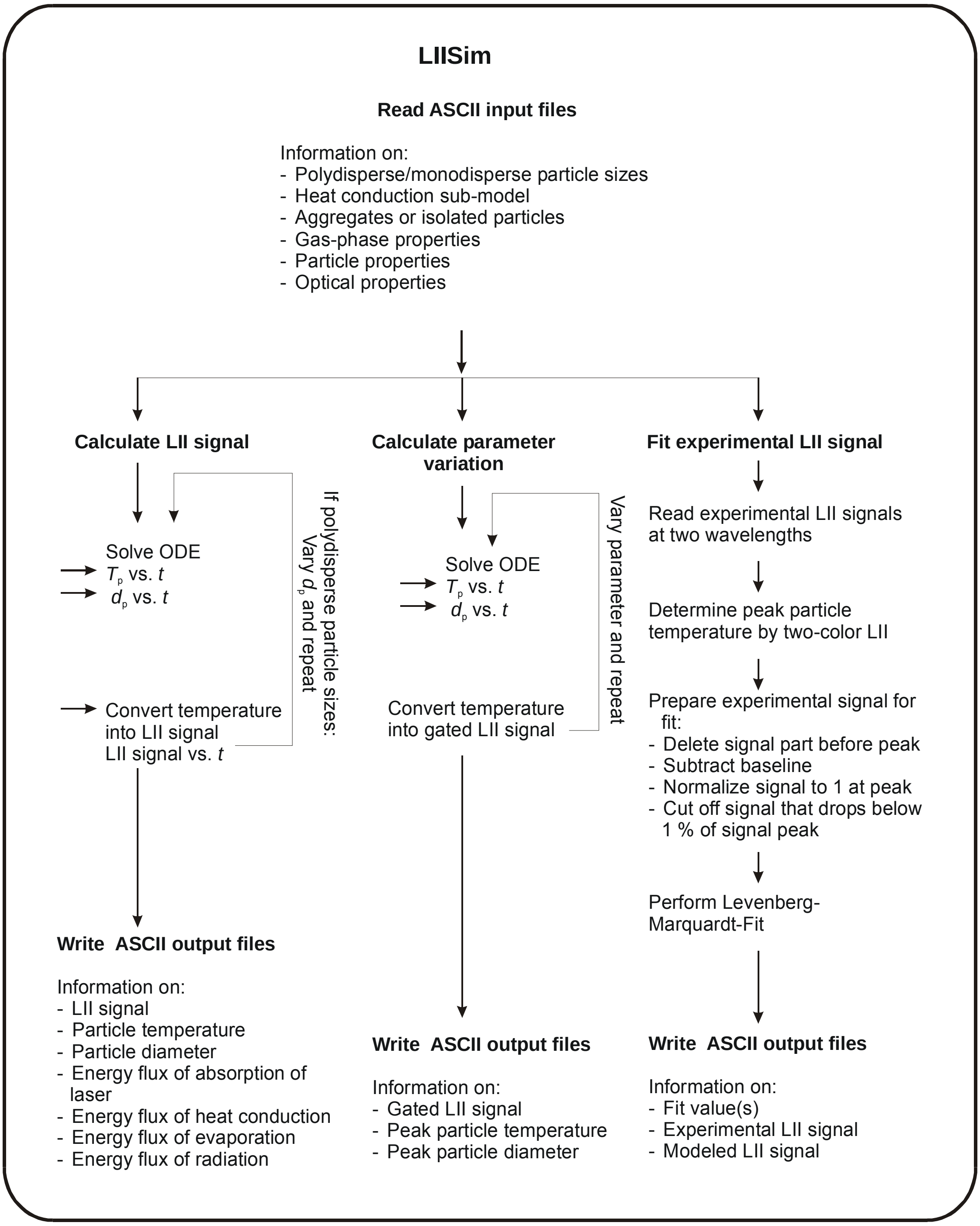

Figure 3.2. Schematic overview on LIISim.

A schematic overview on LIISim is given in Figure 3.2. It shows in a brief way the different tasks that can be carried out by the program:

Calculating LII signals. For given initial conditions, e.g. gas temperature, pressure, laser fluence, etc, the differential equation is solved and the LII signal is calculated as a function of time. This can be done for single isolated particles, log-normal particle-size distributions or aggregated particles. The result file contains the time histories of the LII signal, the particle temperature, the particle diameter as well as the contributions of the different energy fluxes, i.e. the absorption of laser energy, heat loss due to heat conduction, evaporation, and radiation. Different heat conduction models can be chosen.

Parameter variation. To obtain soot volume fractions, the LII signal is often temporally integrated ("gated"). This gated LII signal can be calculated by LIISim in dependence on a variable parameter like the laser fluence, the particle diameter or the pressure. In such a way, the influence of these parameters on the gated LII signal and, hence, the obtained soot volume fraction, can be modeled.

Fit experimental LII signals. Experimental LII signals can be fitted by a Levenberg-Marquardt non-linear least-squares fitting algorithm. The agreement between model and experiment is expressed by the maximum likelihood estimator χ^2:

$$\chi^2 \equiv \sum_{i=1}^{N_E} \left(\frac{y_i - y_i(x_i, a_1, \ldots, a_P)}{\sigma_i} \right)^2 \tag{3.3}$$

where y_i is the measured quantity, $y_\mathrm{i}(a_1,\ldots a_P)$ is the model prediction for P fitting parameters, N_E is the number of experimental data points, and σ_i is the experimental standard deviation. The Levenberg-Marquardt algorithm varies the fitting parameter(s) until a minimum for χ^2 is reached. This yields the set of fitting parameters that most likely represent the experimental conditions under the assumption that the applied model correctly describes the experimental method. The standard deviation can be either taken from the experimental input files or simply set to one. An individual data evaluation part allows to fit multiple LII signals successively. The data file names are passed to the program by an ASCII file. In such a way, long fit procedures for many signals can be run over night.

Up to 8 fitting parameters are possible in LIISim, though in practice a maximum of two variables are fitted while keeping the others constant. These fitting parameters are the gas temperature, the particle diameter or count median diameter, the thermal accommodation coefficient, the laser fluence, the temporal peak of the laser pulse, the number of primary particles per aggregate, the initial particle temperature, and the geometric width of the particle-size distribution. The user can choose the combination of fit parameters. A module for fitting the entire LII curve instead of the decay only is set up, but has not yet been used. It requires the experimental temporal laser profile in a high resolution. Using the entire LII curve requires to model the particle heating as well and might give a more robust fit. This could allow to fit more than two parameters.

In order to fit the model to an experimental LII signal, the peak particle temperature after laser heat-up is determined by two-color pyrometry. Only the signal decay curve is used for the fit since this part contains the information about the particle size. After the experimental signal is read by the program, the signal part before the peak is cut off. Then the baseline is substracted – a signal which results from the background luminosity of the sooting flame and does not contribute to the LII signal. The start of the LII decay curve is normalized to one, and the tail of the signal that falls below 1% of the peak intensity is cut off. This preprocessed signal is then passed on to the fitting module. The fit values, the experimental, and the modeled signal are written into the result file.

3.2 LIISim – Web interface

Different models for LII are widespread in the research community. However, recent comparisons have shown that large discrepancies exist between different approaches in the micro-physical mechanisms of particle heating and cooling [13]. From publications, however, it is difficult to compare the models presented by different research groups since

a) not all detailed equations and physical properties are always given in a paper

and

b) the finally programmed model is not available. Different models which use the same equations and physical properties might give different results due to different approaches in the numerical solution of the ODE or maybe even due to errors in programming the source code.

Therefore, the motivation was high to make LIISim available to the scientific community by a web interface. In a first step, only the modeling part of LIISim should be accessible via the web interface. The fitting routine requires a more detailed input to match individual experimental data sets, like the time resolution of the data and noise of the data, the use of two-color LII or single color LII. However, in future it should be feasible to implement the fit module in the web interface as well.

The web access of LIISim is accomplished by a CGI script (*Common Gateway Interface*). CGI-scripts are widely used on the internet to enable the communication between a user and programs, databases or other scripts via a web browser. HTML files can call the CGI script and pass data, entered in a form on a website by the user, to the script. The CGI script can process these data and then, in turn, generate new HTML code with the result which is sent back to the browser. With the use of CGI scripts, websites are no static surfaces, and, therefore, this phenomenon is often called “dynamic HTML”. Traditionally, perl is the programing language to write CGI scripts. The LIISim web interface is based on such a CGI script, written in perl.

A scheme of the functionality of the web interface is shown in Figure 3.3. The user sends the request to the server to model an LII signal. The perl script is called and an HTML form with the default values of the physical input parameters is sent to the user. This form contains information on the heat conduction model, particle aggregation, gas phase and particle properties as well as detection wavelengths. After the form is filled out and submitted, the data are read by the perl script and checked for wrong or incomplete entries. The form is sent back to the user in case of wrong entries, otherwise the ASCII input files are generated and the LIISim executable is called. The duration of the calculation depends on the computational speed of the web server – the program is not executed on the users computer. After LIISim has performed the calculation, the ASCII output file with the model results is passed to the program GNU-plot that creates a graph of the LII signal.

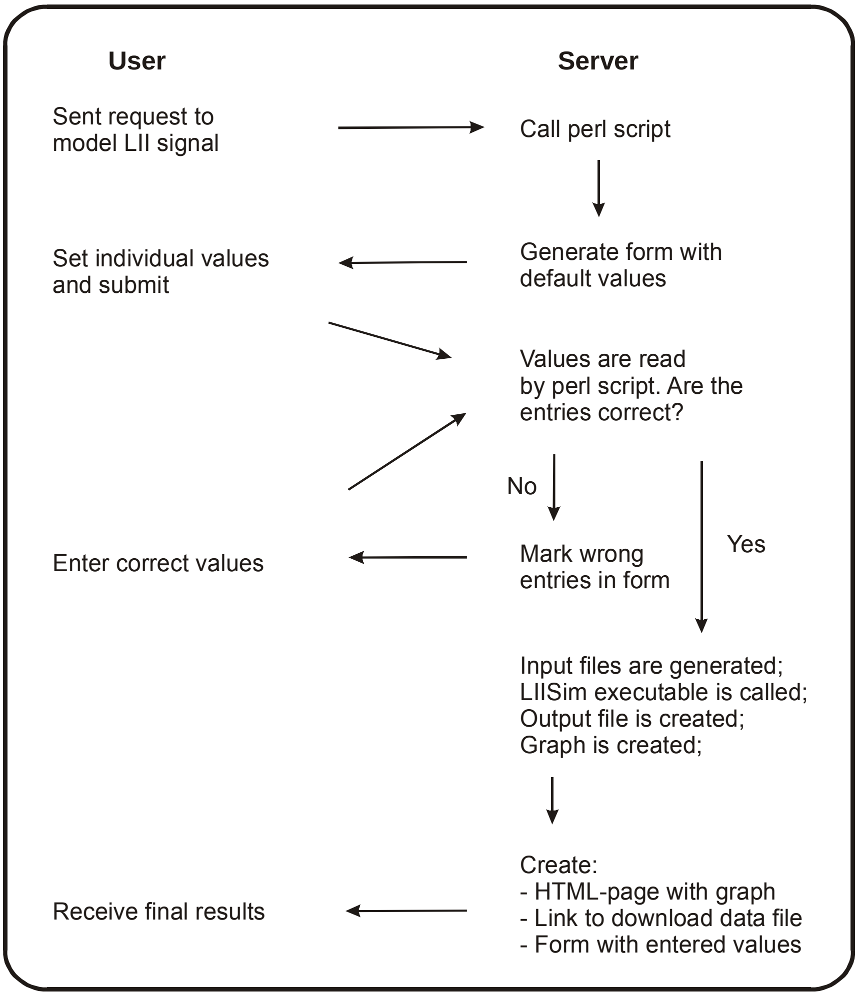

Figure 3.3. Functionality of the LIISim web interface.

A new HTML page is then created, which shows the modeled LII signal, a link to download the data file and the form with the corresponding initial conditions. The web surface of LIISim is shown in Figure 3.4. An individual domain was created for LIISim – it is available at http://www.liisim.com.

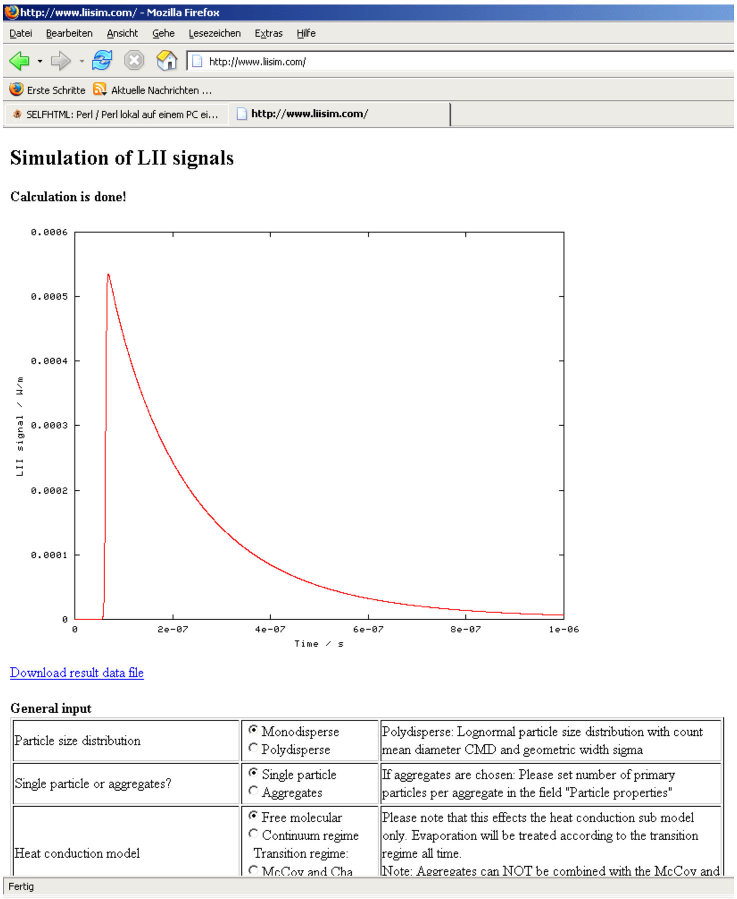

Simulation of LII signals

Calculation is done!

Download result data file

General input

Particle size distribution	● Monodisperse ○ Polydisperse	Polydisperse: Lognormal particle size distribution with count mean diameter CMD and geometric width sigma
Single particle or aggregates?	● Single particle ○ Aggregates	If aggregates are chosen: Please set number of primary particles per aggregate in the field "Particle properties"
Heat conduction model	● Free molecular ○ Continuum regime Transition regime: ○ McCoy and Cha	Please note that this effects the heat conduction sub model only. Evaporation will be treated according to the transition regime all time. Note: Aggregates can NOT be combined with the McCoy and

Figure 3.4. The LIISim website: http://www.liisim.com.

3.3 Comparing modeled LII signals

In this section, modeled LII signals will be presented for different conditions, i.e. different laser fluences, pressures, heat conduction models and particle properties. As the laser fluence has a significant impact on the LII signal, the cases for low and high laser fluences will be handled separately. This will reveal differences in the models and will show the influence of physical parameters, aggregates and particle-size distributions on the LII signal. Besides the temporal behavior of the LII signal, which is of importance for the derivation of particle sizes, the temporally integrated LII signal, as used for the measurement of soot volume fractions, will be modeled and discussed. Finally, the ability of LII to determine particle-size distributions will be described.

3.3.1 Low fluence

In the case of low laser fluences, i.e. the fluence is below the vaporization threshold, particle cooling will be dominated by heat conduction. Experiments have shown that this threshold is around 0.2 J/cm^2 [18,19,75] for 532 nm and that there is a negligible influence on the evaporation for fluences of 0.1 J/cm^2 at 1064 nm [71,104]. Of course this value strongly depends on the value of the soot absorption function *E(m)*. As a guideline, the peak particle temperature should remain well below the vaporization temperature of soot of 3915 K. In this study, a laser fluence of 0.1 J/cm^2 at 1064 was taken to model the low fluence LII signals.

Monodisperse particle sizes

In Figure 3.5, the particle temperature of a laser heated, monodisperse particle is shown for 1 and 30 bar. The particle diameter is 30 nm with a gas temperature of 1800 K. Compared are the different heat-conduction models which were described in section 2.2.5: The free-molecular regime (FM), the continuum regime, the heat conduction of McCoy and Cha and the Fuchs model. Additionally, the Fuchs model is shown with the often used simplified assumption for the change in internal energy which has been mentioned in section 2.2.4.

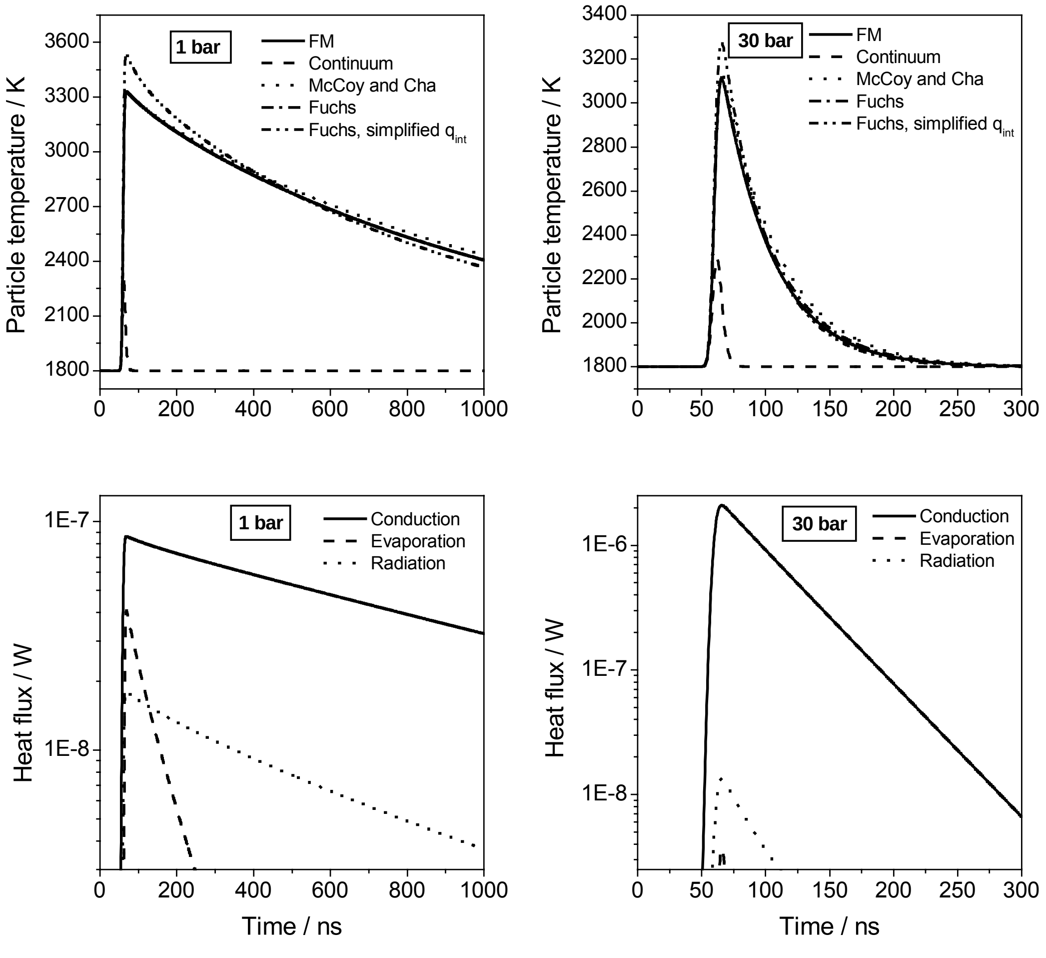

Figure 3.5. LII: Particle temperatures (top) and corresponding heat fluxes (bottom) for monodisperse particles of 30 nm diameter for 1 and 30 bar.

In the case of 1 bar, the Fuchs model and the free-molecular model behave almost identically. A peak temperature of ~3300 K is reached followed by a decay down to ~2400 K after 1000 ns. The model of McCoy and Cha results in a similar peak value but decreases slightly slower. Neglecting the temperature dependence of the particle mass and heat capacity in the change of the internal energy ("simplified assumption") results in a significantly higher peak value of ~3550 K and, hence, to a faster decay. The model for the continuum regime has been included for comparison only – the conditions at 1 bar are free-molecular (Knudsen number ~ 40) and the continuum model predicts – because of the very high heat-conduction rate – a low peak temperature of only 2300 K and a very quick temperature decay.

At 30 bar, the temperature decays much faster than at atmospheric pressure. The ambient gas temperature is reached again after ~250 ns behind the peak. With a Knudsen number of ~1.3 at these conditions, the free-molecular model and the Fuchs model are still very similar. The Fuchs model provides a smooth transition from the free-molecular case towards the continuum regime and should differ from the free-molecular case at high pressure, as the free-molecular model over-predicts heat transfer at high pressures. However, at typical high-pressure conditions of 30 bar and 1800 K, as it is the case in IC engines, the Knudsen conditions for a single, spherical soot particle are still close to free-molecular. The McCoy and Cha model decays, like in the 1 bar case, slightly slower than the free-molecular model. The use of the simplified expression for the change in internal energy results in too high peak temperatures like in the 1 bar case. Again, the continuum model is only shown for comparison. The differences between the different models at both 1 and 30 bar are not extremely large, but significant enough to cause differences if applied to evaluate particle sizes.

The energy fluxes for the different heat-loss mechanisms for 1 and 30 bar are shown in the bottom part of Figure 3.5, modeled using Fuchs' approach. At 1 bar, the dominant heat-loss mechanism is heat conduction, but radiation and even evaporation during the first 150 ns have a small contribution. At 30 bar, heat conduction is increased by more than one order of magnitude during the first 200 ns compared to 1 bar. The heat conduction rate in the free-molecular regime scales linearly with pressure (compare equation 2.16) and decreases the peak particle temperature from ~3300 K at 1 bar down to 3100 K at 30 bar. Radiation and evaporation are negligible in the case of low fluences at 30 bar.

So far, it can be seen that there are differences between some models in the case of monodisperse particles. The correct model can only be identified if experimentally by LII obtained particle sizes are compared with an independent method. This will be done in chapter 5.2.5.

Aggregation

As mentioned in section 2.2.10, aggregation does not affect the absorption, radiation or the change in internal energy (it only scales linearly with the number of primary particles per aggregate). Heat conduction, however, is influenced by aggregation, as it is decreased due to a shielding effect of particles inside the aggregate by surrounding particles. The effect of aggregation is shown in Figure 3.6. using Fuchs' model. The temperature history of a monodisperse 30 nm particle is shown for different aggregate sizes for 1 and 30 bar. There is a considerable influence of aggregation on the temperature decay of a laser-heated particle. Compared to an isolated particle, an aggregated particle cools down much slower. In the 1-bar case, the aggregation of 25 primary particles influences the temperature decay significantly, whereas further aggregation up to 200 primary particles has only minor consequences. At 30 bar, larger aggregates keep decreasing the temperature decay even up to 200 primary particles. First, this implies that, according to the model prediction, aggregation is an effect that should be considered in LII. Second, the differences between the atmospheric and the high pressure case show that the aggregate size at 1 bar needs not to be known exactly. Typical aggregates in flames can contain up to several hundreds of primary particles and, therefore, any large aggregate can be assumed to be present at atmospheric pressure. In the high-pressure case, however, there certainly is a difference between different aggregate sizes and, hence, this information must be available in order to evaluate the primary particle sizes quantitatively. It is difficult to determine a limiting pressure from which on the exact aggregate size must be considered – it is more a gradual shift towards higher pressure and depends on the individual situation, like gas temperature, primary particle size and peak particle temperature.

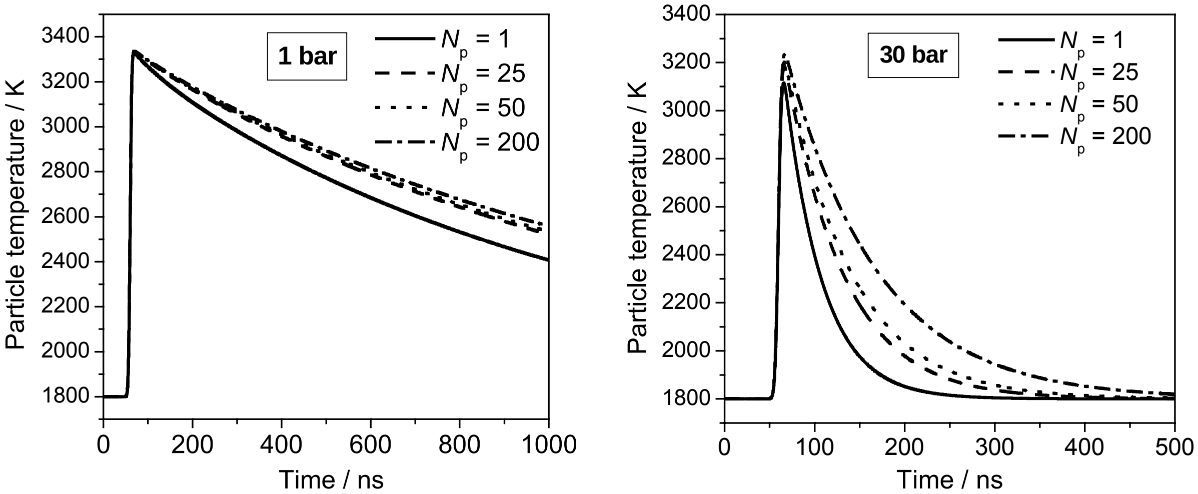

Figure 3.6. Particle temperatures of monodisperse particles (30 nm diameter) for different numbers of primary particles per aggregate for 1 bar (left) and 30 bar (right).

Polydisperse particle sizes

The particle-size distribution in many realistic combustion environments is not monodisperse. The particle sizes often follow a log-normal particle-size distribution which will result in an over-all LII signal from various different particle sizes in the probe volume. Laser-heated particles of different size will cool down at different rates and, therefore, no explicit particle temperature can be given for a polydisperse particle ensemble. Though some researches define an “effective temperature” [96], in this study, the LII signal is chosen in order to compare signals from polydisperse particle ensembles. The signal is detected at 550 nm and has been normalized in order to compare different conditions because only the relative decay of the LII signal is important for the evaluation of particle sizes. The effect of different geometric widths of a log-normal particle-size distribution is shown in Figure 3.7 for 1 and 30 bar. The Fuchs model has been used to model these signals. The LII signal decreases slower with increasing width of the distribution as the contribution of large particles increases and, hence, the signal is dominated by the slower cooling of larger particles. The LII signal decreases much faster in the high-pressure case, but the influence of different geometric widths is still significant. Therefore, polydisperse particles sizes should be considered in both atmospheric and high-pressure conditions.

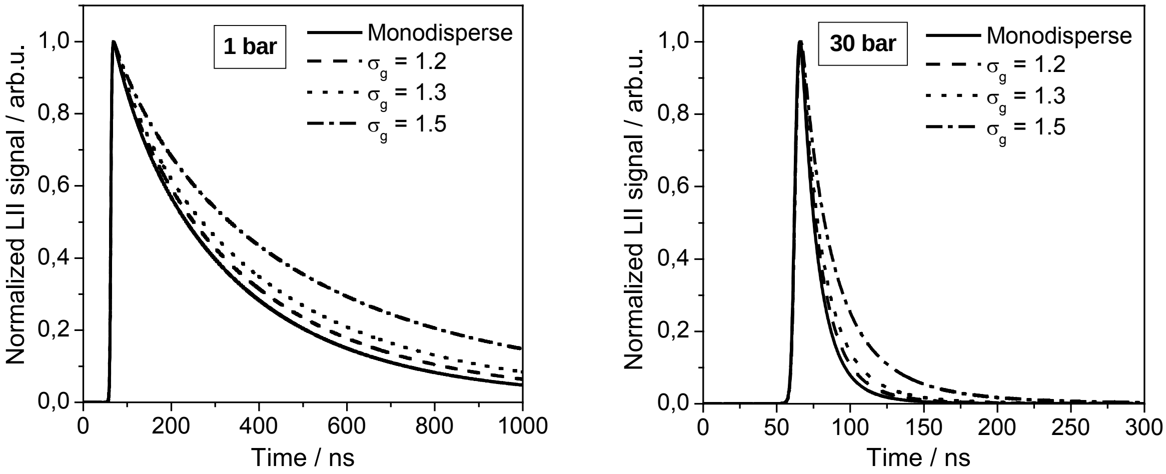

Figure 3.7. Normalized LII signals for polydisperse particles with a CMD = 30 nm for different geometric widths of the size distribution at 1 (left) and 30 bar (right).

3.3.2 High fluence

High laser fluences will cause vaporization of the particle. In contrast to the low fluence case, the particle size will change during the laser pulse. Again, Fuchs' model is used to show the effect of high fluences in modeling LII. A laser fluence of 1 J/cm^2 was chosen.

In Figure 3.8 the particle temperature, particle diameter and heat fluxes are shown for the high-fluence case at 1 and 30 bar. The peak temperature reached in the high-fluence case at 1 bar is ~4500 K which is far above the vaporization temperature of graphite of 3915 K. The particle temperature rapidly decreases during the first 50 ns after the peak due to a strong heat loss by vaporization. This is shown in the bottom left graph of Figure 3.8: Vaporization is the dominant heat-loss path during the first 50 ns after the peak. Then, heat conduction takes over and the temperature decreases less rapidly. The particle size is significantly reduced by vaporization and decreases from 30 nm down to ~20 nm which means a reduction of 30% in size.

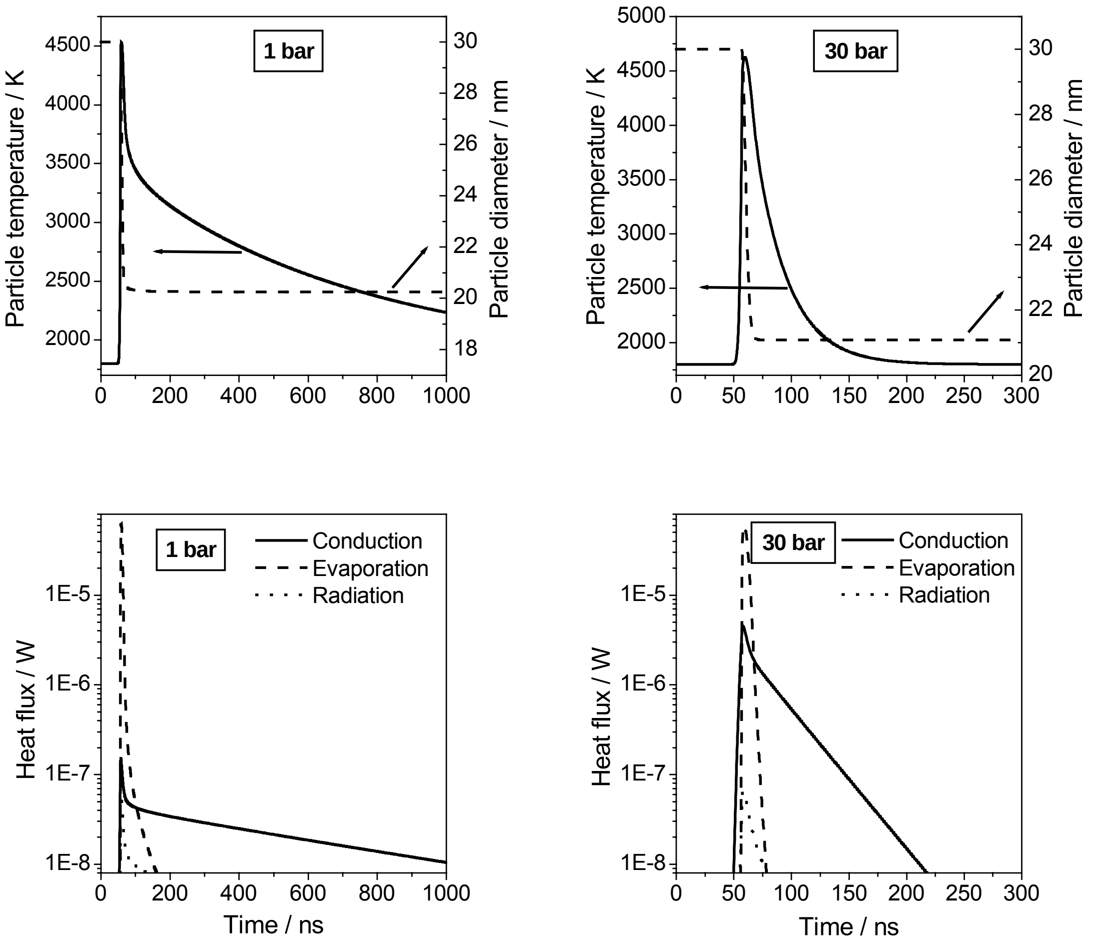

Figure 3.8. Particle temperature, diameter and heat fluxes for the high fluence case (1 J/cm^2 at 1064 nm). Left: 1 bar. Right: 30 bar.

For 30 bar, the peak temperature is slightly higher at ~ 4600 K because heat loss due to vaporization decreases with increasing pressure – in contrast to heat conduction. The diffusion coefficient of soot vapor decreases with increasing pressure and, hence, the flux of soot fragments escaping from the surface decreases at high pressure. The particle size is reduced a little less from 30 nm down to 21 nm. Vaporization is, like at 1 bar, the dominant heat-loss mechanism during the first 50 ns after the peak, though heat conduction has increased by more than one order of magnitude.

The fluence curve, i.e. the gated LII signal vs. laser fluence, and the corresponding peak particle temperatures are shown in Figure 3.9. For low laser fluences, the LII intensity rises monotonically with laser fluence as peak particle temperatures increase. Increasing laser fluence vaporizes the soot during the laser pulse and the maximum particle temperature remains nearly constant. In this regime, where maximum particle temperature is reached but only minor vaporization occurs, the variation of LII with laser fluence is small, resulting in a “plateau region” on the excitation curve. With higher fluences, the soot concentration is significantly reduced by vaporization resulting in reduced LII signals. This behavior is typical for a homogeneously distributed laser fluence.

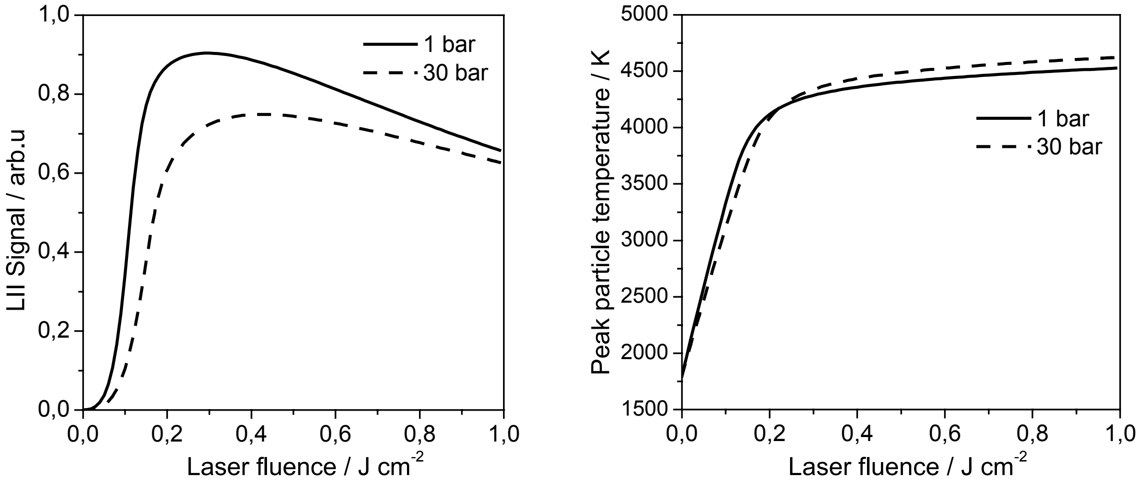

Figure 3.9. Fluence curve (left) and corresponding peak particle temperature (right) for 1 and 30 bar.

The peak particle temperature shown in Figure 3.9 is lower for 1 bar compared to 30 bar for fluences below 0.2 J/cm^2. Here, the increased heat conduction at high pressure decreases the peak particle temperature compared to 1 bar. Vaporization is the dominant heat-loss mechanism at high fluences. Since heat loss due to vaporization decreases at high pressure, the peak particle temperature at 30 bar is higher at fluences above 0.2 J/cm^2 than at 1 bar. This behavior will affect the determination of soot volume fractions with gated LII and will be discussed in the following section.

At 30 bar, the plateau region is shifted to slightly higher values compared to 1 bar. At 1 bar, this plateau is in the region of 0.25 – 0.3 J/cm^2 whereas at 30 bar it is around 0.4 J/cm^2. The decrease of vaporization and the increased heat conduction at high pressures forces the laser fluence to be higher to significantly vaporize the soot and, hence, get a reduced gated LII signal with increasing laser fluence. Up to date, this effect could not be observed experimentally. The only experimental fluence curve at elevated pressure has been reported at 15 bar [14], and it shows no shift of the plateau region towards higher laser fluences.

3.3.3 Soot volume fractions

The traditional application of LII was the two-dimensional measurement of soot volume fractions. Though the focus in fundamental LII research has gradually shifted towards the detection of primary particle sizes, the gated detection of LII for measuring soot volume fractions is still being used. The principle behind this technique is the assumption that the gated LII signal S_{LII} is proportional to the soot volume fraction. Melton [17] has derived an analytical expression which shows that this assumption is roughly fulfilled:

$$S_{\mathrm{LII}} = N_{\mathrm{d}} d_{\mathrm{p}}^{3+154nm/\lambda_{\mathrm{det}}} \tag{3.4}$$

Experiments have shown good proportionality of the gated LII signal to the soot volume fraction obtained by other methods, e.g. extinction. However, there are many cases where deviations of 10 – 40% from this linearity were reported [14,22,27,105]. Although LII models have been largely improved over the last two decades, no theoretical study on the linearity of gated LII versus the soot volume fraction has been repeated since the publication of Melton in 1984.

The model developed in this study has been used to analyze the potential of gated LII for the measurement of soot volume fractions at atmospheric and elevated pressure. The modeled LII signal has been temporally integrated over the first 50 ns, starting with the onset of the laser pulse. This detection gate is typically applied for measurements of soot volume fractions. Longer or delayed detection gates will bias the results towards larger soot volume fractions as small particles cool down faster than large ones. The laser fluence is, if not otherwise mentioned, set to 0.2 J/cm² – a typical value at the start of the plateau region. The gas-phase temperature was set to 1800 K and the detection wavelength was fixed at 550 nm.

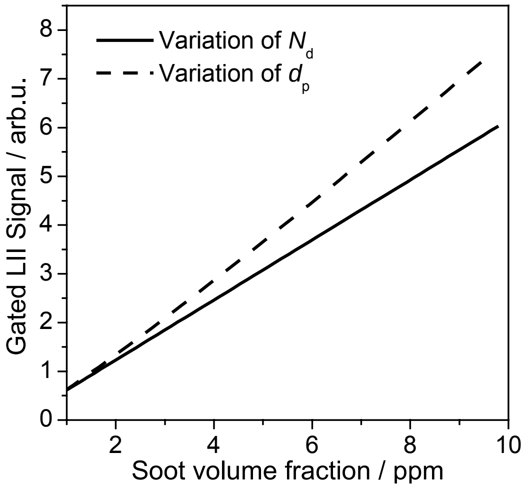

Figure 3.10. Dependence of the gated LII signal on the soot volume fraction.

In Figure 3.10, the gated LII signal is shown in dependence on the soot volume fraction. The soot volume fraction can be changed in two ways: Changing the particle diameter d_p or changing the particle number density N_d. The overall linearity between the gated LII signal and the soot volume fraction is excellent, although a small deviation can be seen if the particle diameter is varied. However, the obtained LII signal can differ significantly if a given soot volume fraction consists of a composition of different particle diameters and number densities. For instance, if the LII signal is calibrated at a soot volume fraction of 5 ppm for the conditions given in the solid line, i.e. a number density of $3.5 \cdot 10^{17}$ and a particle diameter of 30 nm, a wrong soot volume fraction of 4.2 (15% less) would be obtained if the conditions in the actual measurements volume were d_p = 52 nm and $N_d = 5.83 \cdot 10^{16}$ (dashed line). Additional error can be caused if the soot absorption function *E(m)* changes between different measurement conditions. Hence, more detailed experiments are necessary to determine the accuracy of the calibration of LII signals at one single, fixed flame condition.

A second issue on the linearity of gated LII with soot volume fractions is the pressure influence. This linearity is shown for different pressures in Figure 3.11a.

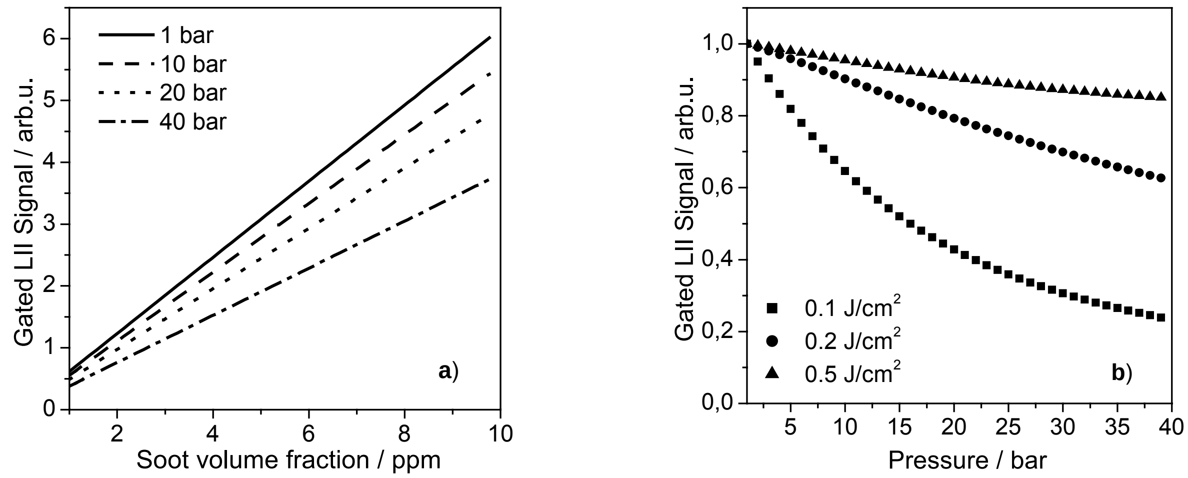

Figure 3.11. Gated LII signal for different pressures in dependence on the soot volume fraction (a) and for different laser fluences in dependence on pressure (b).

The number density has been varied to create different soot volume fractions. The slope of the gated LII signal vs. the soot volume fraction decreases with increasing pressure. This is shown in more detail in Figure 3.11b. The LII signal is plotted vs. pressure for 0.1, 0.2 and 0.5 J/cm^2. The signals are normalized at 1 bar. For the lowest fluence, the pressure dependence of the LII signal is most significant and the signal intensity decreases by nearly 80% from 1 to 40 bar. The effect is less significant if the fluence is higher: Absolute signal intensities decrease by ~40% and ~15% for 0.2 and 0.5 J/cm^2 respectively. Two effects are responsible for this behavior: The pressure-dependent peak particle temperature and the duration of detection gate.

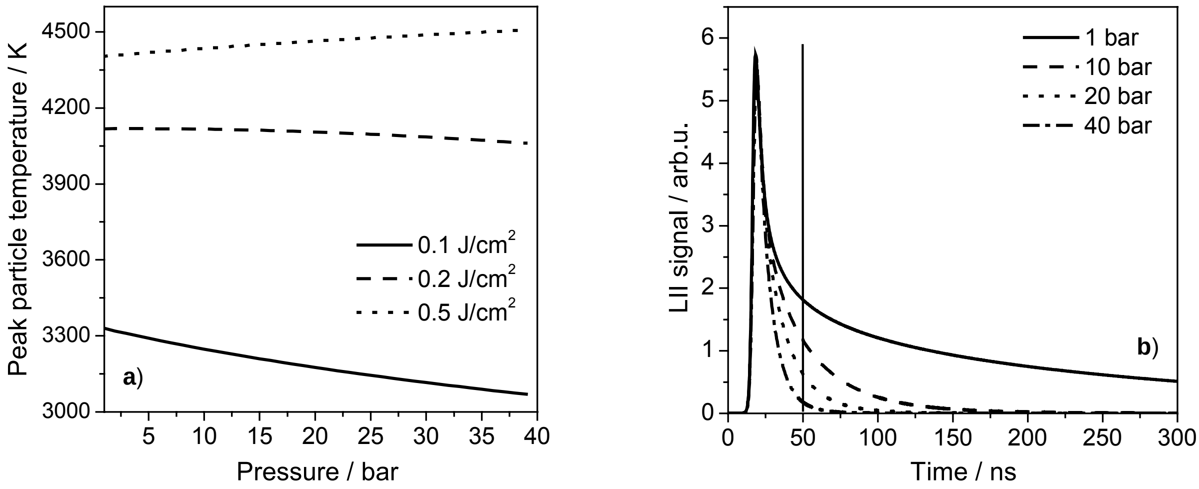

Figure 3.12. Peak temperature vs. pressure (a) and the detection gate (black line) for 0.2 J/cm^2 for different pressures (b).

The peak temperature vs. pressure is shown in Figure 3.12a. For 0.1 and 0.2 J/cm^2, the peak particle temperature decreases with increasing pressure. For instance, at 0.1 J/cm^2 the peak temperature decreases from ~3300 K down to 3060 K. This affects the decrease in absolute LII signal intensity significantly as it scales with T^5. For 0.5 J/cm^2, the peak particle temperature slightly increases with pressure which should result in an increased LII signal intensity at elevated pressure. However, the detection gate affects the absolute collected signal intensity as well. This is depicted in Figure 3.12b. The temporally resolved LII signals for different pressures at 0.2 J/cm^2 are shown. The detection gate of 0 – 50 ns is marked by the vertical black line. It can be seen that the enhanced signal-decay rate at high pressure results in less incandescence detected within this detection gate even though the soot volume fraction is the same for all cases. The prompt, “short” detection gate of 50 ns, which is generally recommended to avoid the influence of different decay rates from different particle sizes, is not sufficiently short for the very large differences in the decay rates at different pressures.

The consequence of these two effects is that if, for instance, calibration of the LII signal is performed in an atmospheric pressure flame, and this calibration is transferred to higher pressures, the soot volume fraction at high pressures will be underestimated. Modeling shows, that the error can be minimized if the laser fluence is high (~0.5 J/cm^2) and the detection gate is kept as short as possible, i.e. less than 25 ns. Correction for the pressure influence during data reduction of experimental signals may be difficult since the pressure influence strongly depends on the laser fluence. The laser fluence is often, due to absorption in strongly sooting (high-pressure) environments, not exactly known. Experiments should be performed to investigate this phenomenon more extensively.

3.3.4 Obtaining particle-size distributions with LII

If one wants to determine a log-normal particle-size distribution from an LII signal decay curve, two parameters must be fitted simultaneously: The count median diameter *CMD* and the geometric width σ_g of the distribution. In order to verify the uniqueness of such a fit, an LII decay curve with a *CMD* of 30 nm and a σ_g of 1.2 has been modeled using LIISim. The initial peak temperature was 3400 K and the gas-phase temperature was 1800 K. An ensemble of LII signals for different values of the *CMD* and σ_g was calculated, for each of which the maximum likelihood estimator χ^2 for the original signal was calculated. The result is shown for an atmospheric-pressure case and a high-pressure case of 30 bar in Figure 3.13. In both the atmospheric- and the high-pressure case, χ^2 reaches a defined minimum for the conditions of the original signal. It is surprising that for the 30 bar case a minimum is still obtained. For these calculations, only the first 75 ns of the LII signal were used. During this time, the signal has fallen below 1% of the initial peak value which is the cut-off criterion in LIISim for fitting experimental data. This short signal seems to contain still enough information for a fit procedure.

For the much slower decaying signal at 1 bar, the signal was used over a time period of 500 ns.

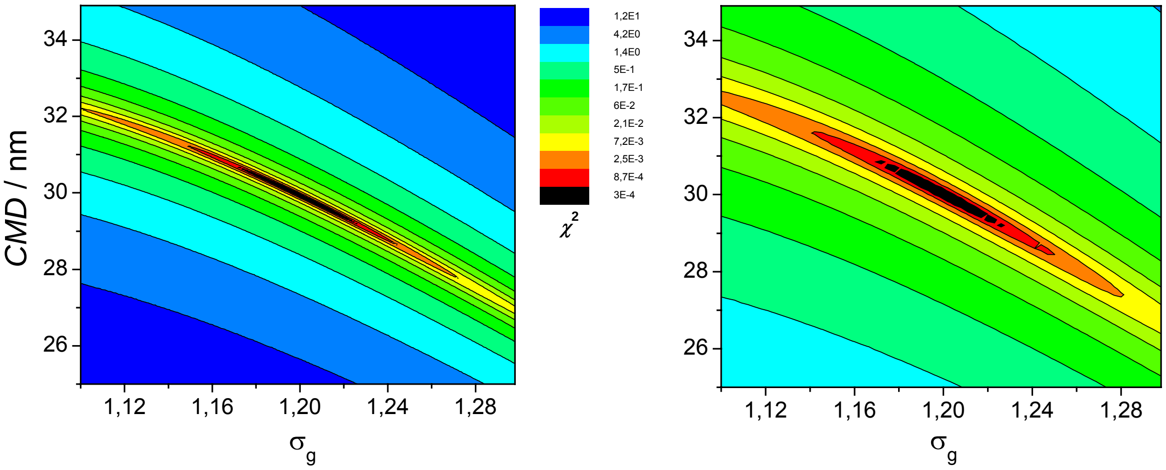

Figure 3.13. Maximum likelihood estimator χ^2 *for a given signal and different calculated signals as a function of CMD and* σ_g *for 1 bar (left) and 30 bar (right). Note the logarithmic scale of* χ^2.

It should be noted that the minimum is well defined, however, it lies in a long, rather flat “valley”. This indicates that for an experimental case, with noisy signals and certain errors in experimental input parameters like the gas-phase temperature, the fit might not be very robust. The information that is available from a monotonic signal decay is limited. This should be kept in mind when both parameters of the distribution are tried to be determined simultaneously.

4 EXPERIMENTAL

4.1 The high-pressure burner

In order to experimentally investigate the LII technique at elevated pressure, a burner was constructed that was laid out to stabilize laminar, sooting premixed ethylene/air flames at pressures up to 30 bar. The advantage of premixed flames over diffusion flames is the control of the stoichiometry of the premixed gases, i.e. a certain equivalence ratio of the premixed air and fuel can be set. Moreover, if a porous, homogenous fuel/air exit at constant temperature is used, the flame will be "flat", i.e. species concentrations and temperatures perpendicular to the direction of the flame propagation are constant. In this case, the axis in the direction of the flame propagation is directly correlated to a time axis of the flame chemistry. The fuel starts to decompose just above the burner surface and the reaction products are formed. In the case of sooting flames, the formation of soot precursors starts at low heights above the burner, then primary soot particles are formed, and aggregated soot particles are present at higher heights above the burner surface.

The construction of the burner was based on previous burners that had been build by the group of Prof. Dr. Dr. h.c. H. Gg. Wagner and Dr. H. Jander at the Universität Göttingen. They have extensively worked on soot diagnostics at elevated pressures for many years and have build several burners that provided premixed sooting flames at pressures up to 70 bar [89,106-110]. Some difficulties arise while working with premixed sooting flames at elevated pressure:

First, laminar, sooting high-pressure flames are very sensitive to turbulence and fluctuations in the gas flow. To stabilize the flame at elevated pressure, a suitable geometry of the burner housing is required to avoid strong convection and eddies that can perturb the flame. Additionally, a second, surrounding flame can stabilize the central flame. Moreover, this flame will prohibit a steep temperature gradient between the central sooting flame and cold, surrounding gases. The formation of a soot layer around the central flame is prevented with such a design.

Second, the diffusion of fuel and oxidizer perpendicular to the flame propagation decreases with increasing pressure. This will result in sooting “streaks” instead of a homogeneous soot distribution within the flame since the unburned gases that exit the channels of the flame holder do not mix with the surrounding gas of their neighbouring channels. To avoid these structures, the thickness of the “walls” between the individual channels must be small. This can be achieved by using thin metal foils (gold/silver/aluminum, ~10 – 50 µm thick) with a corrugated profile that are pressed together, resulting in a rectangular flame holder. For round flames, a similar package of capillary tubes, preferably silver due to the good heat conductivity, can be used. Alternatively, sintered metal foam provides a very fine and porous burner surface as well. However, typical stainless steel sinter matrices have a poor heat conductivity, and operation at high pressure with a high throughput of fuel requires good cooling. Additionally, it is of absolute priority for all constructions that the diameter of the channels in the flame holder is small enough to prevent a flashback of the premixed flame.

4.1.1 The burner and gas supply

The burner constructed in this work consists of a central burner with a diameter of 20 mm. In a first version of the burner, the central part consisted of a pack of ~4000 silver capillary tubes with 0.1 mm inner and 0.3 mm outer diameter and a length of 60 mm. The capillary tubes were pressed into a copper tube that is equipped with a cooling circuit. The silver capillaries, however, were blocked after some operation time of the burner, either due to the evaporation of small amounts of copper contained in the silver, or by soot falling down from the top of the burner housing. In a second version of the burner, the silver capillaries were replaced by a disc of sintered metal foam of stainless steel (Siperm® R10, 10 mm thick). This disc is more easily replaced than the silver capillaries. The central burner is surrounded by a second burner with a diameter of 56 mm that is made of a sintered bronze disc (Siperm® B40, 22 mm thick) in which a cooling coil of copper is embedded. The two burners are surrounded by a ring of sintered bronze (Siperm® B40, 5 mm thick) through which a co-flow of air is led to further stabilize the flame and to keep the windows clean of soot and water deposition. The burner assembly is shown in Figure 4.1.

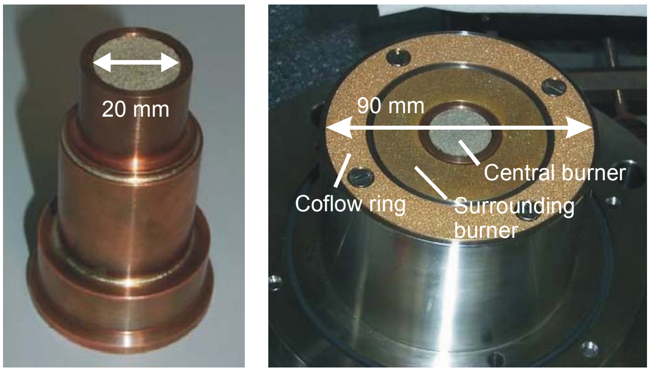

Figure 4.1. Central burner for the sooting flame (left) and the entire burner assembly consisting of the central burner, the surrounding burner and the co-flow ring.

The burner housing is made from a solid block of stainless steel with a bore of 90 mm. It is equipped with four quartz windows for optical access. Each window consists of an inner window of 43 mm diameter (2 mm thick) and an outer window of 60 mm diameter (20 mm thick). The inner window is flush with the combustion chamber to avoid any re-circulation of gases in the hutch of the flanges. The outer window holds the pressure and is sealed with a viton O-ring. Only viton O-rings are used in the entire burner, as this material withstands temperatures of up to 200°C. The window flanges are equipped with water cooling.

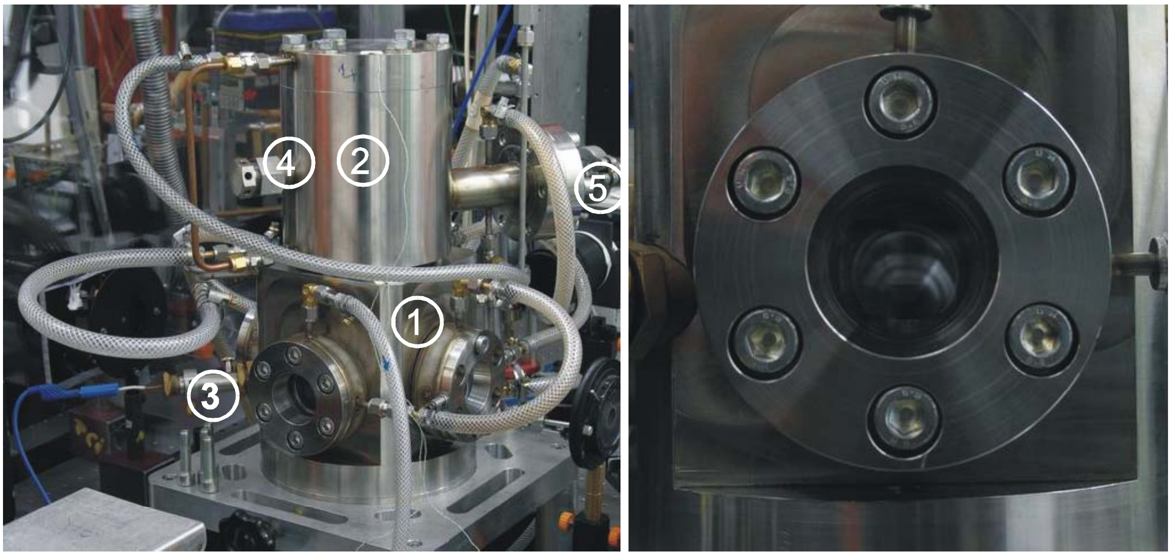

Figure 4.2. The high-pressure burner (left): 1) Burner housing 2) Heat exchanger 3) Ignition device 4) pressure relief valve 5) exhaust. One of four windows for optical access (right).

The burner is electrically ignited with a 0.5 mm thick platinum wire. The ignition device can be inserted into the burner so that the platinum wire is above the outer burner. Care has to be taken during ignition: If the combustion chamber is filled with a fuel/air mixture before an electric current is applied at the ignition device, a shock passes through the chamber which forces old soot to come off from the top of the burner housing. This soot can block the central burner which will result in a poor flame geometry. In such a case, the sinter matrix must be replaced. This can be avoided if the current is applied before the fuel enters the combustion chamber. The air flow is turned on at both burners and the co-flow ring. A current of ~13.5 amperes is applied and the fuel of the outer burner is turned on. As soon as the fuel enters the combustion chamber a smooth ignition of the flame follows. The electric current is then turned off and the ignition device is pulled back into the wall of the burner housing. Then, the fuel for the central burner is turned on and the inner flame is ignited by the outer flame.

A funnel with several concentric rings is placed at a height of ~30 mm above the burner surface to stabilize the flame and to ensure a laminar flow of the exhaust gases. The funnel and rings are made of Thermax® stainless steel which can withstand high temperatures up to 1320 K in oxidizing atmospheres. After passing the stabilization rings, the hot flame gases are led through a heat exchanger which is placed on top of the burner housing. A pressure relief valve is mounted at the side of the heat exchanger to ensure blow off in case of an unwanted pressure increase. It consists of a nickel membrane that is machined to break at a pressure of 43 bar at 200°C. A picture of the burner is shown in Figure 4.2.

The entire burner is placed on a three-dimensional translation system. This provides the ability to probe the flame in all dimensions without the need of changing the alignment of the laser and the detection system. The translation system can be controlled via the serial port of a PC. This enables the automated scan of the flame while taking data at different locations in the flame.

Ethylene 3.0 and methane 2.5 were taken from gas cylinders (Air Liquide) and used as fuel for the central and the surrounding flame respectively. High-pressure air was provided by a compressor (Bauer Kompressoren, Type Verticus 5, model I 150-11-5) at 340 bar which was reduced to a pressure of 35 bar. The gas flows were controlled with high-pressure mass-flow controllers (Bronkhorst). A maximum pressure difference of 20 bar between in- and outlet had to be maintained. Usually, a Δp of 5 – 10 bar was used during operation. Fuel and air were mixed in mixing chambers behind the flow controllers after which the gases entered the burner. For the gas supply of the central burner, however, an additional buffer volume was necessary to prevent fluctuations of the gas flow. An oscillation in the intensity of the sooting flame with a frequency of 0.1 Hz was observed without a buffer volume. The buffer volume used was ~1000 cm^3 and provided a stable flame. Nitrogen monoxide (NO) could be seeded to the fresh gases of the central burner. This was required for multi-line NO-LIF thermometry experiments in order to obtain the gas-phase temperature of the flame. The NO was taken from a gas cylinder (Air Liquide). The connections for the gas supply, including the connections for water cooling, are shown in Figure 4.3.

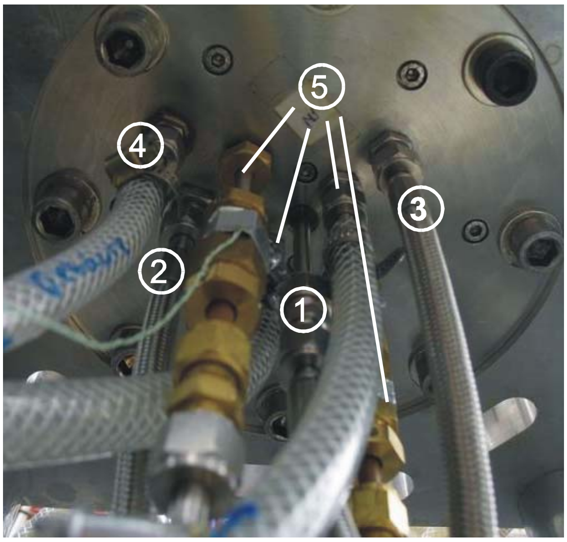

Figure 4.3. Bottom view of the burner with gas and water connections: 1) Gas central burner 2) Gas surrounding burner 3) Co-flow 4) Inlet cooling burner housing 5) Cooling burner matrices.

The exhaust gases were fed into two filter vessels that contain stainless steel chips and steel wool in order to separate the soot from the exhaust gases. The vessels reached ~80 – 90°C at 1 – 2 bar and were kept above the dew point of the exhaust gases at higher pressures. After the filter vessels, the gases passed a motor-driven valve that is used to control the ambient pressure. The gases were expanded to atmospheric pressure, cooled down to room temperature to condensate the water, and were finally led into the exhaust gas system of the laboratory. A schematic layout of the gas supply and exhaust system is shown in Figure 4.4.

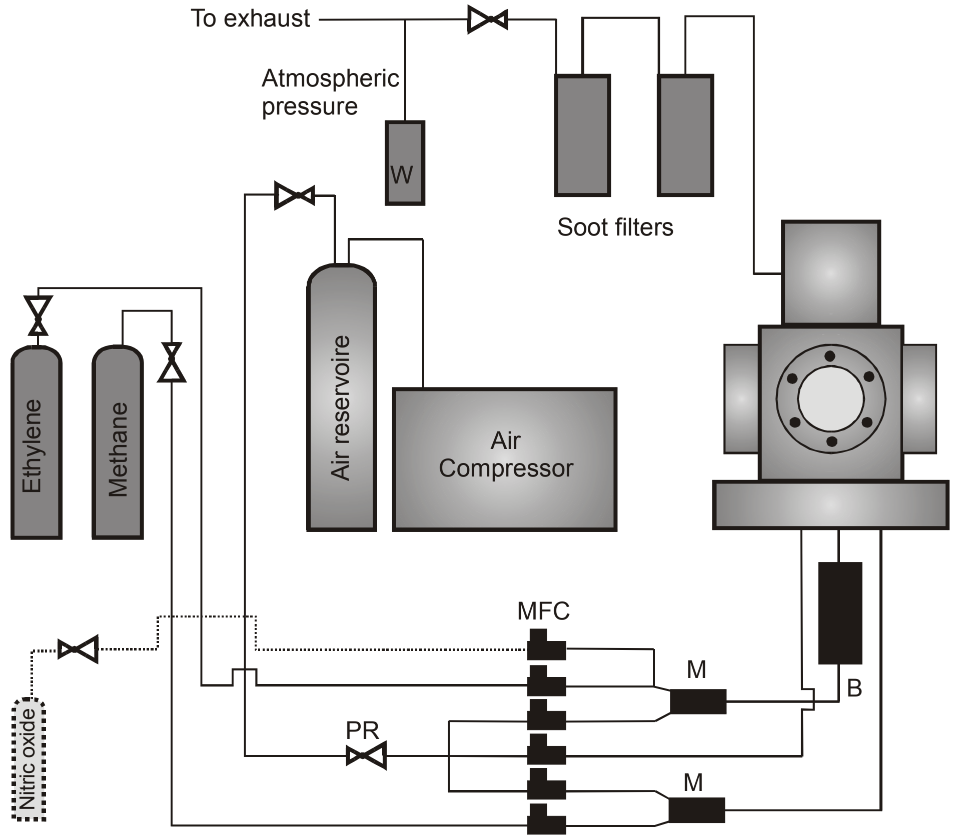

Figure 4.4. Gas supply and exhaust system of the high-pressure burner. M = Mixing chamber, W = Water condenser, MFC = Mass flow controller, PR = Pressure reducer, B = Buffer volume.

4.1.2 The cooling circuit

As the high-pressure burner is set up for premixed flames, the flow rates scale roughly linearly with pressure. The amount of heat produced by the burner can be estimated by calculating the reaction enthalpy of the combustion of methane and ethylene at the given flow rates for a typical flame at a certain pressure. This was done for an equivalence ratio of $\phi = 1$ using the reaction enthalpies of

$$CH_4 + 2\ O_2 \rightarrow CO_2 + 2\ H_2O\ ,\ \Delta H^0 = -890\ \text{kJ/mol} \quad (4.1)$$

$$C_2H_4 + 3\ O_2 \rightarrow 2\ CO_2 + 2\ H_2O\ ,\ \Delta H^0 = -890\ \text{kJ/mol} \quad (4.2)$$

The reaction enthalpies of the real reaction in the unstoichiometric case will be slightly different. However, the reaction enthalpies of the stoichiometric case will be close to the real enthalpies and can be used to estimate the emitted power of the high-pressure burner for the different operating pressures. The thermal power versus pressure is shown in Figure 4.5 for a typical speed of the fresh gases of 6 cm/s. The power developed increases with pressure up to 19 kW at 30 bar. Hence, a good cooling system is required.

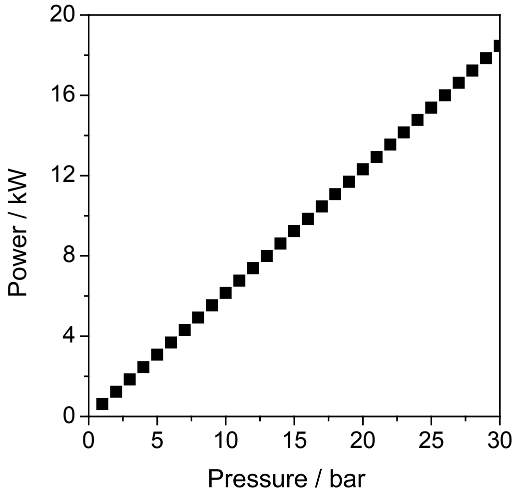

Figure 4.5. Thermal power of the high-pressure burner vs. operating pressure.

The burner has four different cooling circuits. The central burner and the surrounding burner are linked together and are kept at 60°C for pressures up to 5 bar and at 45°C for higher pressures. Water from a thermostat (Lauda UB20) was used as flow medium. The burner housing and window flanges were cooled with water to keep the temperature at ~70°C. The top part of the burner was cooled with water as well and the temperature was kept at ~70°C. The temperature of the exhaust gas had to be above 100°C to avoid condensation of water. Therefore, no cooling was applied at pressures less than 5 bar. At pressures of 5 bar and above, the exhaust tube between burner and soot filter was purged with a constant flow of air. Although the exhaust tube is made of flexible, stainless steel, temperatures can reach 250°C and more if no cooling is applied at high pressures. The maximum temperature limit of the flexible exhaust tube is 250°C as specified by the manufacturer (Serto Jacob). The temperature at the burner is observed by several thermocouples.

4.1.3 Burner operation

The design of the burner was laid out for a maximum operating pressure of 30 bar. However, due to the change from silver capillary tubes to a stainless steel sinter matrix in the central burner, heat conduction from the burner surface to the water cooling was significantly reduced. The reaction zone of the flame moves closer towards the burner surface with increasing pressure and the temperature of the burner surface increases. If the temperature becomes too high, the burner sinter matrix will be blocked and leakages will appear between the edge of the sinter matrix and its mount. Therefore, the burner was operated at pressures up to 10 bar. An example of the non-sooting flame at 1 bar is shown in Figure 4.6.

Figure 4.6 Non-sooting flame at 1 bar for $\phi = 1$ with a fresh gas velocity of 10 cm/s.

Both the ethylene/air and the methane/air flame show the blue chemo luminescence of the CH radical. The red part on top is the incandescence of the hot flame-stabilization rings. If the equivalence ratio of the central burner is increased, soot formation begins, indicated by the yellow luminescence of the flame. Typical sooting flames for 1, 2, 5 and 10 bar are shown in Figure 4.7.

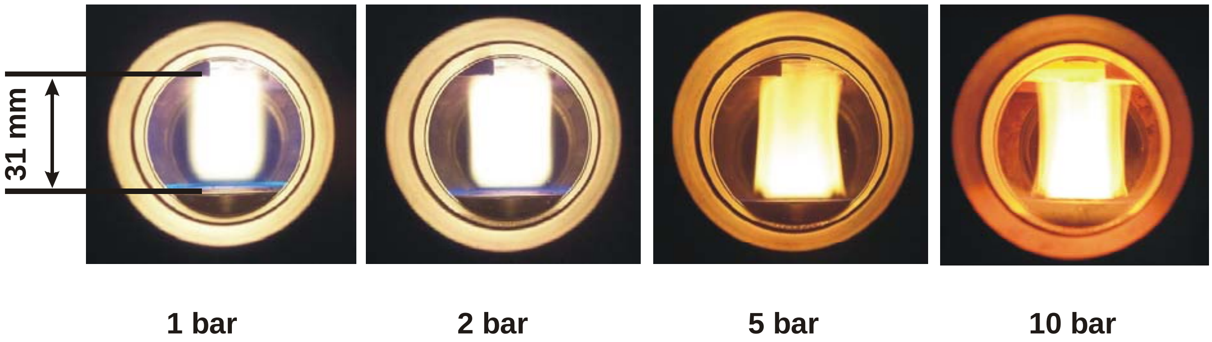

Figure 4.7. The flame of the burner at different pressures.

The flame has a height of ~30 mm and a diameter of ~20 mm. It can be seen that the flame is lifted at 1 bar and that there are a few millimeters space between the burner surface and the onset of soot formation. In this region, the fuel breaks down and the reaction products and soot precursors are being formed. With increasing pressure, this reaction zone becomes thinner as the density increases with increasing pressure. The onset of soot formation moves closer to the burner surface.

Pressure [bar]	Φ	v_{fg} [cm/s]	Air flow [l_n/min]	Ethylene flow [l_n /min]
1	2.1	8	1.31	0.19
2	2.1	8	2.63	0.39
5	1.95	8	6.63	0.90
10	1.95	6	9.95	1.35

Table 4.1. Equivalence ratio, fresh gas velocity and gas flows of the central burner for 1 – 10 bar.

The corresponding gas flows of the flames are listed in Table 4.1 and Table 4.2.

Pressure bar	Φ	v_{fg} **[cm/s]**	**Air flow [l_{n} /min]**	**Methane flow [l_{n} /min]**	**Co-flow Air [l_{n} /min]**
1	1.4	10	10.1	1.48	10.7
2	1.2	10	20.6	2.59	10.7
5	1.2	6	30.9	3.89	10.7
10	1.2	6	61.7	7.78	10.7

Table 4.2. Equivalence ratio, fresh gas velocity and gas flows of the surrounding burner and the co-flow for 1 – 10 bar.

Because the fresh gases for the high-pressure burner are premixed, the equivalence ratio can be chosen. However, there are certain limitations for the gas flows because a stable, homogeneous flame must be the result. If the fresh-gas velocity is too low, the flame is unstable. If the fresh-gas velocity is set too high, the diffusion of fuel and air perpendicular to the flame propagation is decreased and the flame shows, especially at high pressure, sooting streaks instead of a homogeneous soot distribution. Typical velocities of the cold fresh gas are in the order of 6 – 10 cm/s. The equivalence ratio of the surrounding burner must be $\phi > 1.0$ to avoid oxidation of soot at the edge of the central flame. When the pressure in the chamber is changed, the central flame is always set to a non-sooting flame. The gas flow of fuel and air of both the central and the surrounding burner are equally increased. The control unit of the flow controllers (Bronkhorst) allows to define one flow controller as master and the others as slave with individual scaling factors. In such a way, the setting of only one flow controller must be modified, and changing the gas flows is much simplified. The gas flows are kept higher than the actual pressure requires until the flows for the desired pressure are reached. The final chamber pressure is then controlled by adjusting the motor-driven needle valve at the exhaust exit. About 1 – 2 minutes were taken to allow the system to stabilize and get into thermal equilibrium. The burner shows a long-term stability (> 30 minutes) at a given pressure. The pressure fluctuation is less than ± 2%.

Great care must be taken when machining the burner head and the sinter matrices. Due to the exposure to high temperatures, no O-rings are used for sealing. Instead, the different parts are machined with an accuracy in the order of 0.01 mm. If there are gaps between the central and the surrounding burner, the flame will be significantly disturbed. This is shown in Figure 4.8. There is a leak at the left side of the flame. The flame is then blown to the right side – an effect that increases with increasing pressure. The leak can be seen in the left side of the picture at 5 bar where the blue flame of the surrounding burner is not flat but shows a small bump. Such a flame can not be used for measurements.

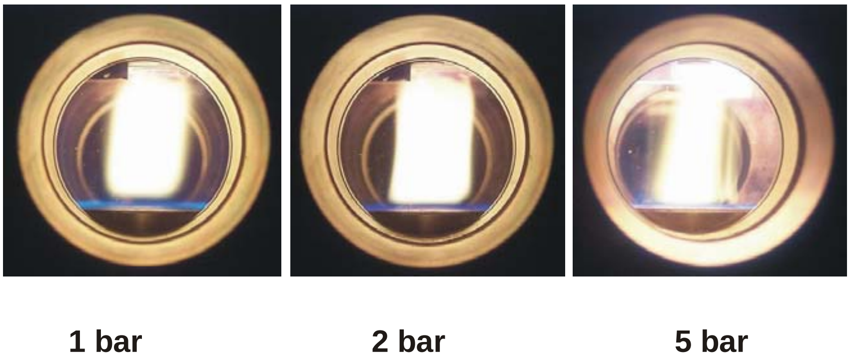

Figure 4.8. Tilted flames at 1, 2 and 5 bar in case of incorrect sealing between central and surrounding burner.

Safety is important when working with high-pressure flames. The gas supply of both fuels, ethylene and methane, can be shut off manually by hitting an emergency button which will close two valves in the tubes of the gas supply. The burner is encased in transparent Makrolon® bullet-proof windows of 20 mm thickness. Windows and burner were mounted in the gap of a U-shaped optical table to provide a working area for the optical diagnostics. They will be described in the following section.

4.2 LII Experimental

4.2.4 Excitation: Laser system

Soot is a broad-band absorber and, although the absorption cross-section increases with decreasing wavelength, in principle any wavelength in the visible or IR regions can be used to heat the particles for LII detection. Ultraviolet excitation wavelengths of 266 and 355 nm were used to generate LII [111], but shorter UV wavelengths preferentially promote photodissociation instead of particle heating [112]. Nd:YAG lasers are frequently used for LII excitation because these lasers are generally reliable, and provide high-power pulses with typical pulse durations of 8 – 15 ns. The fundamental (1064 nm) or second harmonic (532 nm) are most often used for LII.

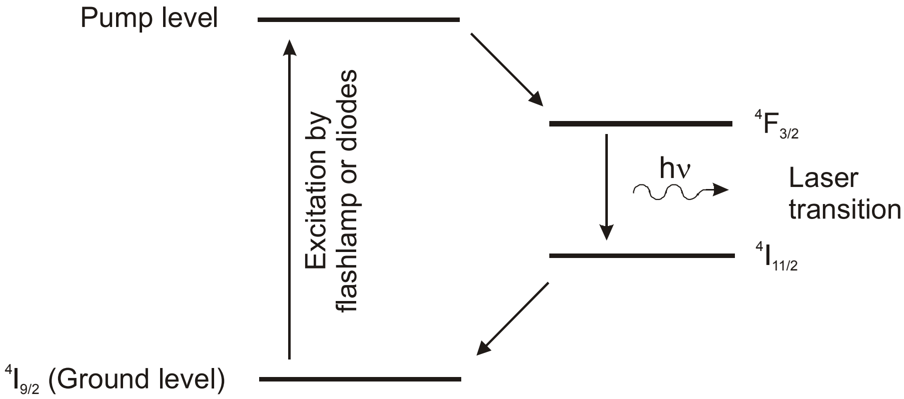

Figure 4.9. Four-level scheme of Nd^{3+} in $Y_3Al_5O_{12}$.

The active medium of a Nd:YAG laser consists of a YAG crystal (yttrium-aluminum-garnet, $Y_3Al_5O_{12}$) in which ~1% of the Y^{3+}-ions are replaced by Nd^{3+}-ions. They are responsible for the laser transition. The Nd:YAG laser is a four-level laser (Figure 4.9).

The ground level is the $^4I_{9/2}$-level from which the pump radiation is absorbed and the Nd^{3+} is excited into the pump levels. The most important ones are the [$^4F_{5/2}$, $^2H_{9/2}$]-levels (pump wavelength of 0.8 μm) and the [$^4S_{3/2}$, $^4F_{7/2}$]-levels (pump wavelength of 0.7 μm). A fast transition without radiation takes place to the $^4F_{3/2}$-level which has a long lifetime of 240 μs. In this way, the population inversion between the upper $^4F_{3/2}$-level and the lower $^4I_{11/2}$-level is generated.

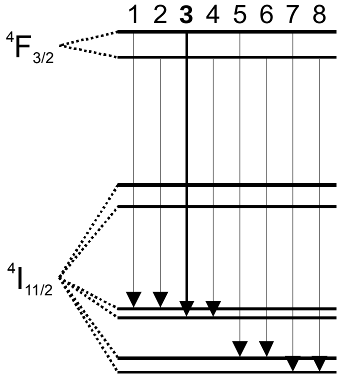

Figure 4.10. Laser transitions of Nd^{3+} in YAG

The laser transitions are shown in detail in Figure 4.10 [113]. The dominating transition with the strongest intensity is the transition 3, i.e. the upper level of $^4F_{3/2}$. It is re-filled by the lower $^4F_{3/2}$-level according to the Boltzmann distribution with a ratio of 40:60. The lower laser level is quickly depopulated by a radiationless transition into the ground level.

For high power in pulsed operation, a so-called quality switch (Q-switch) is used. This is an optical switch that changes the quality of the resonator (i.e., “close” or “open” the cavity). For maximum output, the timing of the Q-switch must be optimized. If the switch is opened too early, the maximum population inversion has not been reached. If it is opened too late, the upper laser level has started to depopulate due to thermal relaxation. High peak power of more than 20 MW and pulse duration of less than 10 ns can be reached in this operating mode.

4.2.5 Detection

The LII signal was detected both spectrally and temporally resolved. The spectrally resolved detection was accomplished with an imaging spectrometer (Acton Research Corp., Model 150, grating with 100 grooves/mm, blazed for 450 nm) combined with an intensified CCD camera (ICCD) (FlameStar II, LaVision, 576 x 384 pixel, 12 bit). The intensifier was gated for the first 40 ns of the LII signal. The obtained images have one spatial axis and one wavelength axis. The spatial axis is the axis in the direction of the laser beam, i.e. the LII signal was detected as a horizontal profile through the flame. The wavelength range covered reached from 656 to 400 nm. The combination of spectrometer and ICCD was calibrated for spectral sensitivity with a tungsten filament lamp (Spectra Physics Oriel, SN 7~1545). Calibration for absolute wavelength position was performed with a mercury lamp (LOT 6035). The spectrometer set-up was used to detect the flame soot emission as well.

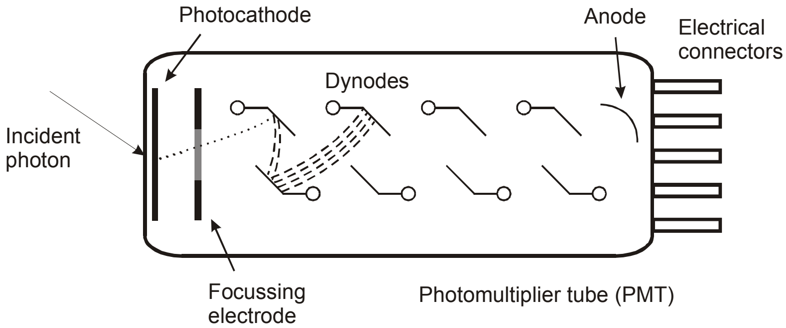

Figure 4.11. Schematic of a photomultiplier tube (PMT).

The time-resolved LII signal was detected with fast photomultipliers (Hamamatsu R7400U-04). A schematic of a photomultiplier tube is shown in Figure 4.11. The incident photons hit the photocathode which is coated with a light-sensitive material. Here, electrons are released due to the photoelectric effect. These electrons are directed towards the electron multiplier by a focussing electrode. The electron multiplying is performed by a series of so-called dynodes. Each dynode is held at a higher positive potential than the previous one. The first electron, resulting from the incident photon, is accelerated towards the first dynode, releasing more electrons to escape from that dynode. They are accelerated towards the next dynode where, in turn, again more electrons are released. In this cascade, the electrons are being multiplied at each stage until they reach the anode where a sharp current pulse indicates the arrival of a photon at the photocathode.

The signal was detected at two wavelengths: 550 and 694 nm. The width of the detection filters are 694 ± 12 and 550 ± 10 nm FWHM respectively. The rise time of the photomultipliers is ~400 ps, the time-response of the combination of the photomultiplier with integrated high-voltage supply (Seefelder Messtechnik) is 780 ps. The highest sensitivity of the photomultipliers is at 400 nm, see also [114]. The set-up is shown in Figure 4.12. The spectral sensitivity of the two-color set-up is calibrated with the same lamp as used for the calibration of the spectrometer.

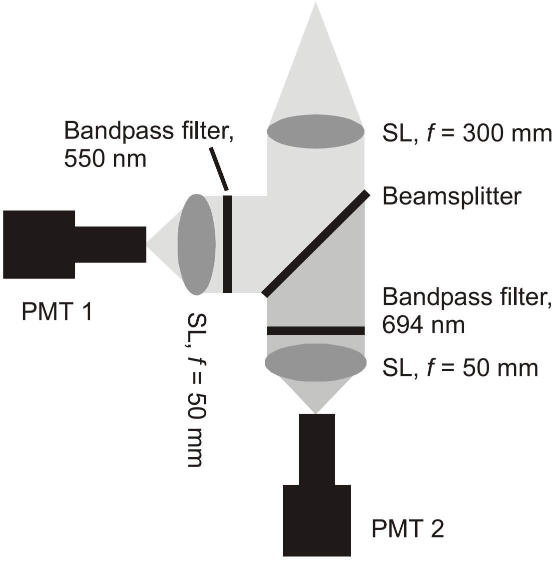

Figure 4.12. Set-up for two-color LII detection. PMT = photomultiplier tube, SL = spherical lens.

4.2.6 Experimental set-up

LII was performed in the high-pressure burner in premixed ethylene/air flames at pressure of 1 – 10 bar. The fundamental wavelength at 1064 nm of a Nd:YAG laser (Continuum PowerLite) was aligned through the burner. An aperture with 2 mm diameter was used to select a homogeneous part of the laser beam and was relay-imaged onto the center of the burner. In this way, a spatial near-top-hat beam profile could be obtained. The spatial profile was measured using the knife-edge method and is shown in Figure 4.13. The laser fluence was around 70 – 115 mJ/cm^2 which is low enough to minimize the evaporation of soot.

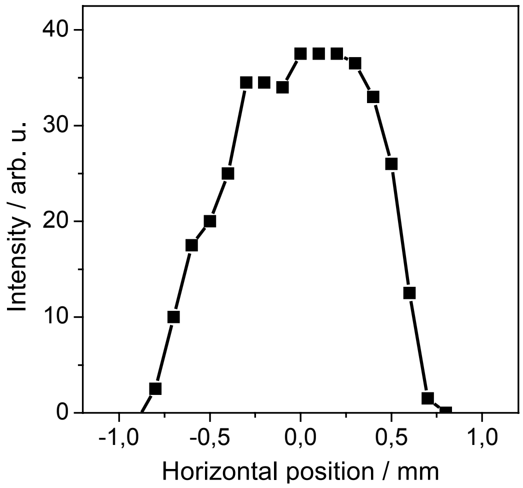

Figure 4.13. Spatial laser beam profile.

The LII signals were detected with fast photomultipliers and were recorded with a digital storage oscilloscope (LeCroy, 300 MHz, 2.5 GS), and transferred to a PC by communication via the RS-232 port. The Nd:YAG laser was triggered externally by a digital delay generator (SRI, model DG535) that triggered the oscilloscope and the image intensifier of the ICCD as well. The main control of the experiment was performed by a PC with the program *DaVis* (LaVision). It was used to trigger and read out the ICCD camera. A macro was written in the CL-macro language of *DaVis* which enabled an automated measurement procedure. The macro controlled the translation system of the burner via the serial port of the PC. The LII signal of a given number of laser shots was averaged on the oscilloscope and the camera, after which both devices were read out by the PC. The burner moved then to the next measurement position and signals were recorded again. The experimental set-up is shown in Figure 4.14.

One series of experiments was performed with NO-seeding to the flame in order to determine the gas-phase temperature from multi-line NO-LIF thermometry. The light of a tunable KrF* laser was Raman shifted in H_2 to ~225 nm to excite NO and the spectrometer was replaced by an ICCD camera equipped with appropriate detection filters. This set-up will be described in more detail in chapter 5.1.

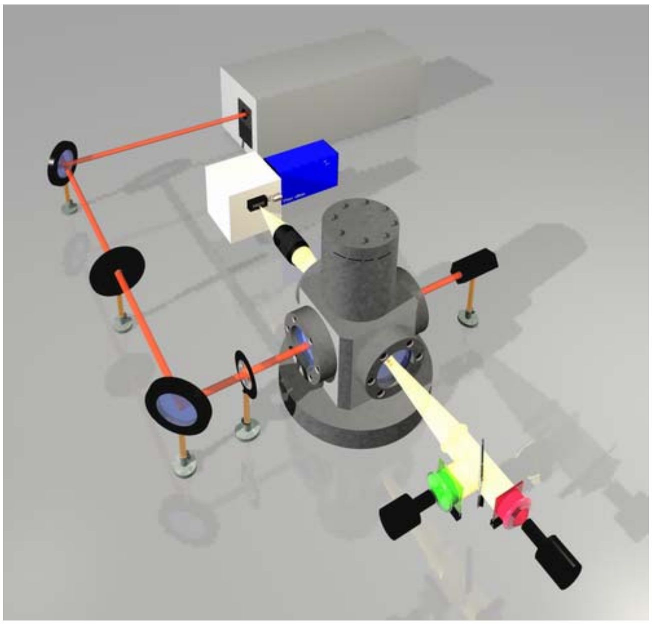

Figure 4.14. Experimental set-up. The LII signal was simultaneously detected with two photomultipliers (front) and spectrally resolved with an imaging spectrometer equipped with an ICCD camera (back).

4.3 TEM probe sampling

Samples from the flame soot were collected for TEM analysis. A device was constructed which enabled thermophoretic sampling at elevated pressure. The device is shown in Figure 4.15. A sluice was constructed that enabled multiple sampling while the burner is running at constant pressure. The vertical position can be varied in order to take samples at different heights above the burner. A rod is equipped with two thin metal sheets with two holes of 2 mm diameter. A grid for electron microscopy could be inserted between the sheets. A TEM grid consists of a mesh of copper wires and has a diameter of 3 mm. The rod with the TEM grid was inserted manually into the flame which resulted in a sampling time of approximately half a second. The soot particles are deposited thermophoretically on the grid due to the temperature difference between the hot gas and the cold grid.

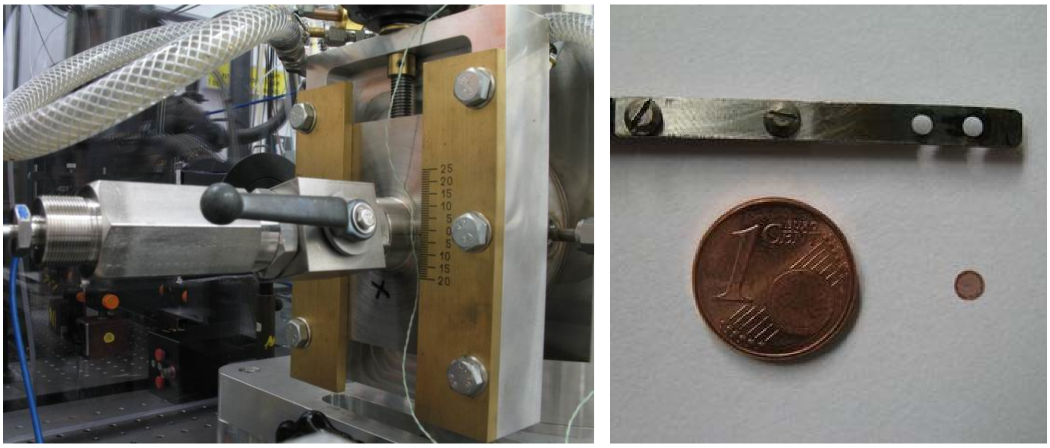

Figure 4.15. Device for taking soot samples of the high-pressure flame for TEM analysis. Left: The sluice device. Right: The tip of the rod with a TEM grid next to it.

Thermophoretic sampling is independent of the particle size and, hence, the sample reproduces the actual particle-size distribution at the measurement location. The grid is oriented parallel to the flow field of the flame in order to minimize the disturbance of the flow. However, one should be aware that this method is not non-intrusive like optical diagnostics and the flame will be disturbed in any case.

A Philips transmission-electron microscope (Model CM 12) at the Universität Duisburg-Essen was used to analyze the samples. Images of the samples were recorded by a CCD camera (1024 x 1024 pixels, 8 bit) and stored for further data analysis.

5 RESULTS

In this chapter, the results of two sets of experiments will be presented and discussed. The first experiment includes the measurement of particle-size distributions at 1 – 5 bar at a single position in the flame of the high-pressure burner. Gas-phase temperatures were obtained by multi-line NO-LIF thermometry. The second series of experiments is a detailed study on the determination of particle-size distributions with LII at different heights above the burner surface for pressures up to 10 bar. The LII signals were evaluated for different heat-conduction models and were compared with data from TEM micrographs.

5.1 LII and multi-line NO-LIF thermometry

The flame used in this experiment was operated at an equivalence ratio of 2.1, corresponding to a C/O-ratio of 0.7, with a gas velocity of 8 cm/s for all pressures, i.e. 1, 2 and 5 bar. The first burner type with the silver capillary tubes was used for the central burner. LII was performed in the fluence range of 0.09 – 0.62 J/cm^2. Measurements were performed with the set-up described in section 4.2.6 at 5 and 10 mm HAB for 1 and 2 bar, and at 5 mm HAB for 5 bar. The model used in this study for LII data evaluation was the model of Kock et al. [37,61].

In order to evaluate the LII signal, the gas-phase temperature is required an input parameter for the LII model. In this study, multi-line NO-LIF thermometry was used to determine the gas-phase temperature. This method has been previously developed [115] and demonstrated in steady stoichiometric and sooting atmospheric-pressure flames [67] as well as in non-sooting high-pressure flames up to 40 bar [116]. The multi-line technique yields absolute temperatures without calibration and can be applied even in systems with strong scattering and fluorescence background. The technique is based on the measurement of LIF excitation spectra of nitric oxide. Some hundreds to thousands ppm NO are added to the fuel/air mixture as a fluorescent tracer. The laser is tuned over a part of the NO absorption spectrum while individual images are taken with an intensified CCD camera for each excitation wavelength. From the resulting stack of pictures (each with the laser tuned to the next wavelength) LIF excitation spectra can be extracted for each pixel. Simulated spectra are then fitted to the experimental data with absolute temperature, broad-band background and total signal intensity as free parameters. The best scan range is determined from a numerical analysis based on LIFSim [67,103]. The technique takes advantage of the shape of the spectra (as a function of excitation wavelength) for each pixel within the observed area. In contrast to two-line temperature imaging, broadband background (due to incompletely suppressed elastic scattering and due to broadband fluorescence) does therefore not affect the temperature evaluation.

For the temperature measurements a tunable KrF* excimer laser (248 nm) was frequency-shifted to 225 nm in a 10-bar hydrogen-filled Raman cell. The laser beam was focused to approximately 2 × 2 mm^2 and illuminated the region of interest. The NO molecules were excited in the A-X(0,0) band and the LIF-signal was recorded with an intensified CCD camera. Elastically-scattered light was suppressed by Schott UG5 filters. An additional reflection band pass filter separated the 230 – 250 nm range for detection. The total set-up is shown in Figure 5.1.

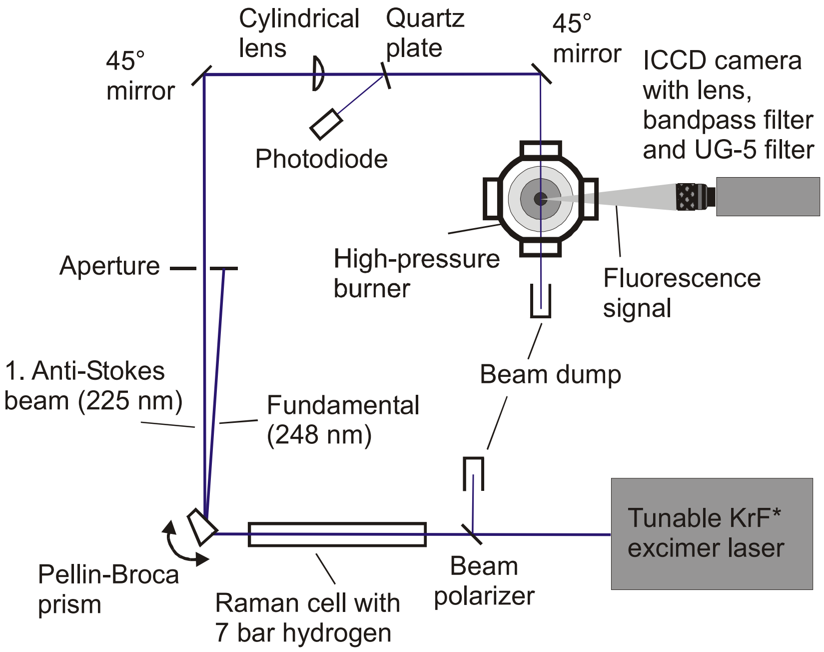

Figure 5.1. Experimental set-up of the multi-line NO-LIF thermometry.

The optimum scan range [67] was a 10 cm^{-1} range with an excitation scan from 44407 – 44417 cm^{-1} (225.190 – 225.139 nm). 56 individual LIF images are taken at different wavelengths each averaged over 100 laser shots. This gives a total of 5600 laser shots for the excitation spectra. The spectra acquisition, therefore, takes about five minutes at a repetition rate of 25 Hz of the KrF* excimer laser system and the synchronized ICCD-camera. The gas temperature in the center (region of 10 mm wide × 2 mm high) of the flame at 1 bar was 1644 ±30 K and 1600 ±20 K at 5 mm and 10 mm above the burner surface respectively. Temperatures at 2 bar are 1665 ±20 K and 1710 ±20 K at 5 mm and

10 mm HAB respectively. At 5 bar, gas temperatures are 1850 ±100 K at 5 mm above the burner surface. NO-LIF excitation spectra are shown in Figure 5.2.

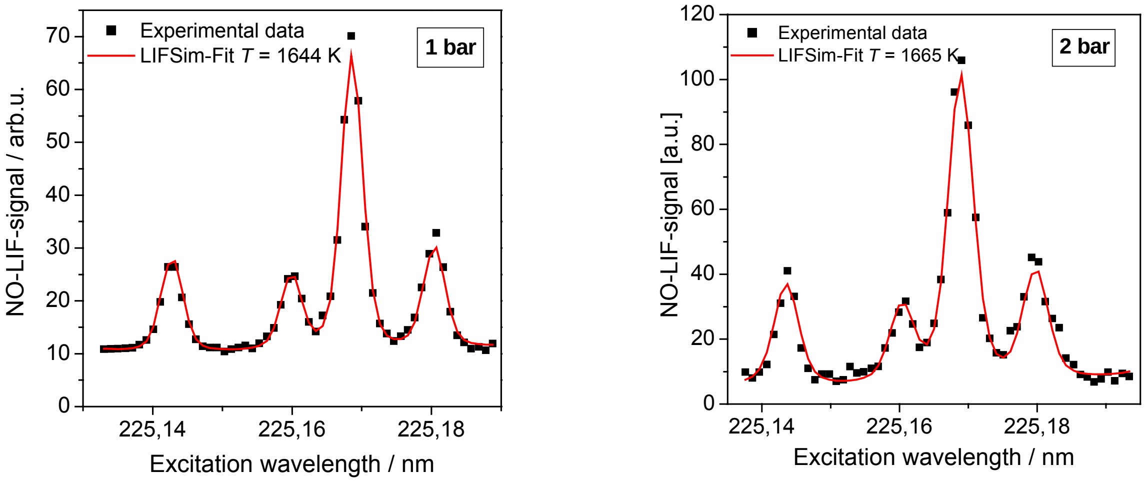

Figure 5.2 NO-LIF excitation spectra at 1 and 2 bar. The black dots are experimental data observed at 5 mm height above burner. The line shows the fitted spectra.

The precision of the temperature measurements depends on the signal-to-noise ratio of the experimental excitation spectra. It can be improved by increasing signal averaging and by using optimized detection filters. NO was seeded to the premixed ethylene/air mixture in amounts of 0.5 % at 1 and 2 bar and 2 % NO at 5 bar. High NO concentrations were required to generate sufficient LIF signal due to strong re-burn of added NO in rich flames. Spectral broadening additionally reduces signal intensities with increasing pressure. In the present set-up poor UV transmission of the windows further reduced the laser and signal intensities. The elastically-scattered light was well suppressed by the filters described above.

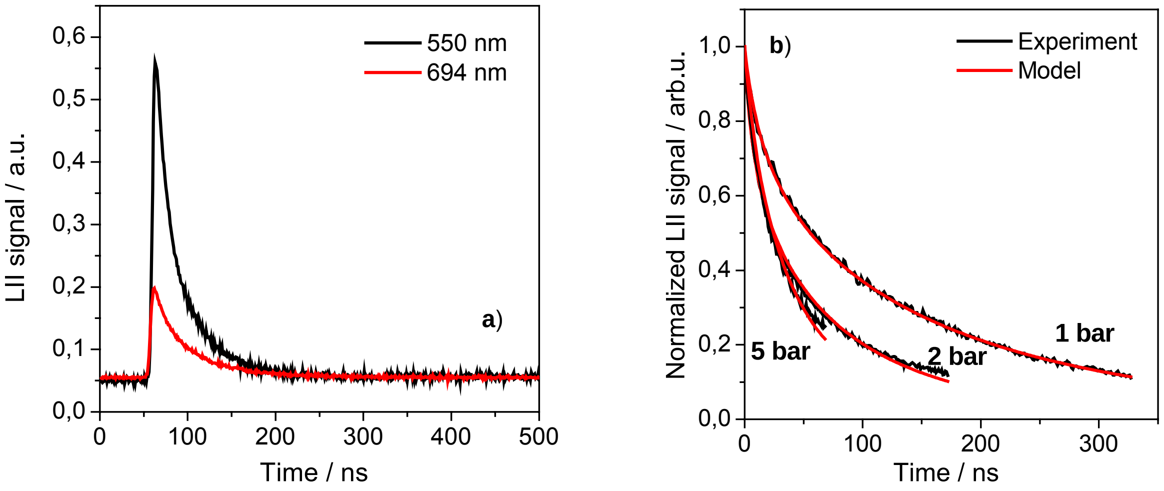

Figure 5.3. Typical LII signal at 5 bar detected at 550 and 694 nm (a). Numerical fits to the experimental LII decay curves at 550 nm detection for 1, 2 and 5 bar (b).

A typical raw LII signal at 5 bar is shown in Figure 5.3a. Two signals are shown for both the 550 nm and the 694 nm detection. The signals are averages over 40 laser shots and were taken at 5 mm height above the burner with a laser fluence of 0.16 J/cm^2. From the ratio of the peak intensities at the two wavelengths the peak particle temperature was calculated. With the gas-phase temperatures obtained from the multi-line NO-LIF thermometry the numerical model was fitted to the LII signal decay curves. The fits are shown in Figure 5.3b. Fits at 1 and 2 bar are given for LII decay curves at 10 mm height above the burner and at 5 mm height above the burner at 5 bar. Laser fluences were 0.09 J/cm^2, 0.22 J/cm^2 and 0.16 J/cm^2 for 1, 2 and 5 bar respectively. With increasing pressure, heat conduction increases whereas evaporation decreases. Hence, one could expect that evaporation becomes less important with increasing pressure. However, fluences higher than ~ 0.25 J/cm^2 resulted in a poor fit for all pressures. Hence, up to 5 bar, it is important to use low fluences for fitting LII decay curves like in the atmospheric case. The 1 and 2 bar data were fitted with the model with free-molecular heat conduction. At 5 bar, the model for the transition regime was used. In Table 5.1, the resulting count median diameter and the geometric standard deviation are listed. At 5 bar a relative small particle diameter of 10 nm is found. In premixed flames particle sizes increase with increasing height above the burner – at 5 bar the measurement location was at 5 mm HAB whereas it was 10 mm HAB at 1 and 2 bar.

p / bar	**HAB / mm**	**T_p^0 / K**	**T_g / K**	**CMD /nm**	**σ_g**
1	10	3758	1600	44	1.49
2	10	3854	1710	31	1.54
5	5	3568	1850	10	1.84

Table 5.1. Results of the measured temperatures and fit parameters of the comparison of the LII signal decay with the model at 1– 5 bar.

In this experiment, the laser fluence might have been too high for a quantitative interpretation of the particle size. The fits at 2 and 5 bar show some discrepancies at the end of the signal. Even before the vaporization temperature of 3915 K is reached, soot can be vaporized. Since the vaporization model is subject to some uncertainty, fits in the high-fluence regime are not that accurate.

5.2 Particle-size distributions obtained by LII at 1 – 10 bar

In this study, a detailed analysis was performed on the ability of LII as a tool for the determination of the log-normal soot particle-size distribution in premixed, sooting ethylene/air flames at pressures up to 10 bar. A comparison between different, commonly applied LII sub-models, used for LII data reduction, was performed. These data were compared with data from TEM micrographs. Investigations were performed at 1, 2, 5 and 10 bar ambient pressure in premixed, ethylene/air flames. The second version of the burner with a 10 mm thick disc of sintered, stainless steel as central flame holder was used to stabilize the flames. The equivalence ratios used were $\phi = 2.1$ for 1 and 2 bar and $\phi = 1.95$ for 5, and 10 bar with a fresh gas velocity of 8 cm/s for 1 – 5 bar and 6 cm/s for

10 bar. Explicit mass flows and pictures of the flames were given in section 4.1.3. Data were taken at the burner's centerline from 2 – 20 mm HAB in steps of 2 mm.

5.2.1 Two-color LII

The LII signal was detected temporally resolved at 550 and 694 nm. The signals were sampled with 500 MS at 1 bar and 1 GS for 2 – 10 bar resulting in one data point per 2 and 1 ns respectively. LII signals were averaged over 170 laser shots. The baseline-subtracted signals for the different pressures at 20 mm HAB are shown in Figure 5.4.

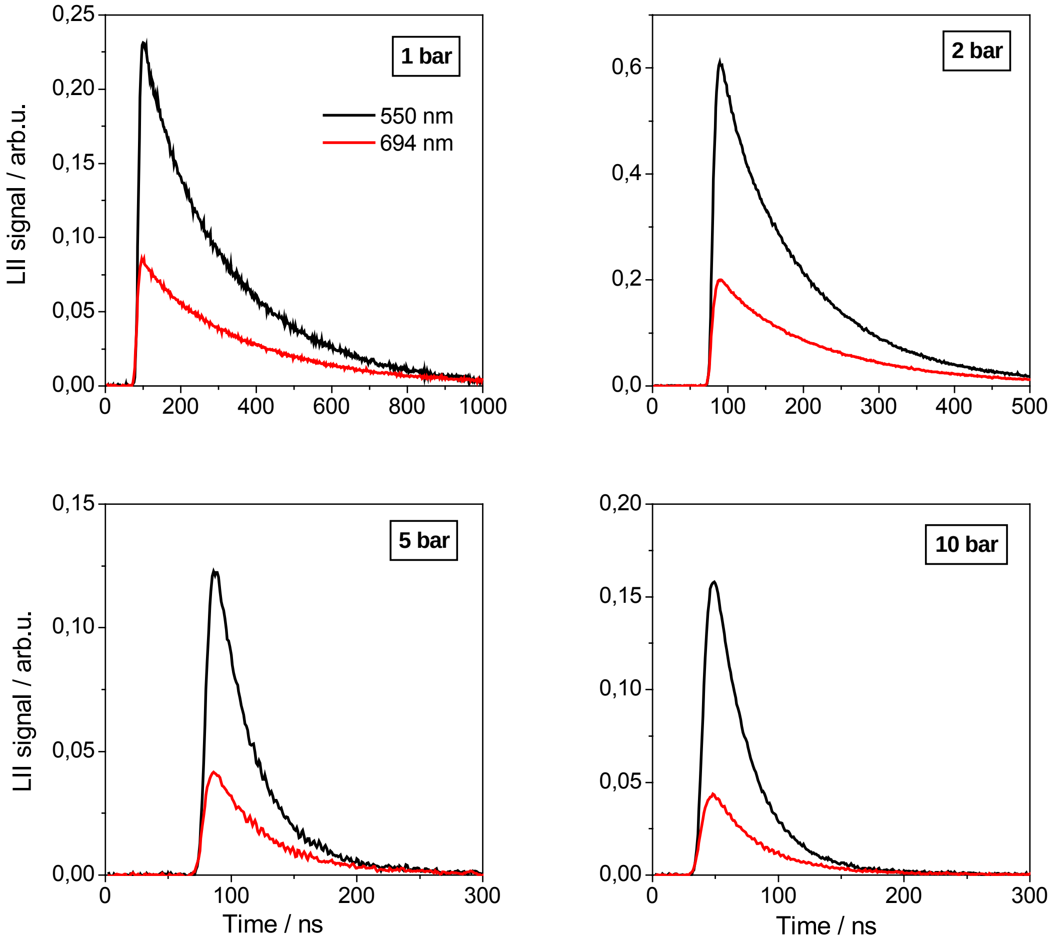

Figure 5.4. LII signals for 1 – 10 bar detected at 550 and 694 nm at 20 mm HAB.

The black-body radiation of particles in the order of 3000 K is stronger at 694 than at 550 nm. However, the detection system, i.e. the combination of bandpass filter and photomultiplier, is more sensitive at 550 than at 694 nm. Therefore, the LII signal at 550 nm is stronger than the signal at 694 nm. The LII signal decreases faster with increasing pressure due to an increased heat conduction at elevated pressure which has been reported before [14].

From the ratio of the peak values (including the baseline off-set accounting for the temperature coming from the non-heated soot particles) the peak particle temperature is calculated from pyrometry. The peak particle temperature vs. height above the burner for the different pressures is shown in Figure 5.5.

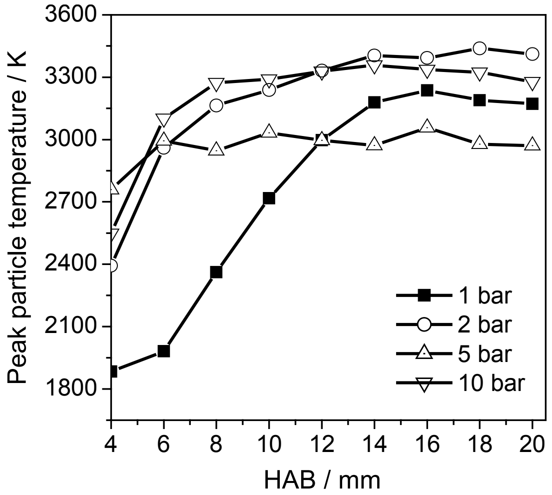

Figure 5.5. Peak particle temperature after laser heat-up vs. height above the burner.

Low fluences of 70 – 115 mJ/cm^2 were used to heat the particles in order to avoid soot evaporation. The obtained peak particle temperatures are below 3500 K for all pressures which is well below the vaporization temperature of 3915 K at atmospheric pressure. At 1 bar, the peak particle temperature increases gradually with increasing height above the burner until a near-constant temperature of ~3200 K is reached. The soot absorption function might be a function of the particle size. A smaller value of *E(m)* for small particles would result in lower peak temperatures. Soot particles in the type of flame that is used in this study gradually grow with increasing height above the burner. The process is slower at low pressures than at high pressures. At high pressure, the soot particles reach a final size much faster than at atmospheric pressure. This explains the less pronounced change in peak particle temperature vs. height above the burner for the higher pressures. However, no data are available about the dependence of *E(m)* on the particle size.

5.2.2 Spectrally-resolved LII

Emissions from the C_2 $d^3\Pi_g \rightarrow a^3\Pi_u$ Swan bands have been reported to interfere with the LII signal at high laser power densities [22], and even emissions from OH and O atoms have been observed with 532-nm excitation [25]. C_2 Swanband emissions can also be observed with 1064-nm excitation at high laser fluences, especially with non-uniform beam profiles that provide high local fluence [25]. C_2 Swanband emissions appear at 473 nm (Δv = +1), 516 nm (Δv = 0), 563 nm (Δv = –1), and 618 nm (Δv = – 2). Hence, potential interferences at the 550 nm detection channel used in this study can be expected. Therefore, the LII signal was detected spectrally resolved with an imaging spectrometer equipped with an ICCD camera.

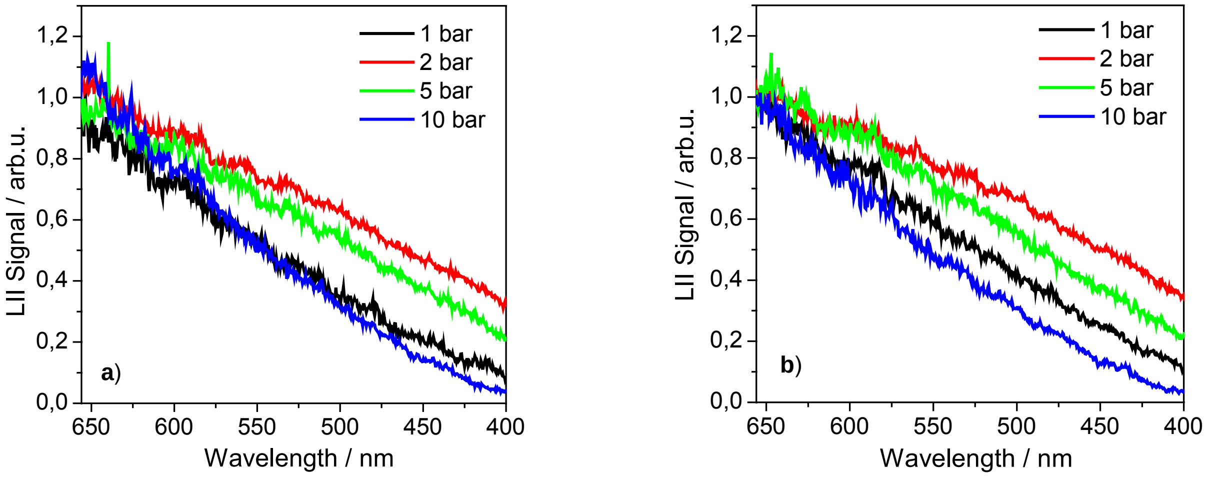

Figure 5.6. Spectrally-resolved LII signal for 1 – 10 bar at 10 mm (a) and 20 mm (b) HAB.

The LII emission spectra are shown in Figure 5.6 at 10 and 20 mm HAB respectively. The spectra have been normalized at 656 nm. No interference of narrow-band emissions can be seen in the region of 656 to 400 nm. Small ripples result from not entirely suppressed streaks in the background of the CCD image. Hence, a laser beam at 1064 nm with a homogeneous spatial energy distribution at low fluences of 70 – 115 mJ/cm^2 does not produce any significant interferences in the LII signal up to 10 bar. However, higher fluences can result in interferences at this excitation wavelength.

5.2.3 Flame temperature

The gas-phase temperature is required in order to determine particle sizes from LII decay curves. Pyrometry of soot at flame temperature has been used to determine the flame temperature. Two issues have to be considered when using this technique. First, this method is a line-of-sight technique and does not give the temperature at the LII measurement location. However, a premixed flat flame is used in this study. Nevertheless, there might be a slight temperature gradient from the center towards the edge of the flame and the obtained temperature might deviate from the true temperature at the centerline. Still, this error is much smaller than in the case of a diffusion flame with steep temperature gradients or a turbulent combustion with strongly varying local soot and temperature distributions. Second, the obtained temperature is the soot temperature and not the gas-phase temperature. However, it can be assumed that these temperatures are similar when particle and gas phase are in thermal equilibrium [117]. Comparisons between soot pyrometry and multi-line NO-LIF thermometry in a laminar, premixed ethylene/air flame at atmospheric pressure have shown that both methods are in reasonably good agreement at positions in the flame with sufficient soot [63].

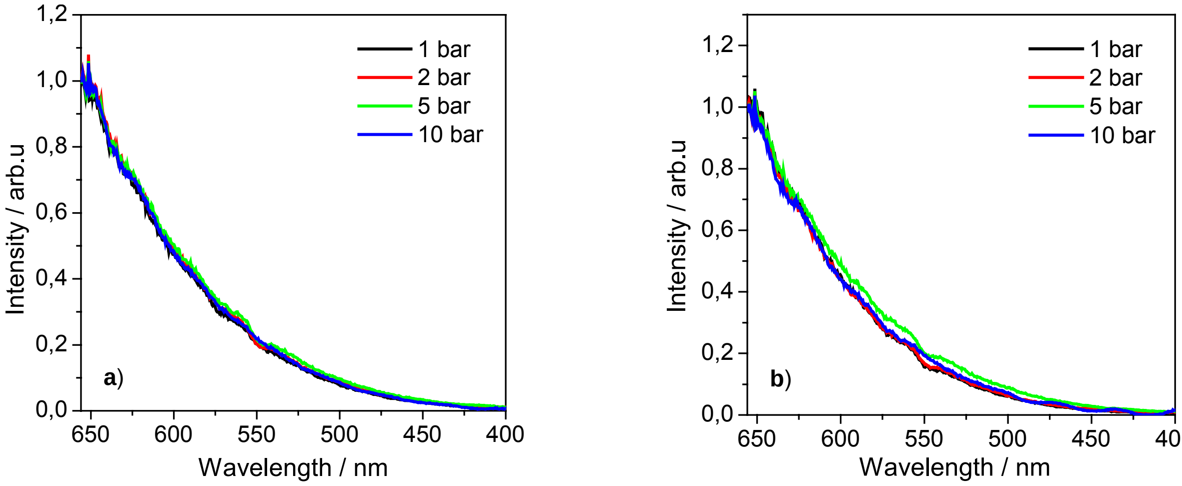

Figure 5.7. Soot emission spectra for 1 – 10 bar at 10 mm (a) and 20 mm (b) HAB.

The soot emission spectra for two different positions in the flame are shown in Figure 5.7. They have been corrected for the spectral sensitivity of the detection system and are normalized to 1 at 656 nm. The temperature can be derived by either fitting Planck functions to the spectra or by taking the ratio of the signal at two given wavelengths. For the first method, the emissivity of soot and, hence, the soot absorption function is required. As the absolute value of *E(m)* is related to large uncertainty, the second method has been used. In that case, only the ratio of *E(m)* at the two detection wavelengths is used (see section 2.1.2). The signal at 530 ± 5 nm and 640 ± 5 nm has been used to calculate the temperature. The results are shown in Figure 5.8.

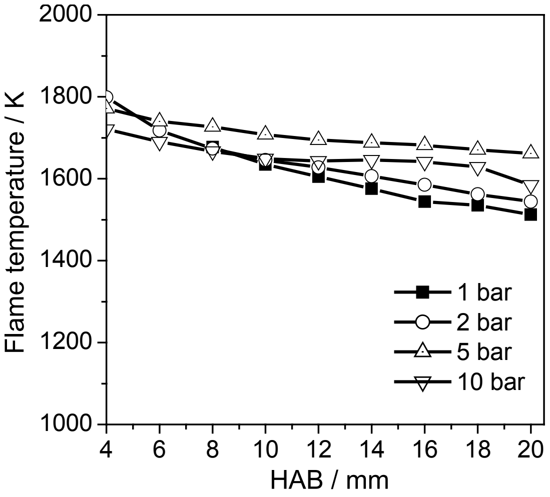

Figure 5.8. Flame temperature obtained from two-color pyrometry as a function of height above the burner.

The temperatures increase slightly from 1 – 5 bar. For these conditions, the fresh-gas velocity was the same, i.e. 8 cm/s. The mass-flow rates increase linearly with pressure for the same fresh gas velocity and more fuel is burned at higher pressure – resulting in higher flame temperatures. For 10 bar, a slower fresh gas velocity of 6 cm/s was used and, hence, the temperatures are lower than at 5 bar. With increasing height above the burner, the temperature decreases slowly. The main reaction zone is at the first few millimeters above the burner surface and the reaction heat is produced in that region. The reaction products are then carried to higher heights and cool down, resulting in the slow temperature decay shown in Figure 5.8.

5.2.4 TEM results

Soot samples were collected from the flame at 10 and 20 mm height above the burner with the device described in section 4.3. TEM images were recorded of the samples. They are shown in Figure 5.9. All images are shown for a magnification of 40.000. The primary particles are loosely connected and form aggregates at all pressures. The aggregate size is larger at 20 mm HAB than at 10 mm HAB because the primary particles form aggregates with increasing size with increasing height above the burner. Very small particles, in comparison to the other pressures, can be observed at 5 bar. The particle size depends on temperature; with increasing temperature, particles become smaller. The flame temperature at 5 bar was higher compared to the other pressures – resulting in smaller particles at this pressure.

The images were calibrated, i.e. 1024 x 1024 pixels correspond to 733 x 733 nm at a magnification of 40.000 With the freely available software ImageTool (version 3.0), the diameter of 100 – 300 primary particles was measured in several images taken from the same sample. The obtained diameters were divided into classes of the same primary particle size. In such a way, a histogram was obtained which shows the number of particles (counts) per particle-size class. The histograms were then fitted by a log-normal particle-size distribution with the mean diameter, the geometric width and an intensity scaling parameter as free fit parameters. The primary particle-size statistics are shown in Figure 5.10. A log-normal distribution fits the particle sizes well for all investigated pressures.

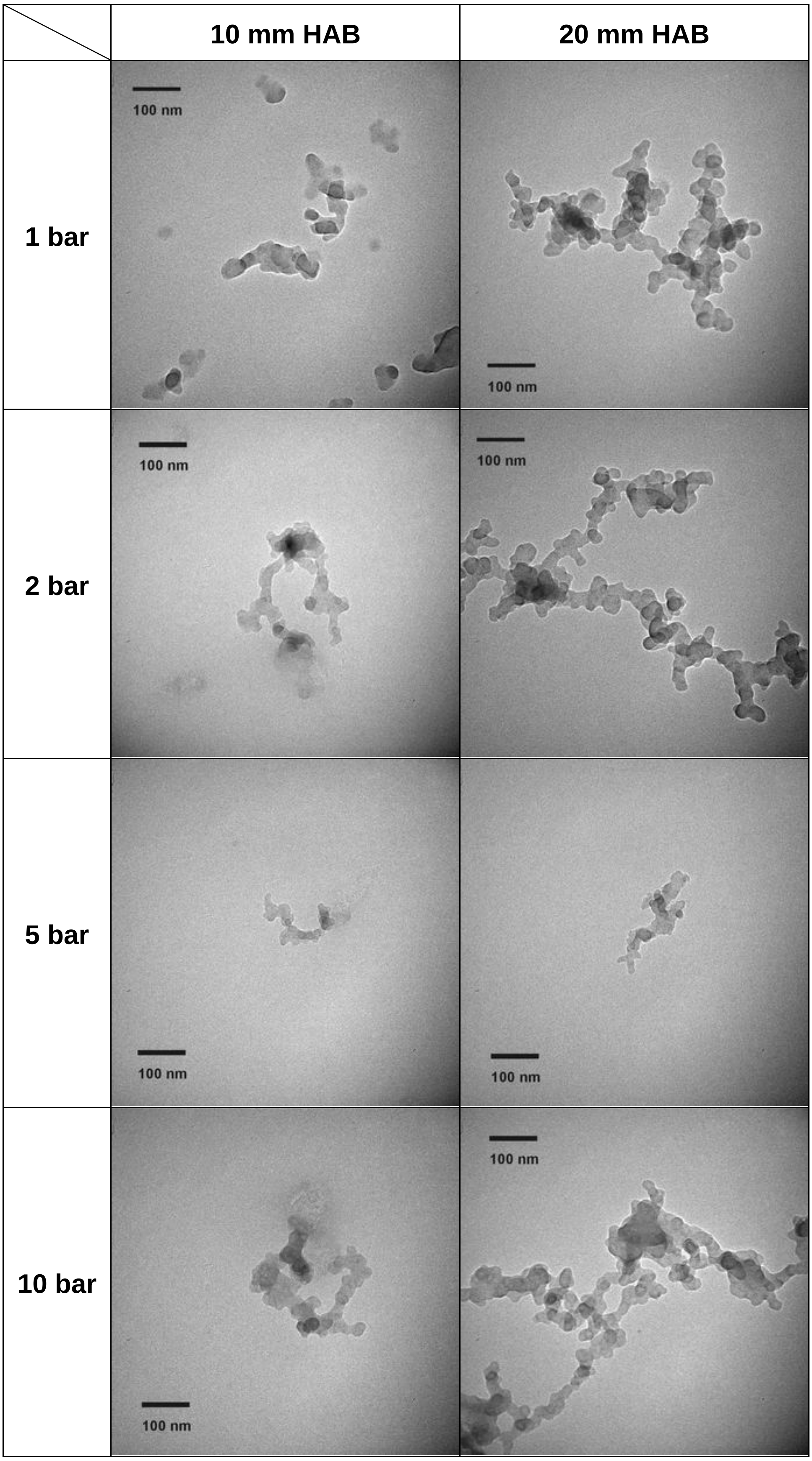

Figure 5.9. TEM micrographs for 1 – 10 bar from soot samples taken at 10 and 20 mm HAB.

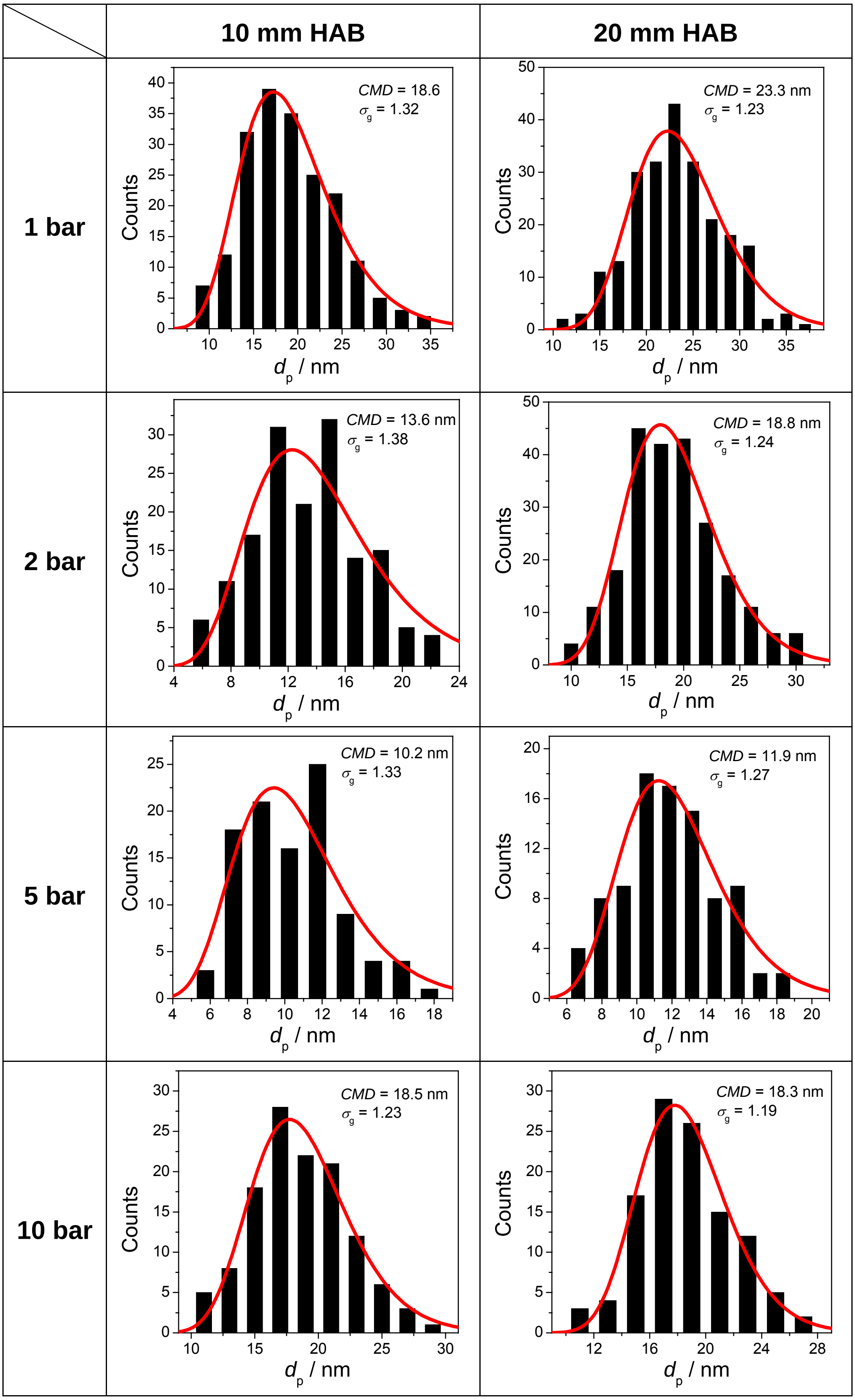

Figure 5.10. Primary particle sizes counted in TEM images (bars) with best log-normal fit (line).

5.2.5 Determination of the particle-size distribution with LII

The primary particle-size distribution has been determined with LII as well. The LII signal at 550 nm was used for data evaluation. The signal before the peak was disregarded. To avoid an overlap of particle cooling and laser pulse, 13 data points after the signal peak (i.e. 26 ns at 1 bar and 13 ns at 2 – 10 bar) were deleted before the LII model was fitted to the signal decay. The initial cooling temperature was determined at this point with two-color LII and is therefore slightly below the actual peak temperature shown in Figure 5.5. At this early point after the LII signal peak, a difference in the different cooling behavior of small and large particles can be still neglected. The gas-phase temperature was taken from the pyrometry data described in section 5.2.3.

One aim of this study was to identify differences in commonly used heat conduction models used in literature. They have been described in detail in chapter 2.2. Briefly, these are the free-molecular model, the two-layer model of Fuchs, the model of McCoy and Cha, and the Fuchs model taking into account the reduced heat conduction from aggregates. Additionally, the Fuchs model was applied with the often used simplified expression for the change in internal energy – that is the expression in which the temperature-dependence and, hence, time-dependence of the particle mass and particle heat capacity are ignored. The different models were combined with the Levenberg-Marquardt fitting algorithm. Whereas the heat conduction sub-model was changed, all other parameters were kept constant. Physically, it is incorrect to take different values for quantities like the accommodation coefficient or the heat capacity if different heat conduction models are applied. The accommodation coefficient used was 0.3 which is typical for soot in flames [13]. However, one should be aware that this value is subject to some uncertainty.

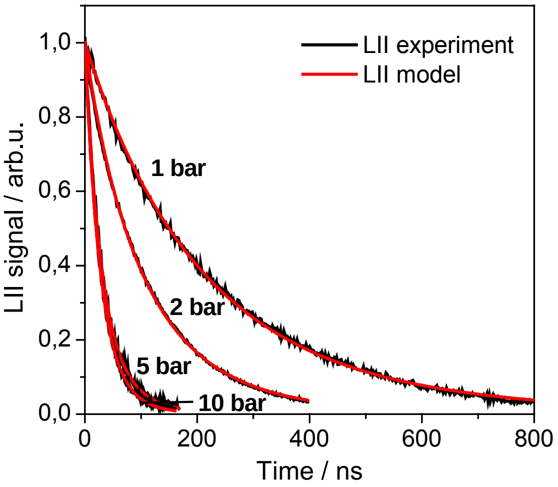

Figure 5.11. Numerical fits to experimental LII decay curves. This example is shown at 20 mm HAB for the Fuchs model taking into account the effect of aggregation.

Typical numerical fits to experimental LII decay curves are shown in Figure 5.11. The Fuchs model with the assumption of aggregated particles has been used in this specific graph. In general, all models give excellent fits to the experimental data. The difference in the models used for data evaluation lies in the different values that were obtained for the count median diameter (*CMD*) and the geometric width (σ_g) of the particle-size distribution. The results are shown in the following sections.

Count median diameter of the particle-size distribution

The obtained *CMD* for the different models as a function of height above the burner is shown in Figure 5.12.

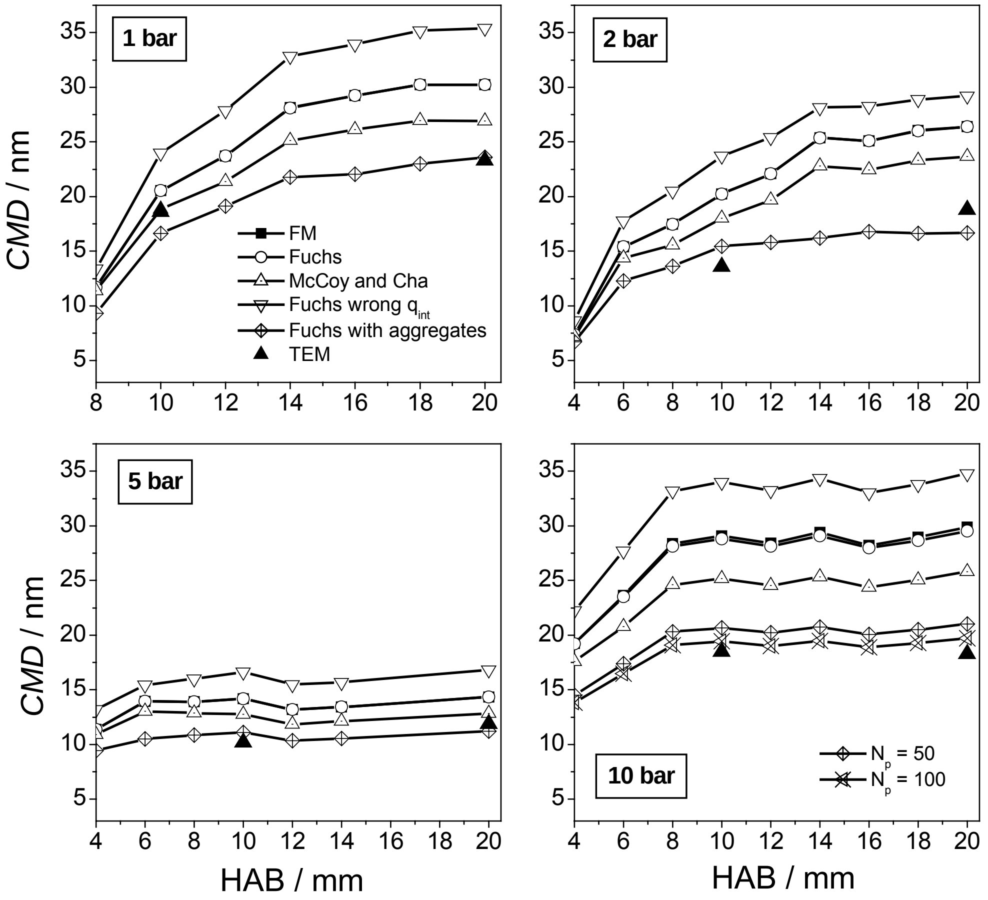

Figure 5.12. Evaluated count median diameter of the log-normal particle-size distribution as a function of height above the burner (HAB) for 1 – 10 bar. The results are shown for the free-molecular heat conduction model (solid squares), Fuchs' model (open circles), the McCoy and Cha model (open triangles tip up), Fuchs' model with the simplified expression for the internal energy (open triangles tip down), and Fuchs' model with the assumption of 50 primary particles per aggregate (open diamonds). For 10 bar, the evaluation is additionally shown for 100 primary particles per aggregate (crossed open triangles). The solid triangles show the results of the TEM analysis.

In general, the particle size increases with increasing height above the burner. The particles reach a final size at a certain height when the soot growth has finished. The obtained particle sizes differ significantly for the different models used for data evaluation. The Fuchs model with the simplified expression for the change in internal energy results in the largest particle diameter for all pressures, i.e. 35, 29, 17, and 35 nm at

20 mm HAB for 1, 2, 5, and 10 bar respectively. The smallest particle diameter is obtained by the Fuchs model with aggregates. For N_p = 50, the *CMD* at 20 mm HAB is 24, 17, 11 and 21 nm for 1 – 10 bar respectively. At 10 bar, the result for an aggregate of N_p = 100 is shown as comparison – the diameter is 20 nm at 20 mm HAB, i.e. 5% less than for N_p = 50. It is difficult to determine the exact aggregate size. The aggregate size shows, similar to the primary particle size, a log-normal size distribution [91]. However, introducing a log-normal aggregate-size distribution would increase the number of unknown parameters in the LII model and, therefore, make the interpretation of the obtained results even more difficult. In this approach, an average, constant aggregate size of 50 primary particles per aggregate was assumed for all measurement locations. It has been shown in chapter 2.2.10. that the influence of aggregates on heat conduction is most significant for the first 50 – 100 particles per aggregate. For larger aggregates, the decrease in heat conduction compared to non-aggregated particles levels off. In flame soot, aggregates usually consist of at least 50 primary particles. Therefore, an assumption of N_p = 50 seems reasonable. Modeling LII has shown in chapter 3.3.1 that the influence of increasing aggregate sizes has only minor effects at atmospheric pressure, but a more significant effect at higher pressures. Therefore, an aggregate size of N_p = 100 is considered additionally at 10 bar. It can be seen from Figure 5.12 that this has only a minor effect relative to the case of N_p = 50 compared to the change in particle size when aggregation is not considered at all. Of course, the change from 50 to 100 primary particles per aggregate is only a factor of 2 compared to the factor of 50 for the change from a single primary particle to an aggregate of 50 primary particles. However, typical aggregates do not consist of thousands of primary particles and 50 – 100 particles per aggregate are realistic numbers as can be seen from the TEM images shown in section 5.2.4.

The free-molecular model and the Fuchs model, which provides a smooth transition from the free-molecular regime to the continuum regime, result in nearly the same particle size for all pressures. Apparently, the transition regime has not been reached at 10 bar for the given flame conditions. The Knudsen number at 20 mm HAB is ~3.4 at 10 bar. Under these conditions, the free-molecular regime describes heat conduction still very well. However, if aggregation is taken into account, heat conduction is shifted further towards the transition regime and slight differences appear between the free-molecular and the Fuchs model (not shown in Figure 5.12). Therefore, the aggregate sub-model was used in combination with the Fuchs model.

The results of the TEM analysis are shown as solid triangles. The Fuchs model with the aggregation sub-model is in very good agreement with the TEM results for all pressures. All other models result in too large particle diameters. In order to quantify this result in more detail, a sensitivity study on a variation in the experimental input parameters, i.e. the peak particle temperature and the gas-phase temperature, was performed. This is shown in Figure 5.13.

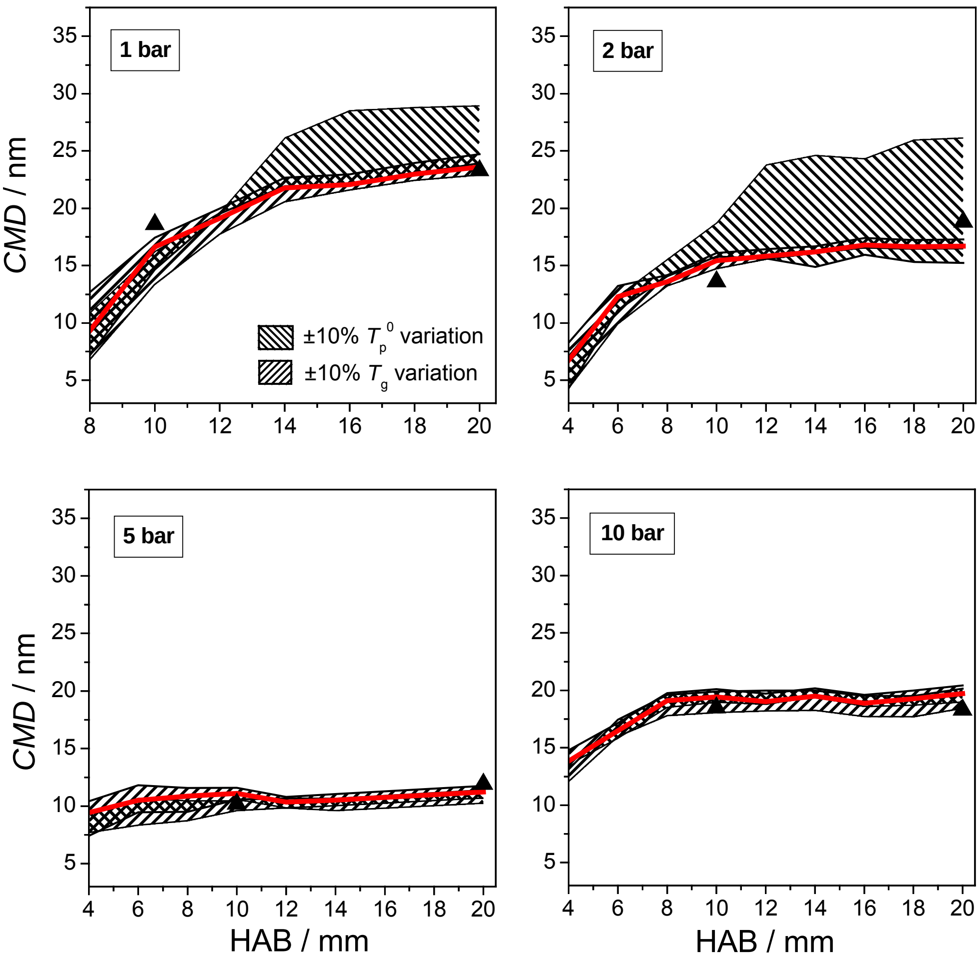

Figure 5.13. Sensitivity of the obtained count median diameter to a ±10% variation in assumed peak particle temperature T_p^0 and to a ±10% variation in assumed gas-phase temperature T_g. The analysis is based on the Fuchs model with 50 primary particles per aggregate for 1– 5 bar and 100 primary particles per aggregate for 10 bar (solid line). The TEM results are shown as solid triangles.

The solid line is the results of the analysis with Fuchs' model with 50 primary particles per aggregate for 1 – 5 bar and 100 primary particles per aggregate for 10 bar. The two dashed areas correspond to the obtained *CMD* if the peak particle temperature or the gas-phase temperature, that are required as input for the data evaluation, are changed by ±10% respectively. A variation of ±10% in the gas-phase temperature has only minor effects on the obtained *CMD* for all pressures. However, the obtained *CMD* is relatively sensitive to a ±10% variation in peak particle temperature for 1 and 2 bar. The sensitivity is smaller at higher pressures which indicates that LII is a robust method to correctly quantify the count median diameter at elevated pressure if the Fuchs model with aggregates is applied for data evaluation.

Geometric width of the obtained particle-size distribution

The obtained geometric width of the log-normal particle-size distribution for the different models as a function of height above the burner is shown in Figure 5.14. The models and assumptions used are the same as those used for the count median diameter – which is self-explanatory as both parameters are determined from the same fit.

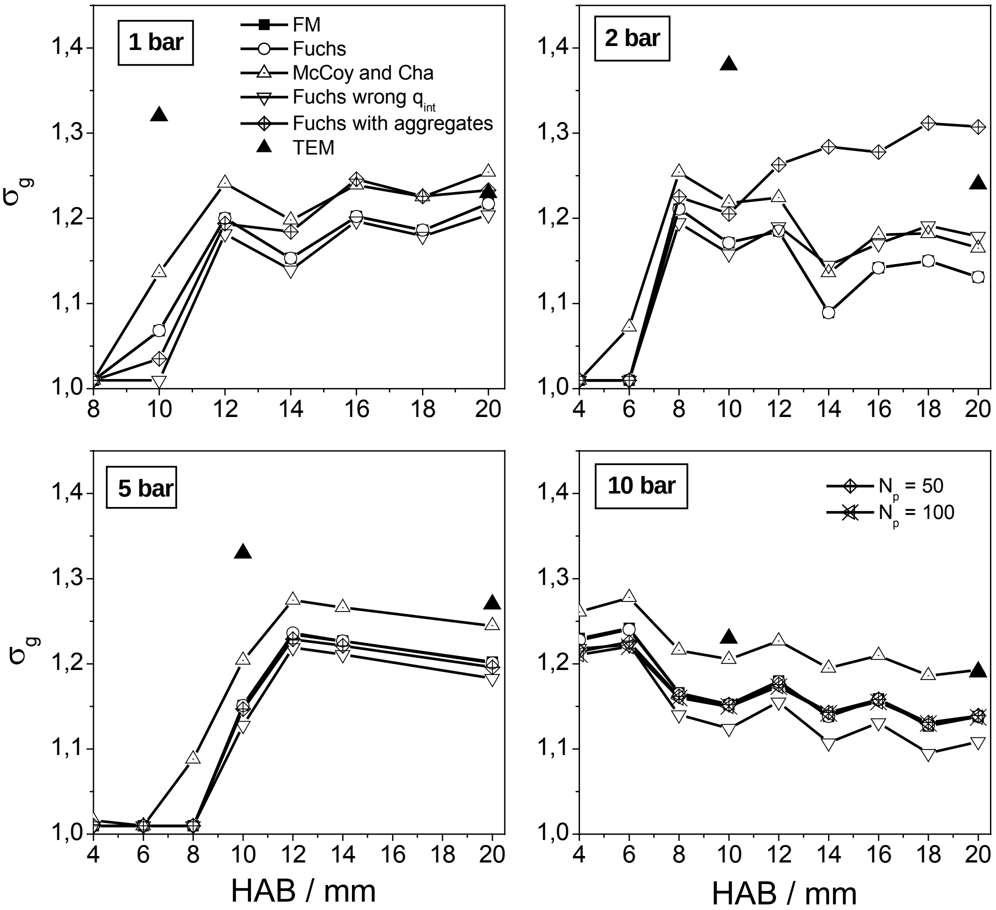

Figure 5.14. Evaluated geometric width of the log-normal particle-size distribution as a function of height above the burner (HAB) for 1 – 10 bar. The results are shown for the free-molecular heat conduction model (solid squares), Fuchs' model (open circles), the McCoy and Cha model (open triangles tip up), Fuchs' model with the simplified expression for the internal energy (open triangles tip down), and Fuchs' model with the assumption of 50 primary particles per aggregate (open diamonds). For 10 bar, the evaluation is additionally shown for 100 primary particles per aggregate (crossed open triangles). The solid triangles show the results of the TEM analysis.

In general, σ_g increases with increasing height above the burner and remains more or less constant from a certain height. The free-molecular model and the Fuchs model give the same results like in the case of the *CMD*. For 1, 5 and 10 bar, the Fuchs model with the simplified expression for the internal energy results in the lowest value of σ_g – at 2 bar it is the free-molecular and the Fuchs model. The McCoy and Cha model results in the largest value for σ_g for 1, 5 and 10 bar, whereas it is the Fuchs model with aggregates at 2 bar. For the different models, a σ_g between 1.01 and 1.31 is obtained. 1.01 is chosen as the lower boundary for the fit of σ_g because 1.0 is the monodispere case. The result of the TEM analysis at 20 mm HAB is a σ_g of 1.23, 1.24, 1.27, and 1.19 for 1, 2, 5, and 10 bar respectively. The LII results are in rough agreement with the TEM results though there is no pronounced model which can be identified as the most correct one. At 1 and 2 bar, the LII results under-predict the TEM result.

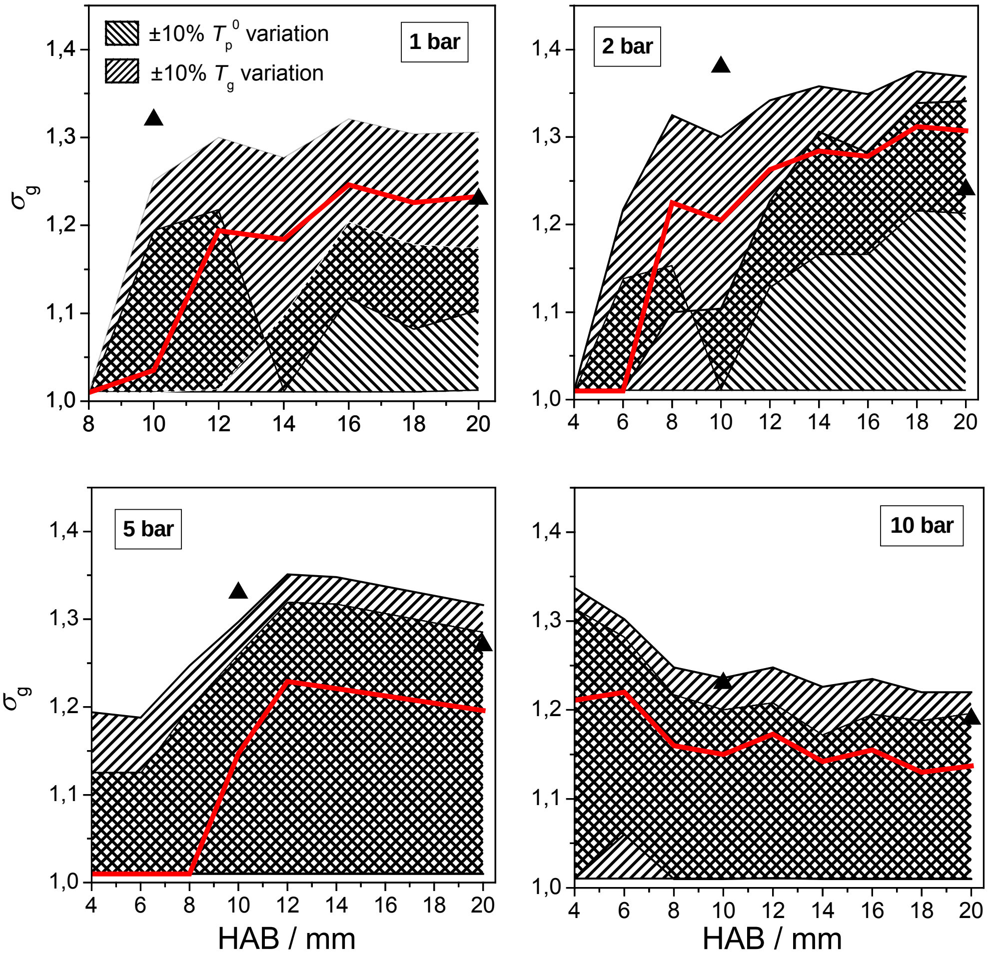

Figure 5.15. Sensitivity of the obtained geometric width to a ±10% change in peak particle temperature and to a ±10% change in gas-phase temperature. The analysis is based on the Fuchs model with 50 primary particles per aggregate for 1– 5 bar and 100 primary particles per aggregate for 10 bar (solid line). The TEM results are shown as solid triangles.

Again, a sensitivity study on a variation in the peak particle temperature and the gas-phase temperature was performed. This is shown in Figure 5.15. The solid line is the result of the analysis with Fuchs' model with 50 primary particles per aggregate in case of 1 – 5 bar and 100 primary particles per aggregate for 10 bar. The two dashed areas correspond to the obtained σ_g if the peak particle temperature or the gas-phase temperature are changed by ±10% respectively. Within the assumed uncertainty, the Fuchs model with aggregates agrees with the TEM results in most cases. However, large deviation in the determined σ_g occur when either the peak particle temperature or the gas-phase temperature is changed. For a 10% decrease in T_p^0 or for a 10% increase of T_g, the lower limit of 1.01 of the geometric width is reached. A ±10% variation in the peak particle temperature does not necessarily lead to a higher or lower value of the obtained σ_g respectively. At 2 bar, for instance, both an increase or decrease in T_p^0 will result in a lower value of σ_g. Hence, the overall sensitivity of the geometric width to any changes in the peak particle temperature or the gas-phase temperature is high.

5.2.6 Discussion

The results presented show that the most accurate heat-conduction model for LII data evaluation is the Fuchs model taking into account the effect of aggregated particles. Excellent agreement is found for the count median diameter of a log-normal particle-size distribution using this model with the independent results obtained from TEM analysis of soot samples taken at the LII measurement location. The poorest result is obtained from the heat-conduction model which uses the often applied, simplified expression for the change in internal energy.

The geometric width of the particle-size distribution is more difficult to obtain with LII. Although the width, obtained from TEM analysis, is roughly represented by the Fuchs model with aggregates as well, it is very sensitive to variations in experimental input parameters like the peak particle temperature and the gas-phase temperature. It should be noted that no detailed investigations on the ability of LII to determine particle-size *distributions* have been reported so far:

Initial particle sizing experiments in LII were performed to obtain particle sizes under the assumption of *monodisperse* particles. In some cases they were compared with scattering and extinction data without the exact knowledge of the aggregate structure of soot. Examples are the work of Will et al. in 1996 and 1998 [32,33], Axelsson et al. in 2000 [27], and Schittkowski et al. in 2002 [118] who determined monodisperse soot particle sizes with LII in flames.

Roth and Filippov reported the determination of log-normal distributions from a real two-parameter fit with LII for the first time in 1996 [56]. However, they did not compare their results with an independent method. Lehre et al. [34] took into account a log-normal particle-size distribution for the determination of particle sizes in premixed flames. However, the geometric width was obtained from other independent studies and was used as fixed input parameter for the LII model. On the other hand, in his work, three other parameters of the LII model were fitted simultaneously which is highly questionable in case of a rather unspecific, monotonic signal decay. Boiarciuc et al. [57] determined the particle-size distribution in a laminar diffusion flame at atmospheric pressure. In that case, the geometric width of the distribution was taken from TEM data – no simultaneous fit of both the mean diameter and the width of the distribution was performed. Dankers et al. [119] determined log-normal particle-size distributions of carbon black from exponential fits to the LII signal at two different delay times. They observed good agreement with TEM results for the count median diameter, but significant deviations for the geometric width. Thomson et al. [58] recently performed LII particle sizing in a high-pressure diffusion flame. In that study, only *effective* particle sizes were determined. Kock et. al [61] measured particle-size distributions with a real two-parameter fit in a Diesel engine. TEM results of soot samples taken in the exhaust gas showed good agreement with the LII data. Unfortunately, this was only performed for one single measurement condition. At the first LII workshop in Duisburg 2005, the results from the determination of both the width and the mean diameter from sample data and self-measured signals in different flames show a significant variation of the geometric width of the distribution. The results from the χ^2-maps calculated in chapter 3.3.4 indicate that a simultaneous determination of the mean and the width of a log-normal particle-size distribution might result in difficulties since the minimum of the fit is not very well pronounced.

Therefore, the results in this work are the first detailed investigations on the ability of LII for measuring both the mean diameter and the width of a soot particle-size distribution in a flame – both at atmospheric and elevated pressure. Excellent agreement with TEM data was found for the obtained count median diameter for the Fuchs model with aggregates for all pressures. The width can not be obtained very accurately, as it is very sensitive to a variation in experimental input parameters. It should be noted that other models, assuming other physical input parameters, or maybe using simplified expressions, e.g. for the heat-capacity ratio γ, can obtain the same result for the *CMD* as in this study. In this work, it was tried to use the most accurate physical assumptions that are based on recent theoretical investigations [79,95]. Further research, both in modeling LII and experimental work, has to be done to clarify the correct experimental approach and data reduction and to determine the ability of LII for the measurement of particle-size distributions for a broad pressure range.

6 OUTLOOK

This work focused on theoretical and experimental work on laser-induced incandescence in sooting flames at elevated pressure. Though some open questions concerning particle sizing with LII at pressures up to 10 bar could be answered, some questions remain.

Experimental issues. The burner housing that was constructed in this work was laid out for operating pressures up to 30 bar. With the burner matrix made from sintered stainless steel, however, pressures up to 10 bar could be reached only because of the limited cooling of the burner surface. As practical combustors, e.g. Diesel engines, operate at higher pressures, the maximum pressure of 30 bar in the burner should be reached. A new type of flame holder, e.g. using the concept of the Universität Göttingen with alternating flat gold and corrugated aluminum foils, combined with a square plate with a round outlet, might give better results for higher pressures.

In this work, it has been shown that the effect of particle aggregation should be taken into account when primary particle sizes are deduced from LII decay curves. *In-situ* diagnostics with elastic light scattering can give more detailed insight in the aggregate structure at all pressures. This is preferred to intrusive TEM sampling measurements. Light scattering should be combined with LII measurements in order to quantify the effect of aggregates on LII in more detail.

Modeling results indicated that the gated LII signal, as used for the measurement of soot volume fractions, decreases with increasing pressure. Experimentally, by LII obtained soot volume fractions should be compared with an independent method, e.g. light extinction. Therefore, the burner windows must be modified, as etalon effects of a laser beam at the parallel surfaces of the windows complicate the extinction measurements. Either wedged windows must be used or the windows must be mounted in a tilted position in the flanges. Both solutions require a new design of the window flanges.

Modeling issues. The LII model, LIISim, that was developed in this thesis, must be further improved. The aggregate sub-model so far considers monodisperse aggregate sizes only. A polydisperse aggregate-size distribution should be taken into account in the model. The polydisperse distribution of the primary particle size is implemented as a numerical integral over the primary particles. This requires long calculation times, especially in the case of the Fuchs model. The calculation time can be significantly reduced if the log-normal size distribution is implemented as an analytical function.

So far, the model is based on soot. However, since LII is a suitable technique for the characterization of general nano-sized particles and future investigations plan to focus on the application of LII on these materials, LIISim should be modified to enable the modeling of these particles as well.

Other heat-loss mechanisms can be included, e.g. thermal annealing and photodesorption which are supposed to be imported at high laser fluences. The evaporation submodel should be studied again. The evaporation model is based on equilibrium thermodynamics which might describe the fast, nanosecond heat-up insufficiently. Additionally, incorrect values for the heat of vaporization of soot and the vapor pressure of soot should be replaced by more correct values.

7 SUMMARY

This work focussed on laser-induced incandescence (LII) at elevated pressure. LII is a laser-based technique for measuring particle sizes and volume fractions of nano-sized particles in aerosols. These particles, as emitted by traffic in the form of soot, cause a significant health risk. Nano-sized particles can penetrate deeply into the lungs and are considered important for causing asthma, fibrosis and the development of tumors [1,2]. LII has the potential as a non-intrusive diagnostic tool for measuring these ultrafine particles. Over the past 20 years, the main focus of LII has been on the development and application of LII for soot diagnostics in flames, though recent investigations studied non-carbon particles as well. Only little work has been performed on LII in sooting flames at elevated pressure. Nonetheless, this information is important for applications in practical high-pressure environments, e.g. Diesel engines and gas turbines, in order to understand the behavior and accuracy of LII under these conditions.

In order to quantify LII for soot diagnostics at elevated pressure, a stable, laminar sooting flame is required that can be operated at different pressures. It is challenging to stabilize sooting flames at elevated pressure, as these flames are very sensitive to fluctuations in the flow field. World wide, three other research groups have been setting up high-pressure sooting flames for LII in parallel to the work described in this thesis: Thomson and co-workers at the National Research Council (NRC) in Ottawa (diffusion flame, stable up to 40 bar) [120], McCrain and co-workers at North Carolina State University (diffusion flame, stable up to 25 bar), and the Deutsches Zentrum für Luft und Raumfahrt (DLR) in Stuttgart (premixed flame, stable up 5 bar). These groups have performed measurements of soot volume fractions [121,122] and effective particle sizes [58] with LII at variable pressure. However, no detailed investigations were performed on the determination of particle-size distributions with LII at elevated pressure. Therefore, this thesis focussed on this problem.

The work can be divided into three parts: First, a high-pressure burner was constructed and built in order to enable the experimental investigation of LII at elevated pressure. In a second, theoretical part, a state-of-the-art software program for modeling and fitting LII signals was developed. This is needed for the quantitative interpretation of experimental LII signals. Finally, LII experiments were performed in the newly developed high-pressure burner in sooting, premixed ethylene/air flames at pressures up to 10 bar. The data were evaluated with the model developed in the second part.

Construction of a sooting high-pressure burner. In order to investigate the ability of LII as a tool for soot diagnostics at elevated pressure, a sooting high-pressure burner was constructed in cooperation with the group of Prof. Dr. Dr. h.c. H. Gg. Wagner and Dr. H. Jander of the Universität Göttingen. They have long-term experience in the construction of sooting high-pressure burners. Improvements compared to previous burners were made in terms of larger optical access to the flame, automated control of the gas flows by mass-flow controllers, automated translation of the burner by a computer-controlled, 3-dimensional translation stage, a smaller burner housing, and a compact soot filter system. In contrast to the burners from Göttingen, the flame was chosen to be circular instead of rectangular. This caused some problems in constructing the flame holder. The concept of alternating flat gold and corrugated aluminum foils, which results in a rectangular flame holder with small (~15 μm) channels and a good heat conductivity, was not feasible. In the end, a round disc of sintered stainless steel was used as flame holder. The advantage of an axisymmetric flame over a rectangular flame is the simplification of potential modeling of the flow field in the burner. With the sintered stainless steel disc, the burner produced long-term stable, laminar ethylene/air flames up to 10 bar with pressure fluctuations less than ± 2%.

Modeling laser-induced incandescence. The LII signal results from a heat-up of particles by a nanosecond pulsed laser and subsequent cooling due to different heat-loss paths. In case of high laser fluences, evaporation of the particle is induced. This process can be modeled by setting up an energy and mass balance for the different heat- and mass-loss mechanisms. Recent advancements on the different sub-models were combined in the model, e.g., the influence of particle-size distributions, particle aggregation, and different heat-conduction sub-models often applied in literature. This model was implemented in a C-code, called LIISim, that enabled the modeling of LII signals as well as the fitting of experimental LII decay curves with a Levenberg-Marquardt non-linear least-squares fitting algorithm. LIISim allows to compare the influence of different physical parameters, e.g. pressure and temperature, on the LII signal. Moreover, LIISim provides the tools that are required for a detailed analysis of experimental LII signals. Additionally, a perl script was written which allows the access to the LII model over a web browser. For the first time, an LII model was made available to the scientific community by a web interface. The user can model LII signals for different conditions, e.g. different particle properties, heat conduction sub-models, and detection wavelengths. A data file with the calculation results can be downloaded. This will simplify the comparison of different LII models and reveal deficiencies in the underlying sub-models. LIISim is available at http://www.liisim.com.

Particle sizing with LII at variable pressure. In a first series of experiments, the log-normal particle-size distribution at 1 – 5 bar was measured using LII. The LII signal was detected at two different wavelengths, 550 and 694 nm, in order to determine the peak particle temperature after laser heat-up with two-color pyrometry. The gas-phase temperature was measured with multi-line NO-LIF thermometry. Both the peak particle temperature and the gas-phase temperature are required as input parameters for the LII model. The LII model is fitted to the experimentally acquired LII decay curves with the count median diameter (*CMD*) and the geometric width σ_g of the log-normal distribution as free fit parameters. However, the laser fluence might have been too high for a quantitative interpretation of the particle size in these experiments. At high laser fluences, soot fragments evaporate from the particle surface. The evaporation term in the LII model is related to some uncertainty, as detailed data on the vapor pressure and heat of formation of the evaporating carbon species are lacking.

In a second series of experiments, a detailed analysis of the ability of LII for measuring log-normal particle-size distributions at pressures of 1 – 10 bar was performed. Data were taken at 2 – 20 mm height above the burner for a flame at 1, 2, 5 and 10 bar respectively. The flame temperature was determined by two-color pyrometry of the non-laser-heated soot. Again, peak particle temperatures were measured with two-color LII at 550 and 694 nm. Low laser fluences of 70 – 115 mJ/cm^2 at 1064 nm were used to avoid evaporation. Peak particle temperatures remained below 3500 K which is well below the vaporization threshold of 3915 K at atmospheric pressure. C_2 fluorescence around the 550 nm detection channel might interfere with the LII signal. However, spectrally-resolved detection showed no narrow-band interferences in the region of 656 – 400 nm for the low laser fluences used in this study at all investigated pressures. One aim of this study was to identify differences in commonly used heat conduction models used in literature. LIISim includes these different sub-models and the experimental LII signals at 1 – 10 bar were evaluated with LIISim for different heat conduction sub-models. Significant differences between the applied models could be observed. In order to identify the correct model, soot samples were taken from two different locations in the flame for all pressures. Transmission-electron microscopy (TEM) images were taken from the samples and the frequency of particle size classes were counted in these images. From a statistic evaluation, the log-normal particle-size distribution could be reconstructed. For the first time, soot particle-size distributions obtained with LII could be compared with a second, independent method at elevated pressures. Moreover, a first comparison of different heat-conduction models applied to experimental LII signals could be performed. The results show excellent agreement between the *CMD* obtained by TEM analysis and LII for all pressures if the LII data are evaluated with the model of Fuchs (a general model for heat conduction of aerosols suggested in the 1960’s) taking into account the reduced heat conduction of aggregated particles. The peak particle temperature and the gas-phase temperature are required as input parameters for the LII data evaluation with LIISim. A variation of these parameters has only a minor effect on the determined *CMD* – an effect that is even decreasing with increasing pressure. However, the obtained geometric width is very sensitive to any variations in peak particle temperature or gas-phase temperature for all pressures. This might be in the nature the LII signal: The information that is available from a single, monotonic signal decay is limited and probably only sufficient to determine one parameter. It should be noted that these results are the first detailed investigations on the ability of LII for measuring both the mean diameter and the width of a soot particle-size distribution in a flame by a two-parameter fit – both at atmospheric and elevated pressure.

Hence, it could be shown that LII is a robust method to determine the count median diameter of a log-normal soot particle-size distribution for pressures up to 10 bar as long as the correct model for data evaluation is used. The Fuchs model taking into account the reduced heat conduction of aggregated particles could be identified as the most correct model. This work significantly advanced the understanding of LII at high pressures which further improves the applicability of this diagnostics technique to *in-situ* particle-size measurements in practical combustion apparatuses.

8 REFERENCES

1. J. Ferin, G. Oberdörster, D. P. Penney, S. C. Soderholm, R. Gelein, and H. C. Piper, "Increased pulmonary toxicity of ultrafine particles? I. particle clearance, translocation, morphology," J. Aerosol Sci. **21**, 381-384 (1990).
2. G. Oberdörster, J. Ferin, G. Finkelstein, P. Wade, and N. Corson, "Increased pulmonary toxicity of ultrafine particles? II. Lung lavage studies," J. Aerosol Sci. **21**, 384-387 (1990).
3. International Energy Agency, *http://www.iea.org*. 2003.
4. P. McKendry, "Energy production from biomass (part 1): overview of biomass," Bioresource Technology **83**, 37-46 (2002).
5. P. McKendry, "Energy production from biomass (part 2): conversion technologies," Bioresource Technology **83**, 47-54 (2002).
6. P. McKendry, "Energy production from biomass (part 3): gasification technologies," Bioresource Technology **83**, 55-63 (2002).
7. A. C. Eckbreth, *Laser diagnostics for combustion temperature and species*, 2 ed (Gordon and Breach, Amsterdam, 1996).
8. K. Kohse-Höinghaus and J. B. Jeffries, eds. *Applied Combustion Diagnostics* (Taylor and Francis, New York, 2002).
9. J. Wolfrum, "Lasers in combustion: From basic theory to practical devices," Proc. Combust. Inst. **27**, 1-42 (1998).
10. B. F. Kock, C. Kayan, J. Knipping, H. R. Orthner, and P. Roth, "Comparison of LII and TEM sizing during synthesis of iron particle chains," Proc. Combust. Inst. **30**, 1689-1697 (2005).
11. T. Lehre, R. Suntz, and H. Bockhorn, "Time-resolved two-color LII: size distributions of nano-particles from gas-to-particle synthesis," Proc. Combust. Inst. **30**, 2585-2593 (2005).
12. R. L. Vander Wal, T. M. Ticich, and J. R. West, Jr., "Laser-induced incandescence applied to metal nanostructures," Appl. Opt. **38**, 5867-5879 (1999).
13. C. Schulz, B. F. Kock, M. Hofmann, H. Michelsen, S. Will, B. Bougie, R. Suntz, and G. Smallwood, "Laser-induced incandescence: recent trends and current questions," Appl. Phys. B **83**, 333 (2006).
14. M. Hofmann, W. G. Bessler, C. Schulz, and H. Jander, "Laser-induced incandescence (LII) for soot diagnostics at high pressure," Appl. Opt. **42**, 2052-2062 (2003).
15. R. W. Weeks and W. W. Duley, "Aerosol-particle sizes from light emission during excitation by TEA CO_2 laser pulses," J. Appl. Phys **45**, 4661-4662 (1973).
16. A. C. Eckbreth, "Effects of laser-modulated particle incandescence on Raman scattering diagnostics," J. Appl. Phys. **48**, 4473-4479 (1977).

17. L. A. Melton, "Soot diagnostics based on laser heating," Appl. Opt. **23**, 2201-2208 (1984).

18. C. J. Dasch, "Continuous-wave probe laser investigation of laser vaporization of small particles in a flame," Appl. Opt. **23**, 2209-2215 (1984).

19. C. J. Dasch, "New soot diagnostics in flames based on laser vaporization of soot," Proc. Combust. Inst. **20**, 1231-1237 (1984).

20. T. Ni, J. A. Pinson, S. Gupta, and R. J. Santoro, "Two-dimensional imaging of soot volume fraction by the use of laser-induced incandescence," Appl. Opt. **34**, 7083-7091 (1995).

21. D. J. Bryce, N. Ladommatos, and H. Zhao, "Quantitative investigation of soot distribution by laser-induced incandescence," Appl. Opt. **39**, 5012-5022 (2000).

22. C. R. Shaddix and K. C. Smyth, "Laser-Induced Incandescence Measurements of Soot Production in Steady and Flickering Methane, Propane, and Ethylene Diffusion Flames," Combust. Flame **107**, 418-452 (1996).

23. P. O. Witze, S. Hochgreb, D. Kayes, H. A. Michelsen, and C. R. Shaddix, "Time-resolved laser-induced incandescence and laser elastic-scattering measurements in a propane diffusion flame," Appl. Opt. **40**, 2443-2452 (2001).

24. B. Quay, T.-W. Lee, T. Ni, and R. J. Santoro, "Spatially resolved measurements of soot volume fraction using laser-induced incandescence," Combust. Flame **97**, 384-392 (1994).

25. R. L. Vander Wal, "Laser-induced incandescence: Development and characterization towards a measurement of soot-volume fraction," Appl. Phys. B **59**, 445-452 (1994).

26. J. Appel, B. Jungfleisch, M. Marquardt, R. Suntz, and H. Bockhorn, "Assessment of soot volume fractions from laser-induced incandescence by comparison with extinction measurements in laminar, premixed, flat flames," Proc. Combust. Inst. **26**, 2387-2395 (1996).

27. B. Axelsson, R. Collin, and P.-E. Bengtsson, "Laser-induced incandescence for soot particle size measurements in premixed flat flames," Appl. Opt. **39**, 3683-3690 (2000).

28. B. Axelsson, R. Collin, and P.-E. Bengtsson, "Laser-induced incandescence for soot particle size and volume fraction measurements using on-line extinction calibration," Appl. Phys. B **72**, 367-372 (2001).

29. H. Geitlinger, T. Streibel, R. Suntz, and H. Bockhorn, "Two-dimensional imaging of soot volume fractions; particle number densities; and particle radii in laminar and turbulent diffusion flames," Proc. Combust. Inst. **27**, 1613-1621 (1998).

30. T. R. Meyer, S. Roy, V. M. Belovich, E. Corporan, and J. R. Gord, "Simultaneous planar laser-induced incandescence, OH planar laser-induced fluorescence, and droplet Mie scattering in swirl-stabilized spray flames," Appl. Opt. **44**, 445-454 (2005).

31. H. Bockhorn, H. Geitlinger, B. Jungfleisch, T. Lehre, A. Schön, T. Streibel, and R. Suntz, "Progress in characterization of soor formation by optical methods," Phys. Chem. Chem. Phys. **4**, 3780-3793 (2002).

32. S. Will, S. Schraml, and A. Leipertz, "Comprehensive two-dimensional soot diagnostics based on laser-induced incandescence," Proc. Combust. Inst. **26**, 2277-2284 (1996).

33. S. Will, S. Schraml, K. Bader, and A. Leipertz, "Performance characteristics of soot primary particle size measurements by time-resolved laser-induced incandescence," Appl. Opt. **37**, 5647-5658 (1998).

34. T. Lehre, B. Jungfleisch, R. Suntz, and H. Bockhorn, "Size distributions of nanoscaled particles and gas temperatures from time-resolved laser-induced-incandescence measurements," Appl. Opt. **42**, 2021-2030 (2003).

35. D. Woiki, A. Giesen, and P. Roth, "Time-resolved laser-induced incandescence for soot particle sizing during acetylene pyrolysis behind shock waves," Proc. Combust. Inst. **28**, 2531-2537 (2000).

36. R. L. Vander Wal, T. M. Ticich, and A. B. Stephens, "Can soot primary particle size be determined using laser-induced incandescence?" Combust. Flame **116**, 291-296 (1999).

37. B. F. Kock, T. Eckhardt, and P. Roth, "In-cylinder sizing of Diesel particles by time-

resolved laser-induced incandescence (TR-LII)," Proc. Combust. Inst. **29**, 2775-2781 (2002).

38. D. R. Snelling, G. J. Smallwood, R. A. Sawchuk, W. S. Neill, D. Gareau, D. J. Clavel, W. L. Chippior, F. Liu, and Ö. L. Gülder, "In-situ real-time characterization of particulate emissions from a Diesel engine exhaust by laser-induced incandescence," SAE Technical Paper Series No. 2000-01-1994 (2000).

39. S. Schraml, S. Will, and A. Leipertz, "Performance characteristics of TIRE-LII soot diagnostics in exhaust gases of Diesel engines," SAE Technical Paper Series No. 2000-01-2002 (2000).

40. N. P. Tait and D. A. Greenhalgh, "PLIF imaging of fuel fraction in practical devices and LII imaging of soot," Ber. Bunsenges. Phys. Chem. **97**, 1619. (1993).

41. R. L. Vander Wal, K. A. Jensen, and M. Y. Choi, "Simultaneous Laser-Induced Emission of Soot and Polycyclic Aromatic Hydrocarbons Within a Gas-Jet Diffusion Flame," Combust. Flame **109**, 399-414 (1997).

42. R. L. Vander Wal, "LIF-LII measurements in a turbulent gas-jet flame," Exp. Fluids **23**, 281-287 (1997).

43. R. L. Vander Wal, "Laser-induced incandescence: Detection issues," Appl. Opt. **35**, 6548-6559 (1996).

44. R. L. Vander Wal and K. A. Jensen, "Laser-induced incandescence: Excitation intensity," Appl. Opt. **37**, 1607-1616 (1998).

45. R. T. Wainner, J. M. Seitzman, and S. R. Martin, "Quantitative limitations of laser-induced incandescence in practical combustion environments," AIAA paper 98-0398 (1998).

46. K. C. Smyth and C. R. Shaddix, "The elusive History of m = 1.57 - 0.56i for the Refractive Index of Soot," Combust. Flame **107**, 314-320 (1996).

47. D. R. Snelling, G. J. Smallwood, F. Liu, Ö. L. Gülder, and W. D. Bachalo, "A Calibration-Independent LII Technique for Soot Measurement by Detecting Abolute Light Intensity," Appl. Opt. **44**, 6773-6785 (2005).

48. A. E. Greis, G. Grünefeld, M. Becker, and S. Pischinger, "Quantitative measurements of the soot distribution in a realistic common rail D.I. Diesel engine," in *11th International Symposium on Application of Laser Techniques to Fluid Mechanics* (Lissabon, 2002).

49. D. Choi, M. Iwamuro, Y. Shima, J. Senda, and H. Fujimoto, "The effect of fuel-vapor concentration on the process of initial combustion and soot formation in a DI Diesel engine using LII and LIEF," SAE Technical Paper Series No. 2001-01-1255 (2001).

50. G. Bruneaux, D. Verhoeven, and T. Baritaud, "High-pressure Diesel spray and combustion visualization in a transparent model Diesel engine," SAE Technical Paper Series No. 1999-01-3648 (1999).

51. K. Inagaki, S. Takasu, and K. Nakakita, "In-cylinder quantitative soot concentration measurements by laser-induced incandescence," SAE Technical Paper Series No. 1999-01-0508 (1999).

52. J. A. Pinson, D. L. Mitchell, R. J. Santoro, and T. A. Litzinger, "Quantitative; planar soot measurements in a D.I. Diesel engine using laser-induced incandescence and light scattering," SAE Technical Paper Series No. 932650 (1993).

53. G. Wiltafsky, W. Stolz, J. Köhler, and C. Espey, "The quantification of laser-induced incandescence (LII) for planar time resolved measurements of the soot volume fraction in a combustion Diesel jet," SAE Technical Paper Series No. 961200 (1996).

54. D. L. Hofeldt, "Real-time soot concentration measurement technique for engine exhaust streams," SAE Technical Paper Series No. 930079 (1993).

55. S. Will, S. Schraml, and A. Leipertz, "Two-dimensional soot-particle sizing by time-resolved laser-induced incandescence," Opt. Lett. **20**, 2342-2344 (1995).

56. P. Roth and A. V. Filippov, "In situ ultrafine particle sizing by a combination of pulsed laser heatup and particle thermal emission," J. Aerosol Sci. **27**, 95-104 (1996).

57. A. Boiarciuc, F. Foucher, and C. Mounaïm-Rousselle, "Soot volume fractions and primary particle size estimate by means of the simultaneous two-color-time-resolved and 2D laser-induced incandescence," Appl. Phys. B **83**, 413 (2006).

58. K. A. Thomson, D. R. Snelling, G. J. Smallwood, and F. Liu, "Laser induced incandescence measurements of soot volume fraction and effective particle size in a laminar co-annular non-premixed methane/air flame at pressures between 0.5-4.0 MPa," Appl. Phys. B **83**, 469 (2006).

59. R. Starke and P. Roth, "Soot particle sizing by LII during shock tube pyrolysis of C_6H_6," Combust. Flame **127**, 2278-2285 (2002).

60. R. Starke, B. F. Kock, and P. Roth, "Nano-particle sizing by laser-induced-incandescence (LII) in a shock wave reactor," Shock Waves **12**, 351-360 (2003).

61. B. F. Kock and P. Roth, "Two-color TR-LII applied to in-cylinder Diesel particle sizing," in *Proc. of the European Combustion Meeting* (Orléans, 2003).

62. T. P. Jenkins and R. K. Hanson, "Soot Pyrometry using Modulated Absorption/Emission," Combust. Flame **126**, 1669-1679 (2001).

63. K. Omerbegovic, H. Kronemayer, M. Hofmann, and C. Schulz, "Vergleich von Ruß- und Gasphasentemperatur in Ethylen/Luft-Flammen," in *VDI Flammentag* (2005).

64. C. Brackmann, J. Bood, P.-E. Bengtsson, T. Seeger, M. Schenk, and A. Leipertz, "Simultaneous vibrational and pure rotational coherent anti-Stokes Raman spectroscopy for temperature and multispecies concentration measurements demonstrated in sooting flames," Appl. Opt. **41**, 564-572 (2002).

65. K. P. Geigle, Y. Schneider-Kühnle, M. S. Tsurikov, R. Hadef, R. Lückerath, V. Krüger, W. Stricker, and M. Aigner, "Investigation of laminar pressurized flames for soot model validation using SV-CARS and LII," Proc. Combust. Inst. **30**, 1645-1653 (2005).

66. J. Nygren, J. Engström, J. Walewski, C. F. Kaminski, and M. Aldén, "Applications and evaluation of two-line atomic LIF thermometry in sooting combustion environments," Meas. Sci. Technol. **12**, 1291-1303 (2001).

67. W. G. Bessler and C. Schulz, "Quantitative multi-line NO-LIF temperature imaging," Appl. Phys. B **78**, 519-533 (2004).

68. M. Hofmann, H. Kronemayer, B. F. Kock, H. Jander, and C. Schulz, "Laser-induced incandescence and multi-line NO-LIF thermometry for soot diagnostics at high pressures," in *Proc. of the European Combustion Meeting* (Louvain-la-Neuve, 2005).

69. S. De Iuliis, F. Cignoli, and G. Zizak, "Two-color laser-induced incandescence (2C-LII) technique for absolute soot volume fraction measurements in flames," Appl. Opt. **44**, 7414-7423 (2005).

70. S. De Iuliis, F. Migliorini, F. Cignoli, and G. Zizak, "Peak soot temperature in laser-induced incandescence measurements," Appl. Phys. B **83**, 397 (2006).

71. D. R. Snelling, F. Liu, G. J. Smallwood, and Ö. L. Gülder, "Determination of the soot absorption function and thermal accomodation coefficient using low-fluence LII in a laminar coflow ethylene diffusion flame," Combust. Flame **136**, 180-190 (2004).

72. D. R. Snelling, F. Liu, G. J. Smallwood, and Ö. L. Gülder, "Evaluation of the nanoscale heat and mass transfer model of LII: Prediction of the excitation intensity," in *34th National Heat Transfer Conference* (Pittsburgh, 2000).

73. H. Bladh and P.-E. Bengtsson, "Characteristics of laser-induced incandescence from soot in studies of a time-dependent heat and mass-transfer model," Appl. Phys. B **78**, 241-248 (2004).

74. B. Mewes and J. M. Seitzman, "Soot volume fraction and particle size measurements with laser-induced incandescence," Appl. Opt. **36**, 709-717 (1997).

75. H. A. Michelsen, "Understanding and predicting the temporal response of laser-induced incandescence from carbonaceous particles," J. Chem. Phys. **118**, 7012-7045 (2003).

76. C. F. Bohren and D. R. Huffman, *Absorption and Scattering of Light by Small Particles* (Wiley, New York, 1983).

77. M. Kerker, *The Scattering of Light and other Electromagnetic Radiation* (Academic, New York, 1969).

78. H. Chang and T. T. Charalampopoulos, "Determination of the wavelength dependence of refractive indices of flame soot," Proc. R. Soc. Lond. A **430**, 577-591 (1990).

79. F. Liu, K. J. Daun, D. R. Snelling, and G. J. Smallwood, "Heat conduction from a spherical nano-particle: status of modeling heat conduction in laser-induced incandescence," Appl. Phys. B **83**, 355 (2006).

80. A. V. Filippov and D. E. Rosner, "Energy transfer between an aerosol particle and gas at high temperature ratios in the Knudsen transition regime," Int. J. Heat and Mass Transfer **43**, 127-138 (2000).

81. M. Knudsen, "Die molekulare Wärmeleitung der Gase und der Akkomodationskoeffizient," Annalen der Physik **34**, 593-657 (1911).

82. A. V. Eremin, E. V. Gurentsov, M. Hofmann, B. F. Kock, and C. Schulz, "TR-LII for sizing of carbon particles forming at room temperature," Appl. Phys. B **83**, 449 (2006).

83. B. J. McCoy and C. Y. Cha, "Transport phenomena in the rarefied gas transition regime," Chem. Eng. Science **29**, 381-388 (1974).

84. S. Chapman and T. G. Cowlings, *Mathematical Theory of Non-Uniform Gases* (Cambridge U.P., London, 1970).

85. N. A. Fuchs, "On the stationary charge distribution on aerosol particles in a bipolar ionic atmosphere," Geophys. Pura Appl. **56**, 185-193 (1963).

86. N. A. Fuchs, *The Mechanics of Aerosols* (Pergamon Press, Oxford, 1964 (Dover Publications, New York, 1989)).

87. H. R. Leider, O. H. Krikorian, and D. A. Young, "Thermodynamic properties of carbon up to the critical point," Carbon **11**, 555-563 (1973).

88. G. J. Smallwood, D. R. Snelling, F. Liu, and Ö. L. Gülder, "Clouds over Soot Evaporation: Errors in Modeling Laser-Induced Incandescence of Soot," J. Heat Transfer **123**, 814-818 (2001).

89. T. Heidermann, H. H. Jander, and H. G. Wagner, "Soot particles in premixed C_2H_4-air-flames at high pressures (P=30-70 bar)," Phys. Chem. Chem. Phys. **1**, 3497-3502 (1999).

90. C. M. Megaridis and R. A. Dobbins, Combust. Sci. Tech. **71**, 95 (1990).

91. R. Puri, R. T.F., R. J. Santoro, and R. A. Dobbins, "Aerosol Dynamic Processes of Soot Aggregates in a Laminar Ethyne Diffusion Flame," Comb. and Flame **92**, 320-333 (1993).

92. Ü. Ö. Köylü, K. C. Xing, and D. E. Rosner, Langmuir **11**, 4848 (1995).

93. S. S. Krishnan, K. C. Lin, and G. M. Faeth, J. Heat Transfer **122**, 517 (2000).

94. S. R. Forrest and T. A. Witten, J. Phys. A **12**, L109 (1979).

95. F. Liu, M. Yang, F. A. Hill, D. R. Snelling, and G. J. Smallwood, "Influence of polydisperse distributions of both primary particle and aggregate size on soot temperature in low-fluence LII," Appl. Phys. B **83**, 383 (2006).

96. F. Liu, G. J. Smallwood, and D. R. Snelling, "Effects of primary particle diameter and aggregate size distribution on the temperature of soot particles heated by pulsed lasers," J. Quant. Spectros. Radiat. Transfer **93**, 301-312 (2005).

97. Ü. Ö. Köylü and G. M. Faeth, "Optical properties of soot in buoyant laminar diffusion flames," J. Heat Transfer **116**, 971-979 (1994).

98. G. M. Faeth and Ü. Ö. Köylü, "Soot morphology and optical properties in nonpremixed

turbulent flame environments," Combust. Sci. Tech. **108**, 207-229 (1995).

99. A. V. Filippov, M. Zurita, and D. E. Rosner, "Fractal-like Aggregates: Relation between Morphology and Physical properties," J. Colloid Interface Sci. **229**, 261-273 (2000).

100. V. Beyer and D. A. Greenhalgh, "Laser induced incandescence under high vacuum conditions," Applied Physics B: Lasers and Optics **83**, 455 (2006).

101. W. H. Press, W. T. Vettering, S. A. Teukolsky, and B. P. Flannery, *Numerical Recipes in C: The art of scientific computing*, 2 ed (Cambridge University Press, New York, 1992).

102. J. Navia, *lcc-win32: A compiler system for windows.*

103. W. G. Bessler, C. Schulz, V. Sick, and J. W. Daily, "A versatile modeling tool for nitric oxide LIF spectra," in *3rd Joint meeting of the US sections of the combustion institute* (Chicago, 2003), PI1-6.

104. G. D. Yoder, P. K. Diwakar, and D. W. Hahn, "Assessment of soot particle vaporization effects during laser-induced incandescence with time-resolved light scattering," Appl. Opt. **44**, 4211-4219 (2005).

105. R. L. Vander Wal and T. M. Ticich, "Cavity ringdown and laser-induced incandescence measurements of soot," Appl. Opt. **38**, 1444-1451 (1999).

106. H. Böhm, C. Feldermann, T. Heidermann, H. Jander, B. Lüers, and H. G. Wagner, "Soot formation in premixed C_2H_4-air flames for pressures up to 100 bar," Proc. Combust. Inst. **24**, 991-998 (1992).

107. S. Hanisch, H. Jander, T. Pape, and H. G. Wagner, "Soot mass growth and coagulation of soot particles in C_2H_4/air-flames at 15 bar," Proc. Combust. Inst. **25**, 577-584 (1994).

108. H. Böhm, D. Hesse, H. Jander, B. Lüers, J. Pietscher, H. G. Wagner, and M. Weiss, "The influence of pressure and temperature on soot formation in premixed flames," Proc. Combust. Inst **22**, 403-411 (1988).

109. M. Bönig, C. Feldermann, H. Jander, B. Lüers, G. Rudolph, and H. G. Wagner, "Soot formation in premixed C_2H_4 flat flames at elevated pressure," Proc. Combust. Inst **23**, 1581-1587 (1990).

110. H. Mätzing and H. G. Wagner, "Measurements about the influence of pressure on carbon formation in premixed laminar C_2H_4-air flames," Proc. Combust. Inst. **21**, 1047-1055 (1986).

111. E. A. Rohlfing, "Optical emission studies of atomic, molecular, and particulate carbon produced from a laser vaporization cluster source," J. Chem. Phys. **89**, 6103-6112 (1988).

112. C. B. Stipe, J. H. Choi, D. Lucas, C. P. Koshland, and R. F. Sawyer, J. Nanopart. Res. **6**, 467 (2004).

113. F. K. Kneubühl and M. W. Sigrist, *Laser*, 4th ed (Teubner Verlag, Stuttgart, 1995).

114. B. F. Kock, *Zeitaufgelöste Laserinduzierte Inkandeszenz (TR-LII): Partikelgrößenmessung in einem Dieselmotor und einem Gasphasenreaktor*, in *IVG*. 2005, Universität Duisburg-Essen: Duisburg.

115. A. O. Vyrodow, J. Heinze, M. Dillmann, U. E. Meier, and W. Stricker, "Laser-induced fluorescence thermometry and concentration measurements on NO A-X (0,0) transitions in the exhaust gas of high pressure CH_4/air flames," Appl. Phys. B. **61**, 409-414 (1995).

116. W. G. Bessler, C. Schulz, T. Lee, D. I. Shin, M. Hofmann, J. B. Jeffries, J. Wolfrum, and R. K. Hanson, "Quantitative NO-LIF imaging in high-pressure flames," Appl. Phys. B **75**, 97-102 (2002).

117. H. Zhao and N. Ladommatos, "Optical diagnostics for soot and temperature measurements in Diesel engines," Prog. Energy Combust. Sci. **24**, 221-255 (1998).

118. T. Schittkowski, B. Mewes, and D. Brüggemann, "Laser-induced incandescence and Raman measurements in sooting methane and ethylene flames," Phys. Chem. Chem. Phys. **4**, 2063-2071 (2002).

119. S. Dankers and A. Leipertz, "Determination of primary particle size distributions from time-resolved laser-induced incandescence measurements," Appl. Opt. **43**, 3726-3731 (2004).

120. K. A. Thomson, Ö. L. Gülder, E. J. Weckman, R. A. Fraser, G. J. Smallwood, and D. R. Snelling, "Soot concentration and temperature measurements in co-annular, nonpremixed CH_4/air laminar flames at pressures up to 4 MPa," Combust. Flame **140**, 222-232 (2005).

121. L. L. McCrain and W. L. Roberts, "Measurements of the soot volume field in laminar diffusion flames at elevated pressures," Combust. Flame **140**, 60-69 (2005).

122. M. S. Tsurikov, K. P. Geigle, V. Krüger, Y. Schneider-Kühnle, W. Stricker, R. Lückerath, R. Hadef, and M. Aigner, "Laser-based investigations of soot formation in laminar premixed flames at atmospheric and elevated pressures," Combust. Sci. Tech. **177**, 1835-1862 (2005).

APPENDIX: LIISIM

LIISim is a software tool for modeling LII signals as well as for fitting experimental LII data. The program solves the energy and mass balance for the heating of nano-sized particles by a pulsed laser and subsequent cooling by heat conduction, evaporation and radiation. The model is set up for soot only though a modification to general particle materials will be possible in future. The description in the following sections is for the current version 1.35 of LIISim. A web interface for the modeling part is available at http://www.liisim.com.

A1 Data input

LIISim is written in standard C. The structure of the source code is related to LIF-Sim and is built up in a modular way. The modules, each of which is programmed for a certain task, are called by the main function. The core of the program is the function that numerically solves the differential equation of the energy and mass balance. This is required for the following tasks of LIISim:

1. Model LII signals for a given set of start parameters
2. Model the gated LII signal in dependence on a variable parameter
3. Fit experimental LII signals
4. Calculate a "χ^2-map", i.e. generate a two-dimensional map of the maximum likelihood estimator χ^2 for a given signal in dependence on two variable parameters.

LIISim is started from the command line (e.g. a DOS shell) with the command "liisim". All variable input parameters are given to the program in the form of ASCII files. These are the following files:

lii_start.dat. This is the main input file. The general choice of what LIISim should do is set here as well as the initial values of the model, e.g. the gas temperature, particle diameter and laser fluence. The heat-conduction model that should be used can be chosen and the time step and duration of the numerical integration can be set. An example of some lines of *lii_start.dat* are shown in Figure A1.

```
**********************************************************
* What do you want to do? Choose of the following options:
**********************************************************

* Model LII signal?
1 * 0=no, 1=yes
*
* Model Parameter Variation?
0 * 0=no, 1=yes (if yes, set your variation parameters in lii_variation.dat)
*
* Fit data?
0 * 0=no, 1=yes (if yes, set your fit parameters in lii_fit.dat)
*
* Calculate Chisquare map?
0 * 0=no, 1=yes
*
* Evaluation Max?
0 * 0=no, 1=yes
*
* Log-normal primary particle-size distribution?
0 * 0=no, 1=yes
```

Figure A1. First part of the input file lii_start.dat.

The choice between the different tasks is made by setting a ‘0’ or a ‘1’ after the corresponding question. All lines starting with a ‘*’ are command lines. The different values can be separated by spaces, tabulators or carriage returns. For instance, the settings in Figure A1 are equivalent to ‘1 0 0 0 0 0’. The file *lii_start.dat* is the input file that is modified most often compared to other input files.

lii_absorption.dat. These are the absorption parameters. Default settings are a wavelength of 1064 nm and an *E(m)* of 0.4. If an experimental, temporal laser profile is provided, the normalization constant must be set here.

lii_detection.dat. The detection bandpass, *E(m)* (usually the same as in the file *lii_absorption.dat*) and the detection gate are set here.

lii_evaporation.dat. This file contains the coefficients for the polynomial expressions of the temperature dependence of the heat of vaporization of graphite, the molar mass of the evaporating carbon fragments, the molecular cross section of the graphite vapor and the vapor pressure of graphite.

lii_heatconduction.dat. Different settings for the heat conduction. The value for the number of primary particles per aggregate is set here as well.

lii_internal.dat. Settings for the internal energy: Particle density, coefficients for the temperature dependence of the heat capacity of the particle as well as the molar mass of the particle.

lii_variation.dat. Settings for modeling gated LII signals vs. a variable parameter. This variable parameter can be the laser fluence, the particle diameter, the particle number density or the gas pressure.

lii_fit.dat. The fitting parameters are set here. First, the path and file name of the experimental LII signals for both detection wavelengths of the two-color LII experiment have to be set. The input files should consist of two columns – the first column provides the time in seconds of the experimental signal, the second column the LII signal in arbitrary units. The first line, usually a header line with the column labels, is ignored. The decimal separator of the data must be a '.'. The columns must be separated by a space or a tab stop. If an experimentally obtained standard deviation is used in equation 3.3, the option "Experimental standard deviation" should be set to '1' and the experimental input file should contain a third column with the experimental standard deviation for each data point. The calibration factor for two-color LII is the factor $K_2(\lambda_2)/K_1(\lambda_1)$ in equation 2.3. At the end of the file, it can be chosen which parameter(s) should be fitted. The start value, an upper and lower boundary can be set for each fitting parameter.

The last part is also used for the calculations of the χ^2-maps: If in *lii_start.dat* the option "Calculate Chisquare map" is selected, the start value of the fit parameter in *lii_fit.dat* is the stepsize of the variation of that parameter. The lower and upper boundary are the start and end value of that parameter respectively. For instance, if the option "Calculate Chisquare map" is selected, the following settings in *lii_fit.dat*

```
* value        variation      lower boundary   upper boundary
1800           0              1000                 3000    *Gas temperature, K
0.04           1              25                   35      *Primary particle diameter/CMD, nm
0.3            0              0.01                 1       *Thermal accomodation coefficient
0.0            0              0                    1       *Laser fluence, J/cm^2
60             0              30                   120     *temporal peak of laser pulse, ns
100            0              2                    1000    *Nr. of primary particles/aggregate
3400           0              1000                 5000    *Start particle temperature, K
8E-4           1              1.1                  1.3     *Geometric standard deviation of
*lognormal particle size distribution. Must be >1
```

will result in the generation of a χ^2-map with the *CMD* and σ_g as variables. The *CMD* is varied from 25 to 35 nm in steps of 0.04 nm, σ_g is varied from 1.1 to 1.3 in steps of 0.0008. In this way, Figure 3.13 was created. Note that the settings of the values in *lii_fit.dat*, e.g. the value of the gas temperature or the accommodation coefficient, will override the initial settings in *lii_start.dat* if the fitting option or the χ^2-maps option at the beginning of *lii_start.dat* is chosen. This is the case for all parameters at the end of *lii_fit.dat*, i.e. even if 'variation' is set to '0' for a given parameter.

LaserTempProfile.dat. This file provides an experimental, temporal laser profile. It should consist of two columns – the first column provides the time in seconds, the second column the laser intensity in arbitrary units. The decimal separator of the data must be a '.'. The columns must be separated by a space or a tabulator. The normalization constant must be set in the file *lii_absorption.dat*. The time spacing can be arbitrary and does not have to match the stepsize of the numerical integration routine.

A3 Source code

The source code is contained in several text files:

lii.c. This file contains the main function file. In the function `main(void)`, the start parameters are read and the selection is made which module should be called following the choice the user has made in the data input file. The two functions for solving the energy and mass balance for monodisperse and polydisperse particle sizes respectively are included in *lii.c* as well. Additional functions are called in here which are located in the other source files.

lii_energy_balance.c. The expressions for the different sub-models of the energy and mass balance are located in this file. Additional functions that are required for the calculations of the sub-model terms are located at the end of the file.

lii-fit.c. Here are the functions for the fitting routine. There are two separated functions for the fitting of the LII signal decay and the fitting of the entire LII signal respectively. The functions read the experimental signal, prepare it for fitting and finally perform the fit. The function for calculating the χ^2-maps are included in this file as well.

lii-numeric.c. All numerical algorithms that are required for the model are located here. These functions were taken from the book *Numerical recipes in C*.

lii_max.c. This is an individual data evaluation part. It can be used to fit multiple experimental data sets successively.

lii-io.c. This file contains basic input/output functions to read ASCII files, e.g. the input files.

lif.h. Header file, contains functions and structure definitions. All variables of the energy and mass balance are stored in structure variables. Each heat-loss mechanism with its specific variables has its own structure, e.g. the structure `struct HeatConductionParams` contains the variables of the heat-conduction term. Other groups have their own structure as well, e.g. the fit parameters and the start parameters.

In Figure A2 a schematic overview on the source code is shown. The most important functions in the different source files are given. Each function is drawn as a rectangle with the function name on top of it. Three dots in the parameter list indicate that one or more parameters are passed to the function, e.g. derives(…). A short description of the task of the function is given below the function name. Other functions, that are called within the function, are listed inside the rectangle. If a function is called several times, i.e. it is a loop, the function name is enclosed in an rectangular arrow. Note that not all functions are listed, but only the major functions that are important to understand the connections between the different source code files.

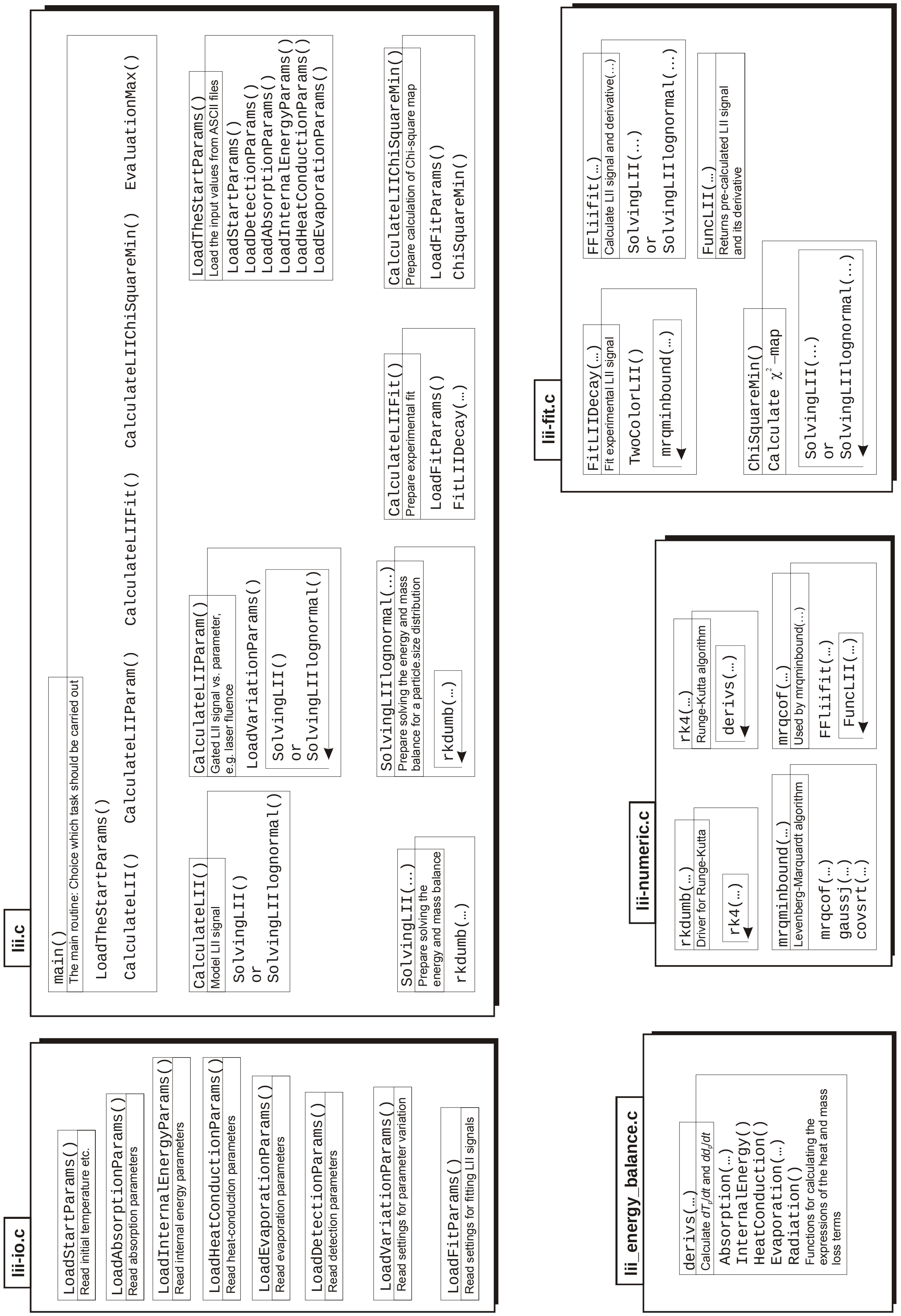

Figure A3. Graphical overview on the most important functions in LIISim and their location in the different source files.

A3 The web interface

A web interface was programmed to access the modeling part of LIISim. This is based on a CGI script written in perl. The script is located in the home directory of the user “hermanns” on the server www.vug.uni-duisburg.de. A button called “Model LII signals” on the start web-site http://liisim.com can be clicked which calls the perl script named *liisim_vug.pl*. This is done with the HTML tag `<form>`:

```
<form method="POST" action="/~hermanns/liisim/liisim_vug.pl">
```

A form with the default input values for LIISim is generated by the perl script. The form contains a so called “hidden field” that indicates whether the form has already been filled out or not. The form is checked for correct entries and, if the entries are correct, the ASCII input files for LIISim are created and the LIISim executable is called. Each output file of the LIISim calculation is renamed into a unique file name that contains the run time of the server in seconds. In this way, each user of the web interface has his own unique data file and a multiple user operation is enabled. To avoid an accumulation of output files over time, all files older than 10 minutes are deleted before LIISim is executed. These are Linux/Unix specific commands and, hence, the script can be executed under these operating systems only. However, a change to general operating systems can be made in future. The program Gnuplot creates a png-graph of the data file which is included in the HTML page that is sent back to the user. An example of the liisim directory with the rights for reading, writing and execution is shown in Figure A3.

```
hermanns@www:~/public_html/liisim> ls -l
total 656
-rw-r--r--    1 hermanns users       13321 2006-06-22 18:10 LaserTempProfile.dat
-rw-r--r--    1 hermanns users      495455 2006-09-25 21:36 download_liidatafile_159212975.dat
-rw-r--r--    1 hermanns users        3598 2006-09-25 21:36 download_liigraph_159212975.png
-rw-r--r--    1 hermanns users         199 2006-09-25 21:36 gnuplotinput.gnu
-rw-r--r--    1 hermanns users          81 2006-09-25 21:36 lii_absorption.dat
-rw-r--r--    1 hermanns users          79 2006-09-25 21:36 lii_detection.dat
-rw-r--r--    1 hermanns users         291 2006-09-25 21:36 lii_evaporation.dat
-rw-r--r--    1 hermanns users         114 2006-09-25 21:36 lii_heatconduction.dat
-rw-r--r--    1 hermanns users          91 2006-09-25 21:36 lii_internal.dat
-rw-r--r--    1 hermanns users         113 2006-09-25 21:36 lii_start.dat
-rwxr-xr-x    1 hermanns users       85128 2006-07-23 23:09 liisim
-rw-r--r--    1 hermanns users         836 2006-09-25 21:36 liisim_file.log
-rwxr-xr-x    1 hermanns users       27815 2006-08-05 14:24 liisim_vug.pl
```

Figure A3. Output of the directory liisim.

If changes in the source code of LIISim are made, the program must be recompiled on the current operating system of the web server. The perl script does not have be modified. The script must be modified if changes in the ASCII input files of LIISim are made. If the number or order of data in the input files is changed, this must be considered in the sub-routines of the perl script that create the input files.

If the web interface is moved to another server or if the directory path of the perl script is changed, the first line, the so called *shebang,* might have to be changed to the path of the current perl executable on the new server. The first two variables in the perl script, i.e. `my $perlscript` and `my $output_dir` must be set to the new paths. The first part of the perl script is shown in Figure A4.

```
#! /usr/bin/perl -w

# option -w: checks for web security

###################################################
#
# Main program liisim_vug.pl
#
# Web-Interface version 0.2 for LIISim
#
# Written by Max Hofmann, April 2006
#
###################################################


use CGI qw(:standard);# Module for printing HTML commands
use FileHandle;       # Module for file input/output
use strict;


# Set directories and file names!

my $perlscript = "/~hermanns/liisim/liisim_vug.pl"; # do not combine with $output_dir
my $output_dir = "/users/nusmd1/hermanns/public_html/liisim";
my $lii_start = $output_dir . "/lii_start.dat";
my $lii_internal = $output_dir . "/lii_internal.dat";
my $lii_heatconduction = $output_dir . "/lii_heatconduction.dat";
my $lii_evaporation = $output_dir . "/lii_evaporation.dat";
my $lii_detection = $output_dir . "/lii_detection.dat";
my $lii_absorption = $output_dir . "/lii_absorption.dat";
my $liisim_program = $output_dir . "/liisim";
my $logfile = $output_dir . "/liisim_file.log";
my $gnuplotinputfile = "gnuplotinput.gnu";
my $gnuplot_program = "gnuplot";
my $home = "http://www.liisim.com";
my $liigraph;
my $liidatafile;
```

Figure A4. First part of the LIISim perl script.

Future applications of the web interface should include more features of LIISim. For instance, a more detailed access to the physical input parameters, e.g. the heat capacities, should be included. An access to the fitting module of LIISim can be made available if individual experimental LII signals are uploaded. However, all calculations are performed on the relatively slow web server and, therefore, the calculation speed of LIISim must be significantly increased.

ACKNOWLEDGEMENTS – DANKSAGUNG

Eine Doktorarbeit schreibt sich nicht von alleine, und es gibt viele Leute, ohne die das Gelingen dieser Arbeit nicht möglich gewesen wäre.

Ganz herzlich möchte ich mich bei Prof. Dr. Jürgen Wolfrum für die Aufnahme in seinen Arbeitskreis sowie für seinen Einsatz und ständige Unterstützung während dieser Arbeit bedanken. Herr Wolfrum, Sie haben mich mit einem hervorragenden wissenschaftlichen Umfeld in Kontakt gebracht und konnten dabei eine besondere Begeisterung für Forschung und Wissenschaft verbreiten.

Sehr ausdrücklich möchte ich mich bei Prof. Dr. Christof Schulz für die exzellente Betreuung während meiner Doktorandenzeit bedanken. Christof, vielen Dank für die vielen Ratschläge, die Unterstützung und die Hilfe in unzählbaren Bereichen der Arbeit. Jederzeit hattest Du ein offenes Ohr für meine Fragen, und Du hast immer eine Lösung für auch noch so komplizierte Probleme gefunden. Die vielen fruchtbaren wissenschaftlichen Diskussionen mit Dir waren von unschätzbarem Wert. Vielen Dank für die einzigartigen Möglichkeiten, die Du mir während der Arbeit geboten hast.

Ein ganz besonderer Dank geht an Herrn Prof. Dr. Dr. h.c. Gg. Wagner und Frau Dr. H. Jander von der Universität Göttingen. Sie haben die Grundlage für den Bau des Hochdruckbrenners und somit dieser Dissertation geschaffen. Die vielen Telefonate, Emails und insbesondere die persönlichen Treffen mit Frau Jander waren von unschätzbarem Wert für diese Arbeit. Nicht zu vergessen ist natürlich Herr Pape. Mit seinem langjährigen Verständnis im Bereich der Hochdruckbrenner und seinen vielen cleveren Ideen, war er einer der tragenden Säulen des Brennerprojekts.

Wo wäre ich ohne die feinmechanische Werkstatt des PCI gewesen? Nirgends, denn der gesamte Brenner, jede Fräsung, Bohrung und jeder Feinschliff wurde in einzigartiger Präzision vom Team der Werkstatt bearbeitet. Insbesondere Herr Weis und Herr Schmitt konnten mit unzerstörbarer Ruhe bei den unzähligen Problemen beim Bau und den etlichen Reparaturen des Brenners stets weiterhelfen.

Vielen Dank auch an die Heidelberg Bürokollegen: Wolfgang, vielen Dank für die

Hilfe und Unterstützung bei der Brennerplanung und für die unzähligen Programmiertipps bei LIISim und dem kryptischen Perl. Helmut, vielen Dank für die nette Zeit mit Dir im Büro und im Labor, das Skifahren und vieles mehr. Frank, unvergesslich sind unsere Blobby-Volley-Kämpfe – diese haben die schweren Zeiten der Arbeit wesentlich versüßt. Wieland und Frank, mit Euch konnten die Inline-Hockey-Spiele erst richtig starten und haben zu einem körperlichen Ausgleich zum Labor und dem Büro gesorgt. Burkhard, vielen Dank für die vielen musikalischen Inspirationen, den Filmtipps und den lustigen Abenden im Karlstorbahnhof und der Villa Nachttanz – der Schnee morgens war schon beeindruckend. Isabell, Axel, My Yen und Daniel: Vielen Dank für die gute und nette Zeit mit Euch, der Hilfe und den netten Diskussion beim Kaffee trinken im Botanik. Vielleicht hätte ich doch noch die Wanderstatistik der Botanik-Stühle mit in den Anhang der Arbeit aufnehmen sollen.

Ein großer Dank geht selbstverständlich an die Duisburger Mannschaft. Boris, vielen, vielen Dank für die langen und hilfreichen Diskussionen und Ratschläge. Nach meiner einsamen LII-Zeit in Heidelberg hatte ich in Duisburg endlich einen „Verbündeten“ gefunden. Vielen Dank auch an Ben, Pascal, Kemal, Ralf Starke, Ludger Jerig, Dieter Hermanns, Barbara Graf und insbesondere an Natascha Schlösser, die meinen, zum Teil sehr drängenden, Nachforderungen nach den Elektronenmikroskop-Aufnahmen immer schnell nachgekommen ist.

Tonghun, many, many thanks to you for your help in „burning“ questions, any kind of high-pressure information and, above all, a cool friendship. I certainly will drop by in Michigan so we can go milking cows.

Schließlich möchte ich meinen Eltern für ihre Unterstützung während meines gesamten Studiums in Tübingen, Heidelberg und Stanford danken. Ohne Euch wäre mein Studium in dieser Art nie möglich gewesen.

Eidesstattliche Erklärung

Hiermit erkläre ich an Eides statt, dass ich die vorgelegte Dissertation selbst verfasst und mich dabei keiner anderen als der von mir ausdrücklich bezeichneten Quellen und Hilfsmittel bedient habe.

Heidelberg, den 5. Oktober 2006

Maximilian Hofmann